DISS. ETH NO: 22666

Microscopic Coexistence of Antiferromagnetic and Spin glass States in Disordered Perovskites

A thesis submitted to attain the degree of

DOCTOR OF SCIENCES of ETH Zurich

(Dr. sc. ETH Zurich)

presented by

SHRAVANI CHILLAL

M. Sc., Technische Universität München

born on 27.08.1986

citizen of Republic of India

accepted on the recommendation of

Prof. Dr. A. Zheludev, examiner
Dr. S. N. Gvasaliya, co-examiner
Dr. P. Gehring, co-examiner

2015

Abstract

Disorder and frustration give rise to a multitude of exotic phenomena in magnetism. Spin glass, a randomly frozen state of spins, is one of the several magnetic ground states directly originating from the presence of these two ingredients. This ground state is experimentally observed in many magnetic materials including alloys, amorphous inter-metallics, and insulators. Long-range mean-field theory and numerical results also predict a spin glass ground state for systems containing disorder and frustration. These methods further predict another ground state where spin glass coexists with a long-range magnetic order. However, so far there is no unambiguous experimental data with which to study this ground state carefully.

This thesis is devoted to the study of the magnetic ground states of disordered perovskites, particularly the coexistence of spin glass and long-range antiferromagnetic order. This work considers stoichiometric dilutions of magnetic ions in perovskite crystals. The major reason for doing this is to prevent any uncertainty due to chemical phase separation arising from non-stoichiometric dilution, which plagued all previous experiments. The compounds under study are: $PbFe_{1/2}Nb_{1/2}O_3$ (PFN), $PbFe_{1/2}Ta_{1/2}O_3$ (PFT), $PbFe_{2/3}W_{1/3}O_3$ (PFW), and $PbCo_{1/3}Nb_{2/3}O_3$ (PCN).

PFN is a disordered antiferromagnet ($T_N = 143$ K) in which magnetic Fe^{3+} is diluted with 50% non-magnetic Nb^{5+} ions. Below $T_{SG} = 12$ K, the system undergoes a transition into spin glass state. In the present work, the exact magnetic ground state of PFN is probed using neutron scattering and Mössbauer spectroscopy. Neutron scattering confirms that the antiferromagnetic Bragg peak that sets in below T_N persists into the spin glass state. However, intensity of the Bragg peak shows a slight reduction below $\sim$50 K. On a local scale, we observe that the magnetic hyperfine field seen in Mössbauer spectra rapidly increases below this temperature. Further, we find that the hyperfine field has dynamic fluctuations that slow down on cooling. These fluctuations vanish below the spin glass transition, and a homogenous ground state is established with a microscopic coexistence of antiferromagnetic and spin glass states (AFSG). This ground state can be described by the canting of spins in a conventional antiferromagnet where the angle of canting differs from site to site randomly. In this arrangement, the transverse components of the spins are randomly frozen giving rise to spin glass properties while the longitudinal components contribute to the mean antiferromagnetic structure. This is similar to the picture proposed by mean field theory in Heisenberg systems for a transition into a coexisting ferromagnetic and spin glass state. To better understand this ground state, the requirements for the AFSG state in these perovskites are probed by concentrating on the role of the non-magnetic ion and the concentration of the magnetic ion.

PFT is a close relative of PFN in which the non-magnetic Nb^{5+} is stoichiometri-

cally substituted by another non-magnetic Ta^{5+} ion. Our measurements based on bulk magnetization, neutron diffraction and Mössbauer spectroscopy show that the magnetic phase diagram of PFT is identical to that of PFN . Meaning, PFT is an antiferromagnet at high temperature (T_N=153 K) and undergoes a second transition at lower temperature exhibiting spin glass properties. At base temperature, the AFSG ground state is observed. Therefore, we can conclude that the AFSG state is unaltered by the iso-valent substitution of the non-magnetic ion in PFN .

PFW and PCN belong to the same family of perovskites as PFN . These compounds have different magnetic ion concentrations (higher in PFW , lower in PCN). However, the change in composition is inevitably accompanied by a different non-magnetic ion in PFW and a different magnetic ion in PCN in order to keep the stoichiometric dilution. The magnetic ground state probed by bulk magnetization in PFW suggests no indication of spin glass properties in the sample. Although neutron diffraction confirms the onset of antiferromagetic order below T_N=350 K which survives down to the base temperature 1.5 K, the results are less reliable due to a ferromagnetic impurity in the sample. In the case of PCN , bulk magnetization shows paramagnetic behavior. However, the susceptibility deviates from Curie-Weiss fit below ∼60 K indicating the presence of magnetic correlations in the sample. This is further evidenced in μSR spectroscopy through the relaxation of muon decay. We observe that the magnetic correlations increse upon cooling. However, they do not culminate into any kind of magnetic ordering even down to 20 mK.

Overall, the thesis establishes a solid experimental proof for the coexistence of long-range magnetic order with a spin glass state.

Zusammenfassung

Unordnung und Frustration führen zu vielen exotischen magnetischen Phänomenen. Ein Spinglas, in dem Spins in eine willkürliche zufällige Richtung eingefroren sind, ist einer von vielen möglichen Grundzuständen, der unmittelbar auf diese beiden Effekte zurückführen ist. Experimentell wurde dieser Grundzustand in vielen magnetischen Materialien, wie zum Beispiel Legierungen, amorphen intermetallischen Verbindungen und Isolatoren nachgewiesen. Langreichweitige Molekularfeldtheorie und numerische Simulationen sagen diesen Spinglas-Gundzustand auch für Systeme die sowohl intrinsisch ungeordnet als auch frustriert sind vorher. Ausserdem wird ein weiterer Grundzustand, in dem langreichweitige magnetische Ordnung und der Spinglas koexistieren, von diesen Methoden prognostiziert. Allerdings gibt es gibt es bis jetzt keinen eindeutigen experimentellen Beweis für diese Spinkonfiguration.

In dieser Doktorarbeit wird der magnetische Grundzustand von ungeordneten Perowskiten untersucht, insbesondere die Koexistenz von Spingläsern mit langreichweitiger Ordnung. Die vorliegende Arbeit befasst sich mit, stöchiometrischen Verdünnungen von magnetischen Ionen in Perowskit-Kristalle. Der Hauptgrund hierfür ist, Unsicherheiten in Hinblick auf eine möglichen Phasenseparation ausschliessen zukönnen, die bei nicht-stöchiometrischen Materialien auftreten, die in allen vorherigen Experimenten auftraten. Die hier untersuchten Verbindungen sind: $PbFe_{1/2}Nb_{1/2}O_3$ (PFN), $PbFe_{1/2}Ta_{1/2}O_3$ (PFT), $PbFe_{2/3}W_{1/3}O_3$ (PFW), und $PbCo_{1/3}Nb_{2/3}O_3$ (PCN).

PFN ist ein Antiferromagnet (T_N = 143 K), in dem die magnetischen Ionen Fe^{3+} mit nicht magnetischen Nb^{5+} Ionen verdünnt werden. Unterhalb von T_{SG} = 12 K friert das System in einem Spinglas-Zustand ein. In der vorliegenden Arbeit wird dieser Grundzustand mittels Neutronenstreuung und Mössbauer-Spektroskopie untersucht. Erstere bestätigt, dass die magnetischen Bragg-Reflektion, die unterhalb von T_N auftritt, auch die Spinglas-Phase überdauert. Allerdings ist die Intensität unterhalb von ∼50 K leicht reduziert. Im Gegensatz dazu steigt simultan das lokale Hyperfeinfeld vom Eisen, welches mit Hilfe von Mössbauerspektrokopie ermittelt wurde, stark an. Diese Zunahme wird auf das Einfrieren von Fluktuationen zurückgeführt. Unterhalb T_{SG} sind diese komplett unterdrückt und der homogener Grundzustand ist eine mikroskopische Koexistenz von antiferromagnetischer Ordnung und Spinglas (AFSG). Dieser Zustand ist ein konventioneller Antiferromagnet, dessen Spins vom Gitterplatz abhängig in einer zufälligen Richtung als auch Winkel gekantet sind. In dieser Beschreibung ist die transversale Komponente beliebig eingefroren, was zu den Spinglaseigenschaften führt, während die longitudinale antiferromagnetisch geordnet ist. Ein ähnliches Verhalten wurde mit Hilfe von Molekularfeldtheorie in Heisenbergsystemen für einen Übergang in einen koexistierenden ferromagnetischen Spinglas-zustand vorhergesagt.

Um das Verhalten des AFSG in Perowskiten besser zu verstehen, wurde der Effekt einer Substitution des magnetischen beziehungsweise unmagnetischen Ions untersucht.

PFT ist artverwandt zu PFN und unterscheidet sich durch die stöchiometrische Substitution des nicht magnetische Ions Nb^{5+} mit dem nicht magnetischen Ta^{5+} Ion. Magnetisierungs-, Neutronendiffraktions- und Mössbauermessungen verdeutlichen, dass das magnetische Phasendiagramm von PFT identisch zu PFN ist. Das bedeutet, PFT wird ein Antiferromagnet bei hoher Temperatur (T_N = 153 K) und durchläuft einen zweiten Übergang bei niedriger Temperatur sich Spinglas-Eigenschaften einstellen. Bei Basistemperatur wird der AFSG-Grundzustand beobachtet. Daraus wird geschlossen, dass der AFSG unabhängig von der der Substitution eines nichtmagnetischen Ions mit gleicher Valenz ist.

PFW und PCN gehören zur gleichen Familie der Perowskite wie PFN . Diese Materialien haben im Unterschied zu PFN eine höhere (PFW) beziehungsweise niederigere (PCN) Konzentration des magnetischen Ions. Allerdings, ist die Änderung der Zusammensetzung unwiderruflich mit einem Austausch des magnetischen Ions (PCN) oder des nichtmagnetischen Ions (PFW) verknüpft, um die stöchiometrische Vermischung zu erhalten. Magnetisierungsmessungen von PFW zeigen keine Anzeichen eines Spinglases, obwohl mit Hilfe von Neutrondiffraktion eine antiferromagnetische Ordnung unterhalb von T_N=350 K gefunden wurde. Im Fall von PCN wird ein paramagnetisches Verhalten durch Magnetisierungsmessungen beobachtet. Allerdings weichen die Suszeptibilitätsdaten unterhalb von ∼60 K vom Curie-Weiss-Fit ab, was die Existenz von magnetischen Korrelationen nahelegt. Dies wurde auch durch μSR Spektroskopie beobachtet. Beim Abkühlen nehmen die magnetischen Korrelationen zu, allerdings wird keine langreichweitige magnetische Ordnung bis zur tiefsten gemessen Temperatur von 20 mK gefunden.

Zusammengefasst zeigt diese Arbeit den soliden experimentellen Beweis für die Koexistenz von langreichweitiger Ordnung mit einem Spinglas auf.

Contents

Chapter 1

Background and Motivation

Magnetism in condensed matter systems is a rich phenomena arising out of spin-spin interactions. Especially in crystalline systems owing to the various possibilities in arrangement of atoms (crystal structure) a wide range of interactions are possible over various time and length scales. In ideal crystals consisting of a regular arrangement of one or two kinds of atoms, relatively simple phases such as paramagnetism, ferromagnetism or antiferromagnetism occur. However, once the complexity in crystal structure and bond arrangement is introduced magnetic interactions start becoming complex, leading to the emergence of new phases such as canted spin structures, spin glass states, spiral magnets, speromagnets, etc. One of the primary ways of producing such complex states is through the introduction of new chemical species or by creating variations in bonds, which ultimately result in a distribution strengths of magnetic interactions within the same material. Complex phases due to such a distribution of interactions could sometimes result from disorder or randomness in bonds or chemical species. Besides this, there could also be competing interactions which then lead to frustration (i.e, the inability to reach a minimum energy state).

The main focus of this thesis will be on the study of complex ground states and interactions resulting from disorder and frustration. Specifically, the coexistence of magnetic long-range order (LRO) and spin glass state (SG) will be studied in detail. In the present chapter we will attempt to place the study in a broader context. We will first briefly review the main constituent phenomena: disorder and frustration and their effects on magnetic interactions and particularly on the spin glass state. Thereafter, we look on how these phenomena further lead to the coexisting phase (long range order and spin glass) and try to assess the current understanding of such a coexistence. Finally we describe the outline of the thesis and the magnetic materials that are used to probe such a coexisting phase.

1.1 Disorder

The term *disorder* generally refers to any deviation from perfect order in a system. In crystalline solids disorder can occur due to imperfections in the periodic arrangement of atomic planes or lines such as stacking faults, twinning defects, vacancies etc., or due to imperfections in atomic sites such as point defects. Another situation arises when some atoms in regular lattice sites are replaced by different species (elements).

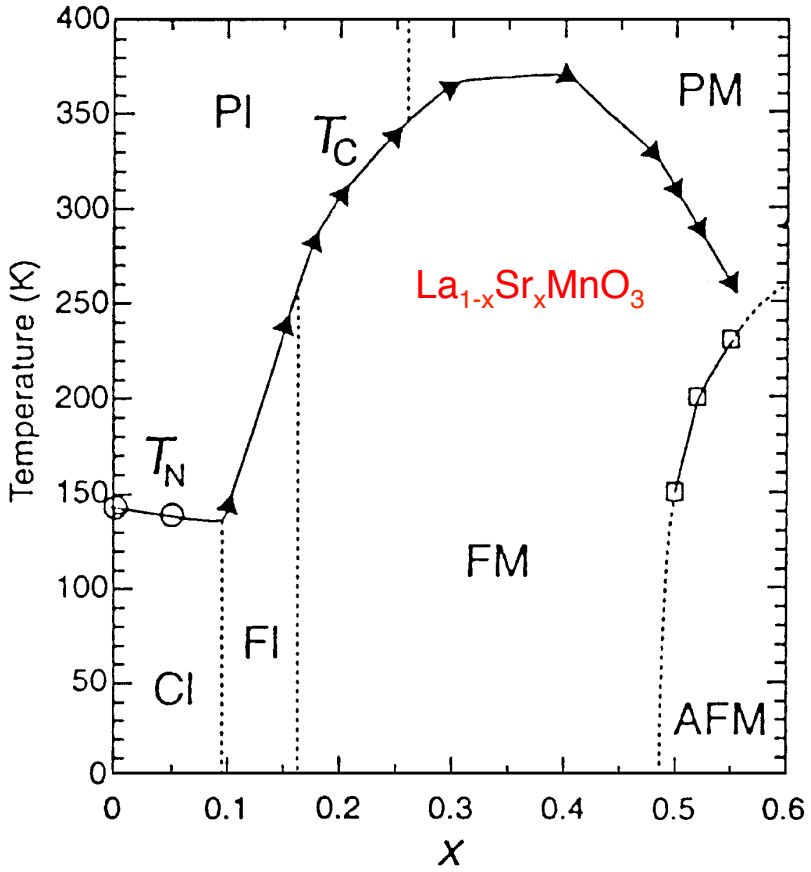

Figure 1.1: Phase diagram of $La_{1-x}Ca_xMnO_3$ as a function of Ca concentration. Here, PI: paramagnetic insulator, CI: canted insulator, PM: paramagnetic metal, FM: ferromagnetic metal and AFM: antiferromagnetic metal [1].

These substituted atoms introduce chemical disorder into the host crystal structure and disorder to the periodic potential of the crystal or in its spin arrangement. As these atoms are bound to the unit cell, their distribution configuration is frozen over time and temperature. This kind of disorder is known as *quenched* chemical disorder. Depending on the fraction of host atoms replaced, this disorder can lead to significant changes in physical properties of the system.

Especially in magnetic materials, the quantity and type of the substituted species leads to various changes in the magnetic behavior of the system. In some materials, this may generally lead to a reduction or an increase of the critical temperatures of the long-range magnetic ordering if the amount of dilution is small. However, as the degree of dilution goes on increasing new magnetic phases start to appear leading to a rich magnetic phase diagram. For example, such a behavior is nicely illustrated in diluted rare earth manganite $La_{1-x}Sr_xMnO_3$ in Fig. 1.1 [1]. In this system the parent $LaMnO_3$ is a canted antiferromagnet in the ground state. Dilution of 'La' with non-magnetic 'Sr' first reduces this transition to lower temperatures. When the concentration of dilution increases above x=0.1, the system realizes a ferromagnetic ground state with a Curie temperature that increases up to x=0.4. This dilution also affects the conductivity of the system by inducing a metal-insulator transition in the phase diagram. Above x=0.5

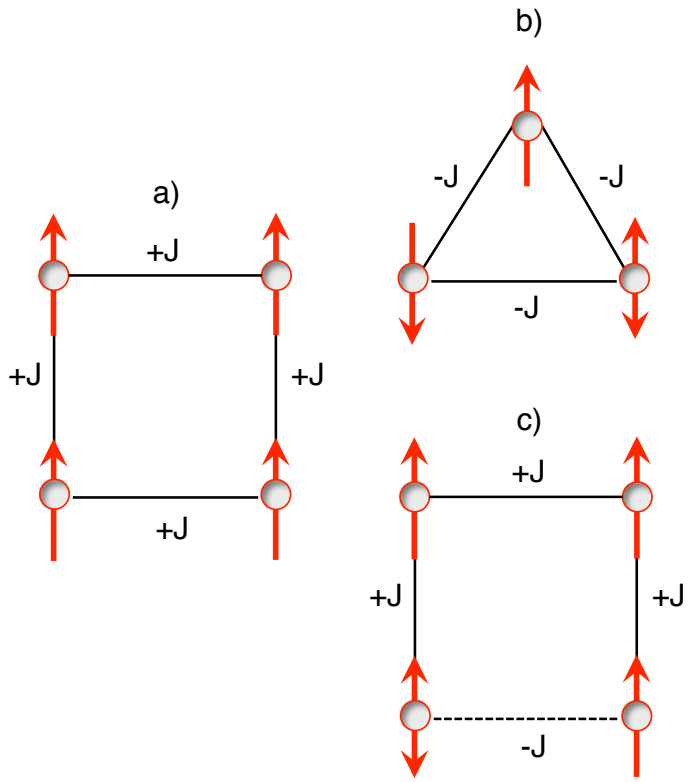

Figure 1.2: a) Spin configuration for a square lattice ferromagnet with nearest neighbor interaction $J_{ij} = +$ J, b) Geometrical frustration in a triangular lattice with antiferromagnetic nearest neighbor interactions and c) Frustration in a spin system due to random replacement of one of the ferromagnetic exchange in the square lattice of a) with an antiferromagnet exchange (-J).

the system stabilizes into an A-type antiferromagnetic state with ferromagnetism in planes and antiferromagnetism between those planes.

A second effect of the quenched disorder is the critical phenomena of the phase transitions. In the case of second order phase transition, the disorder may modify the set of critical exponents leading to new universality class. Likewise, the discontinuities of the first order phase transitions are known to be smeared out as a result of disorder in the system. Overall, the introduction of disorder leads to a rich and complex physics in solid state systems and hence continues to remain the focus of ongoing condensed matter research.

1.2 Frustration

In a conventional ferromagnet (FM) or antiferromagnet (AF), the spins are perfectly aligned in a lattice either in parallel or anti parallel manner depending on the exchange between them as in Fig. 1.2a for a ferromagnet. Here, all ferromagnetic interactions $J_{ij} > 0$ are satisfied simultaneously by all the spins. However, in certain systems the geometry of the crystal lattice does not allow all the interactions to be satisfied simulta-

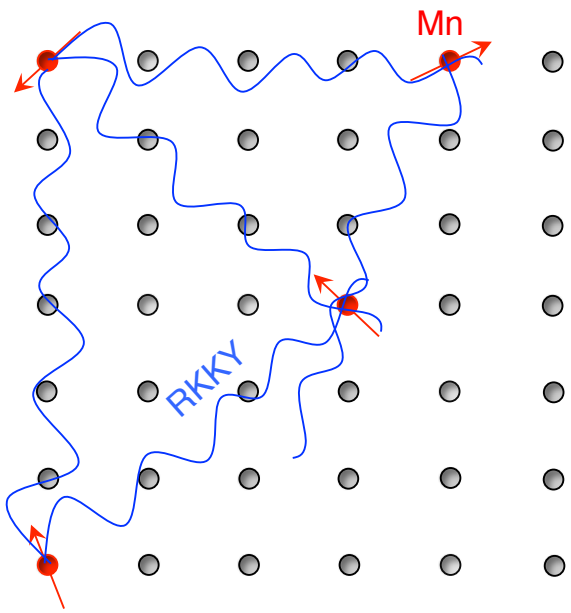

Figure 1.3: Schematic of the spin freezing due to long-range oscillating RKKY interactions (blue lines) in the dilute metallic spin glass CuMn.

neously. For example, in a triangular lattice having nearest neighbor antiferromagnetic interactions, as in Fig. 1.2b, the alignment of one of the spins is undetermined due to its geometry. When such a situation prevails in the whole lattice the system cannot realize a single minimum energy ground state. This condition is known as *frustration* and leads to a variety of degenerate ground states. Due to this, the system cannot settle into a unique magnetic structure. However, metastability is exhibited due to the relatively small energy required to switch between the ground states. This results in history-dependent magnetic properties, and a slow relaxation towards equilibrium. The ground states in most of these systems generally exhibit cooperative paramagnetism consisting only of short-range spin correlations.

Frustration is also observed in many other systems for non-geometrical reasons, for example bond disorder or site disorder. A simplistic picture of this situation can be observed in a square lattice having nearest neighbor antiferromagnetic interactions. If one of the ferromagnetic interactions is replaced with an antiferromagnetic interaction of the same strength, as in Fig. 1.2c, the competition between interactions leads to frustration. As in the geometrically-frustrated case, this too leads to multiple degenerate ground states. However, in the presence of frozen-in disorder, frustration leads to a new magnetic ground state known as a spin glass. As will be discussed in the next section, many of the properties of spin glasses are characteristic features of degenerate ground states.

1.3 Spin glasses

A spin glass can be defined as randomly frozen state of magnetic moments over macroscopic time scales. Historically, the spin glass state was first observed in metallic systems diluted with a small concentration of magnetic ions, for example Mn ions in

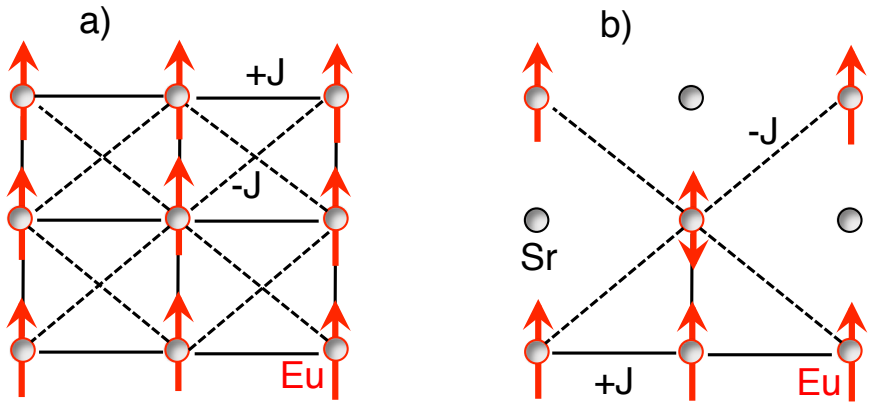

Figure 1.4: The mechanism of frustration (competing interactions) created by short-range interactions as seen in insulating spin glass $Eu_xSr_{1-x}S$. The dashed lines stand for weak AF exchange and solid lines those of strong FM. a) Represents the stable ferromagnetic state of Eu rich compound, b) shows the effect of non-magnetic Sr leading to frustration.

Cu metal, Fe in Au, or Mn in Ag. Magnetic ions in these alloys are randomly distributed in the metal matrix creating chemical disorder. In a metal host, the impurity moments are coupled with each other through an exchange interaction known as the RKKY interaction the strength of which is written as

$$J_{RKKY}(R) \propto J^2 g(\epsilon) \frac{\sin(2k_F R) - 2k_F R\cos(2k_F R)}{(2k_F R)^4}$$

where, $g(\epsilon)$ is the electronic density of states of the metal, k_F is the Fermi wave vector, J is the exchange strength between the Mn moment and the conduction electron spin. This indirect interaction basically describes the polarization of a sea of conduction electrons surrounding a magnetic ion situated at the origin, which then couples to the next magnetic moment at a distance R. The RKKY interaction is distance dependent, long-range, and oscillatory in nature. Therefore, the coupling interaction J_{RKKY} is $\pm J$ i.e, ferromagnetic or antiferromagnetic depending on the distance between two magnetic ions as illustrated in Fig. 1.3. This leads to competing interactions between Mn moments due to their random distribution, thereby freezing them in random directions.

Apart from systems with magnetic impurities in metallic hosts, spin glasses have also been found in magnetic insulators such as $Eu_xSr_{1-x}S$ in which long-range RKKY interactions are not present. Rather, the system has short-range interactions with two relevant exchange interactions: a) nearest neighbors coupled through ferromagnetic exchange (J_1) and b) next-nearest neighbors through antiferromagnetic J_2 such that $\frac{J_2}{J_1} = -0.5$. In the Eu rich limit the ferromagnetic interactions dominate, and the system stabilizes in a ferromagnetic arrangement (see Fig. 1.4a). The random introduction of non-magnetic Sr in place of Eu leads to competing interactions in the system as demonstrated in Fig. 1.4b resulting in a spin glass state [2].

Therefore, it is understood that, despite the nature of the magnetic system, disorder together with frustration are essential ingredients to form spin glass state.

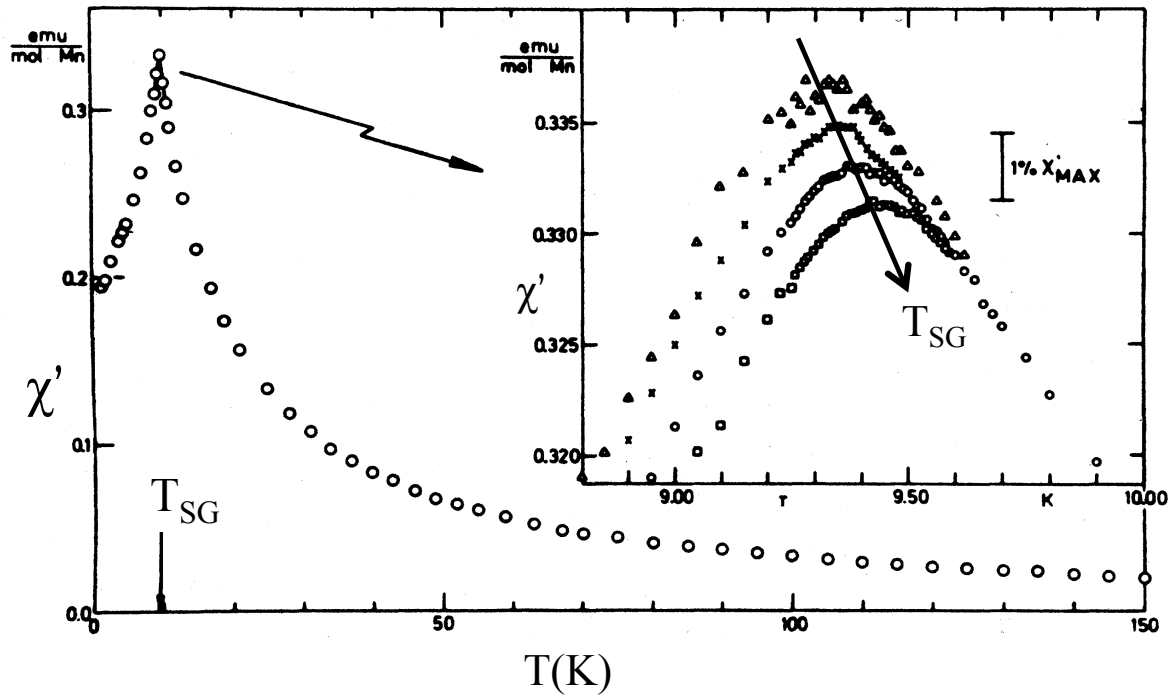

Figure 1.5: The *ac* susceptibility of Cu-Mn intermetallic spin glass system showing a cusp at T_{SG}. The inset illustrates the frequency dependence of the *ac* susceptibility [3].

1.3.1 Properties

In the spin glass state the time averaged value of spin S_i is non-zero. However, it does not exhibit a periodically ordered spin structure as in a ferromagnet or an antiferromagnet i.e, the spin-spin correlation function $< S_i S_j >$ does not show long-range order. Therefore, a spin glass transition is not accompanied by the appearance of a spontaneous or staggered magnetization. Instead, it is indicated by a cusp at the so-called spin glass freezing temperature T_{SG} in the real part of *ac* susceptibility (χ'). This is illustrated in Fig. 1.5 for Cu-Mn spin glass system. In addition, χ' is frequency-dependent below glass transition while T_{SG} shifts to higher temperatures for increasing frequencies of the applied *ac* fields. Inset of Fig. 1.5 illustrates this change for CuMn covering many orders of magnitude in frequency. This behavior indicates that the system has many metastable ground states covering a wide range of characteristic excitation and relaxation time scales.

The glassy nature of the spin state below T_{SG} results in another feature of the spin glass called remanence. This refers to the dependence of the *dc* susceptibility (χ_{dc}) on the the way the experiment is performed. Fig. 1.6 shows χ_{dc} measured for CuMn as a function of temperature in two ways: a) cooled from the paramagnetic state in a small external magnetic field to $T<T_{SG}$ and then χ_{dc} (FC) is measured while warming, b) cooled in zero-field to $T<T_{SG}$ and then measured χ_{dc} (ZFC) after the application of a small external field while warming. In the paramagnetic state the two curves collapse onto each other while a splitting appears below T_{SG}. In addition, one observes that the FC is reversible whereas ZFC is not i.e, any change in the experimental sequence affects the ZFC magnetization. If the external field in a) is switched off after reaching

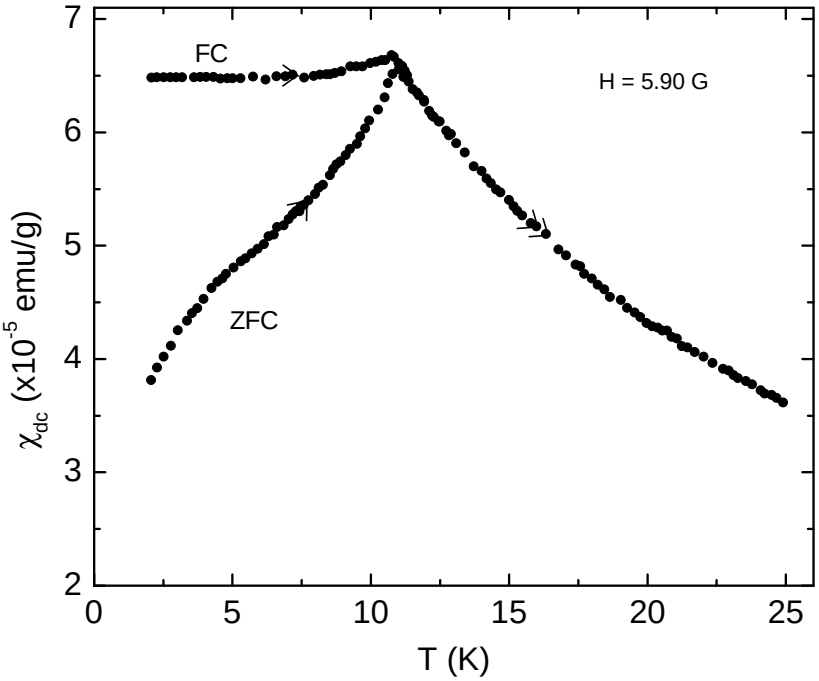

Figure 1.6: The *dc* susceptibility of CuMn(3%) showing the splitting of field cooled and zero-field cooled magnetizations [4].

T<T$_{SG}$ and χ_{dc} is measured as a function of time at constant T, the FC value slowly relaxes to its corresponding value in ZFC. This feature is known as thermo remanence magnetization.

The history dependence of χ_{dc} also leads to various other phenomena in spin glass systems known as rejuvenation, aging, and memory effects. Aging of a spin glass system refers to an idle waiting time t$_w$ at a temperature T$_w$ <T$_{SG}$ while zero-field-cooling the system down to T$_l$ <<T$_{SG}$. If χ_{dc} is measured as a function of temperature in a small field (like in ZFC) while heating from T$_l$, a dip in χ_{dc} is observed at T$_w$. Above this temperature χ_{dc} reverts or rejuvenates to its original value. These two effects are known as memory and rejuvenation. Fig. 1.7 demonstrates this behavior for a Cu-Mn spin glass having T$_{SG}$= 57 K.

Here, χ_{dc} (FC and ZFC) is measured twice while heating: first, after continuously cooling the system down to the lowest temperature directly and second, after waiting for t$_w$= 3000 s at T$_w$=40 K. The two procedures do not affect the FC magnetization, but a dip is observed at 40 K in the ZFC case in the second procedure. This is clearly visible in the difference of ZFC's as shown in the inset.

Altogether, we can say that the presence of relaxation processes at all time scales, slow dynamics, and aging are characteristic magnetic features of a spin glass system. To understand the physical origin of such peculiar behavior many theoretical models have been proposed. In the next section some of these models are described briefly.

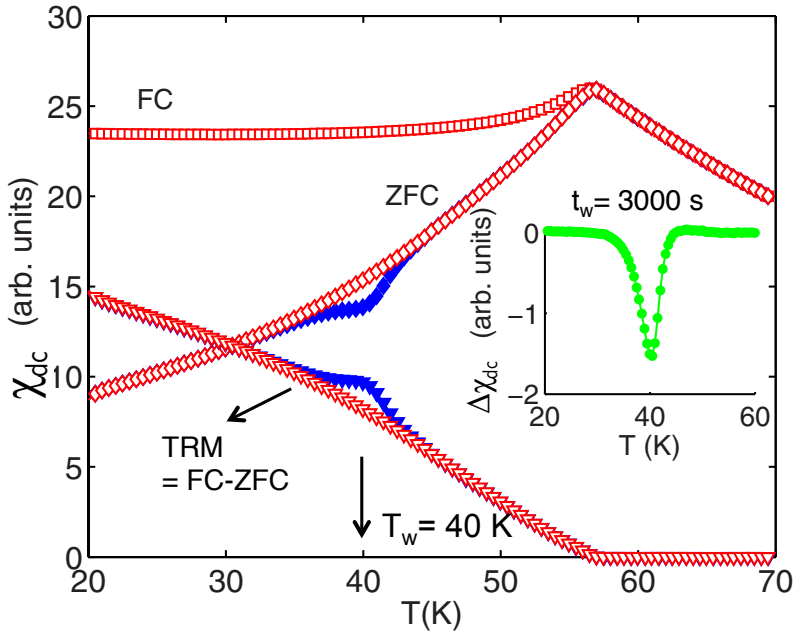

Figure 1.7: The *dc* susceptibitlity of the Cu-Mn system measured in a 0.5 Oe field using FC and ZFC protocols indicates the effect of aging, memory and rejuvenation effects below T_{SG}=57 K. The thermo remanent magnetization is the difference between the FC and ZFC magnetizations [5].

1.3.2 Theoretical Models

The earliest theoretical work towards understanding spin glasses is based on a conventional Heisenberg Hamiltonian for a simple d-dimensional magnetic system,

$$\mathcal{H} = -\sum_{<ij>} J_{ij} \sum_{m} \mathbf{S}_{im}\mathbf{S}_{jm} \tag{1.1}$$

where $\mathbf{S}_{im}$, $\mathbf{S}_{jm}$ are m-component spin vectors positioned at $\mathbf{r}_i$ and $\mathbf{r}_j$. Here, m=1, 2, and 3 correspond to Ising, XY and Heisenberg models respectively. The spins $\mathbf{S}_{im}$ and $\mathbf{S}_{jm}$ have nearest-neighbor interactions J_{ij}. Depending on the sign of J_{ij}, ferromagnetic or antiferromagnetic interactions are expected between the spins. Now, the site disorder observed in real spin glasses is described by disorder in J_{ij}. One of the possible ways to introduce disorder in J_{ij} is through bond disorder (varying the nearest-neighbor interactions).

Two methods to introduce this bond disorder were suggested by Edwards-Anderson (EA model) [1] assuming J_{ij}'s to be distributed in following fashion:

a) The '±J model' where discrete, i.e ferro or antiferro interactions of equal strength J are randomly chosen between spins. So the probability distribution of the spins becomes:

$$P(J_{ij}) = f\delta(J_{ij} - J) + (1 - f)\delta(J_{ij} + J) \tag{1.2}$$

[1] For further details of Edward-Anderson model refer to Ref. [6]

b) The second method assumes the interactions have a Gaussian distribution around a mean value J_0, leading to the following probability for J_{ij}:

$$P(J_{ij}) = \frac{1}{\sqrt{2\pi J^2}} e^{-\frac{(J_{ij}-J_0)^2}{2J^2}}. \tag{1.3}$$

These forms of the EA model are considered prototypes for disordered magnetic systems with competing interactions. For Ising spins, the Gaussian distributed bond-disorder (Eq. 1.3) succeeds in predicting a transition from a paramagnetic to a spin glass state below a certain temperature T_{SG}. In the paramagnetic phase the time averaged moment $< \mathbf{S}_i >= 0$ and in the spin glass phase $< \mathbf{S}_i > \neq 0$. However, the magnetization

$$M = \frac{1}{N}\sum_N < \mathbf{S}_i >= 0 \tag{1.4}$$

and the spin glass order parameter is given by $q_{EA} = [< \mathbf{S}_i >^2]_{avg} = \frac{1}{N}\sum_N < \mathbf{S}_i >^2$ (1.5)

is non zero.

Thus, this model shows a phase transition and hence describes the cusp in the *ac* susceptibility observed in spin glass systems at the paramagnetic-to-spin glass transition. However, the model also predicts a cusp in the specific heat at the spin glass transition, which does not match with the experimental observations.

Mean-Field Theory approach

As mean field theory (MFT) provides a simplified approach to understanding magnetic interactions, it could also be considered as a starting point to develop a theory for spin glasses. In this purview, the spin Hamiltonian would still be described by Eq. 1.1 (for Ising systems), where J_{ij} has a Gaussian distribution as in Eq. 1.3. In addition, MFT assumes that the interactions J_{ij} are of infinite range so that each spin in the N spin system interacts with all other spins with the same strength. Therefore, the mean and variance of the J_{ij} distribution now become

$$[J_{ij}]_{avg} = J_0/N \tag{1.6}$$

$$[J_{ij}^2]_{avg} - [J_{ij}]_{avg}^2 = J^2/N \tag{1.7}$$

Since there is disorder in J_{ij} due to bond disorder, the system can be assumed to comprise many different bond configurations. Each of these configurations is an ensemble of J_{ij}. Therefore, for each configuration c the free energy is $\mathcal{F}_c = -k_B T ln(Z_c)$, where Z_c is the partition function of each configuration. Now, the total free energy of the system is an average over all possible configurations, giving:

$$\mathcal{F}_{av} = \int \mathcal{F}_c P(c) dc \tag{1.8}$$

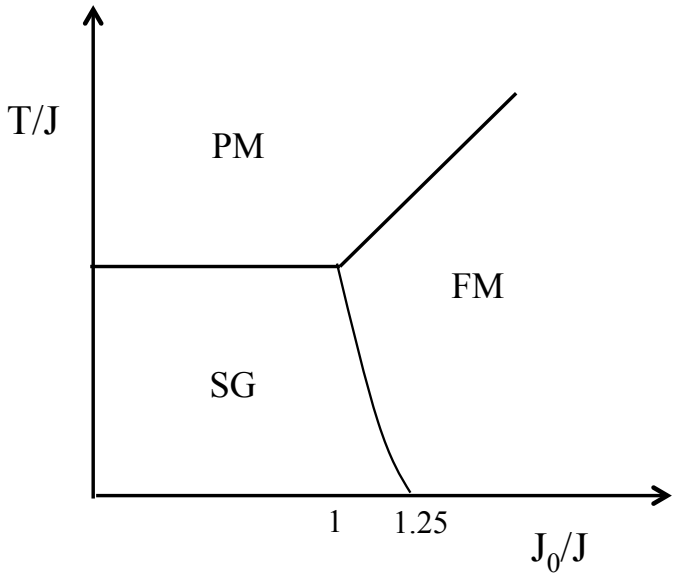

Figure 1.8: The phase diagram in terms of the average exchange J_0 and its width J as predicted by the SK model using the replica symmetry method. Here, PM: paramagnetic, FM: ferromagnetic and SG: spin glass.

where $P(c)$ is the probability distribution for configuration c. The solution for this integral using the identity

$$ln(Z_c) = \lim_{n\to 0} \frac{Z^n - 1}{n} \tag{1.9}$$

was first given for Ising systems by Sherrington and Kirkpatrick (SK) [7], who made use of the 'replica trick'. Here n is the number replicas of initial configuration c so that the integrand in Eq. 1.8 is $Z^n = \prod_c Z_c$. This means that all the configurations can be considered as non-interacting replicas. This is the replica trick. In the SK model the free energy was calculated for an infinite number of spins in the system. Deriving magnetization and order parameter from this calculation leads to three phases in zero field, as illustrated in Fig. 1.8.

Then, the EA spin glass order parameter, written as an overlap of any two replicas α, β of the system, is now same for any pair of replicas:

$$q_{EA}^{\alpha\beta} = [< \mathbf{S}_i >^2]_{avg} =< \mathbf{S}_i^{\alpha}\mathbf{S}_i^{\beta} >= q$$

Although this phase diagram predicts ferromagnetic and spin glass phases ground states, the model leads to unphysical negative entropies for Ising systems. Therefore, the replica symmetric solution succeeds in predicting the spin glass transition, but it fails to explain the characteristics of the spin glass phase.

This drawback is overcome by considering $q^{\alpha\beta}$ to be different for each pair of replicas. The spin glass order parameter is then actually an order parameter function [8] $q(x)$, i.e. the system has many possible states, which differ from each other by a small energy below T_{SG}. This picture helps in understanding the experimental observations of irreversibility in spin glasses. A system prepared in a ZFC condition reaches a

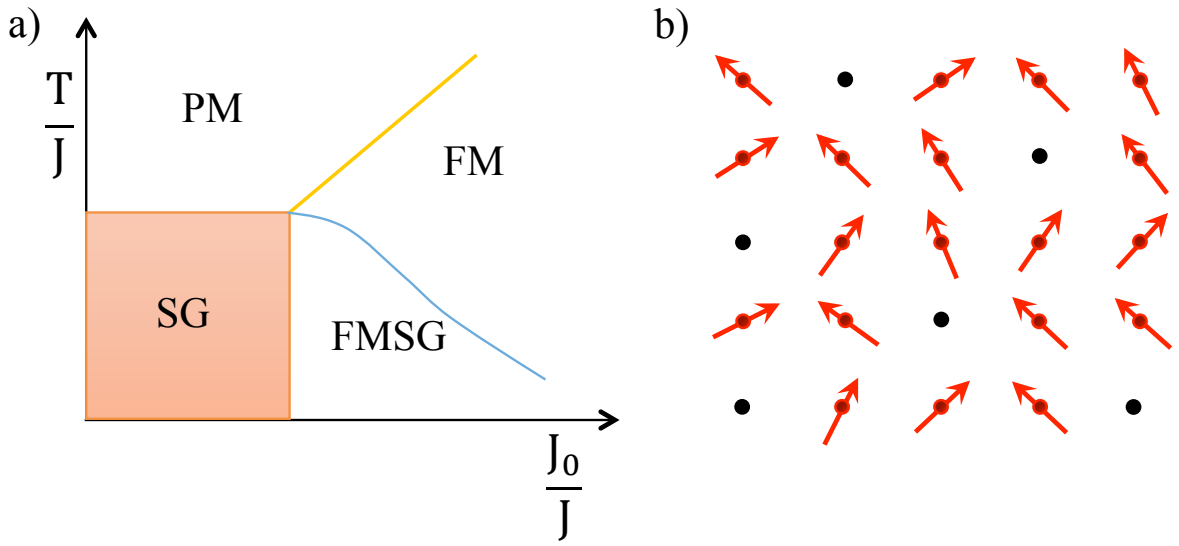

Figure 1.9: a) Phase diagram of the Heisenberg system for random exchange distribution as predicted by mean field approach in the case of mean exchange $J_0 \neq 0$. b) Schematic of the coexisting FMSG state.

certain metastable state below T_{SG} and hence shows corresponding non-zero χ_{dc} when a small external magnetic field is applied. The small field does not push the system into another state, and hence we obtain χ_{dc} for that state. But a FC system chooses a different state relevant to the applied magnetic field and stays in that state. Therefore, a difference between FC and ZFC susceptibilities is observed below T_{SG}. Similarly, a frequency measurement of the ac susceptibility probes only one particular state. By changing the frequency one can scan the different states, which results in a frequency dependent χ'_{ac} below T_{SG}.

The replica symmetric mean-field SK model can be extended to Heisenberg systems [9]. In this case, there are N vector spins $\mathbf{S}_i$ having $\mu = 1, 2, ..m$ components such that

$$\sum_{\mu} \mathbf{S}_{i\mu}^2 = m. \tag{1.10}$$

The m components of $\mathbf{S}_i$ interact via random, Gaussian distributed J_{ij} as given in Eq. 1.1 where $\frac{J_0}{N}$ is the mean and $\frac{J}{\sqrt{N}}$ is variance of the distribution. The spin Hamiltonian for such a system in the presence of an external magnetic field H_{ext} along $\mu = 1$ vector spin component is

$$\mathcal{H} = -\sum_{<ij>} J_{ij} \sum_{\mu} S_{i\mu} S_{j\mu} - H_{ext} \sum_{i} S_{i1} \tag{1.11}$$

This Hamiltonian predicts a ferromagnetic ordering when the mean exchange interaction J_0 is positive and large. However, when $J_0 = 0$, positive and negative couplings are randomly distributed such that spin glass ordering is observed. In the case when $H = 0$, the order parameter can be written as

$$q^{\alpha\beta} = [< \mathbf{S}_{i\mu} >^2]_{avg}.$$

If $J_0 \neq 0$ but is small and $H_{ext} = 0$, the system transforms from a collinear ferromagnetic state to a canted one. Therefore, the solution of this model predicts two magnetic ground states for the system depending on the value of J_0. Fig. 1.9a shows the phase diagram predicted by the model indicating four magnetic phases: paramagnetic, spin glass, ferromagnetic and spin glass+canted ferromagnet. In the canted phase the system has a non-zero spontaneous magnetization and spin glass ordering from the frozen transverse components. Therefore, this scenario illustrates a microscopic co-existence of long-range FM and SG states, and it is generally known as FMSG. A schematic of such a spin configuration is depicted in Fig. 1.9b.

The model also predicts a line of phase transitions for the FMSG state known as the G-T line (Gabay-Toulouse) in the presence of an external field. Here, the FM-FMSG transition occurs with the freezing of transverse spin components. Therefore, when an external field is applied, the longitudinal and transverse components of the order parameter are not identical. If the field is applied along the $\mu = 1$ component of the vector spin, the order parameter for a spin glass becomes

$$q^{\alpha\beta} = [< \mathbf{S}_{i\mu} >^2]_{avg} = q_{\perp} + (q_{||} - q_{\perp})\delta_{\mu,1}$$

where $q_{||}$ and $q_{\perp}$ are the longitudinal and transverse components of the order parameter with respect to the field direction. The longitudinal component $q_{||}$ is a measure of longitudinal correlations and therefore refers to the magnetization in the sample. At high temperatures, $q_{||}$ is non-zero if $H_{ext} \neq 0$. However, $q_{\perp}$ remains zero because there are no transverse components in the system. At the transition temperature T_{SG}, the transverse component of order parameter becomes non-zero indicating the second order nature of the transition. When plotted as a function of field, the replica symmetric formalism for vector MFT (with mean exchange $J_0 = 0$, variance J in Gaussian distribution) gives rise to a line of transitions,

$$1 - \frac{T_{SG}(0)}{T_{SG}(H)} \propto (\frac{H}{J})^2 \Rightarrow \text{G-T line.} \tag{1.12}$$

Two sub-lattice mean field theory approach

A second variant of the MFT approach is based on a two sub-lattice system of spins. For two sub-systems 1 and 2, each containing N Ising spins, the spin Hamiltonian is written as follows:

$$\mathcal{H} = -\sum_{<ij>} J_{ij}\mathbf{S}_{1i}\mathbf{S}_{2j}. \tag{1.13}$$

Here, the exchange interaction within each subsystem is ignored and J_{ij} refers only to the interaction between spins in different subsystems. As usual, the J_{ij} have a Gaussian distribution as in the single lattice system described in the previous section. The solutions of this model are similar to those of the single lattice system of the SK-model which predicts the transition sequence PM→FM→SG as well as PM→AF→SG depending on the average value of the exchange interaction J_0 [10].

When intra-sublattice exchange interactions V_{ij} are introduced in each subsystem, also having a Gaussian distribution, the model predicts a coexisting antiferromagnetic and spin glass (AFSG) ground state for both Ising and Heisenberg systems [11, 12].

Although the MFT approach provides a simplistic approach to understanding magnetic systems, its applicability to real systems cannot be justified in all cases. Especially in the spin glass case, equivalent, infinite-range interactions are unrealistic. Further, MFT ignores critical fluctuations, which are always present in real systems. Therefore, several numerical methods have been implemented for disordered spin systems that include short-range interactions. These methods also account for critical fluctuations, leading to multiple magnetic ground states that include spin glasses as well as spin glasses coexisting with long-range magnetic order.

1.3.3 Monte Carlo simulations

Much of the numerical work on spin glasses uses the EA model with short-range interactions having either random $\pm J$ or a Gaussian distribution of exchange constants (as in Eq. 1.2, 1.3). Monte Carlo simulations based on this model have been able to reproduce many of the experimental observations: a cusp in the *ac* susceptibility and a thermo remanent magnetization, etc. [13, 14]. For a long time the existence of a sharp phase transition has been debated in spin glasses. However, this has been established for 3d Ising systems at non-zero temperature - T_{SG} [15–17]. The transition is associated with a correlation length ξ_{SG} that defines the maximum length over which the short-range spin-spin correlations occur. As the SG transition is approached from above T_{SG}, ξ_{SG} diverges as

$$\xi_{SG} \propto \left(\frac{T}{T_{SG}} - 1\right)^{-\nu} \tag{1.14}$$

and the spin glass susceptibility χ_{SG} diverges as

$$\chi_{SG} \propto \left(\frac{T}{T_{SG}} - 1\right)^{-\gamma}. \tag{1.15}$$

The 3d Ising EA model gives $\nu \simeq 2.5$ - 2.7 and $\gamma \simeq 6$ - 6.5 [18, 19]. These values seem to be consistent with the experimentally observed exponents in Ising spin glass $FeMnTiO_3$ [20].

In the case of 3d Heisenberg systems, the presence of a non-zero temperature spin glass transition was controversial until recently. Although the discovery of spin glasses was first made in Heisenberg systems, initial work based on Monte Carlo simulations using EA model did not find evidence for a SG phase transition at non-zero temperature [21–23]. However, the later work [24] suggested that the experimental observation of Heisenberg spin glasses are driven by a quantity called *chirality*. This quantity is defined for systems with vector spins in which frustration induces canting of the ordered spins. Chirality c_i of this non-collinear spin structure at a site 'i' is written as:

$$c_i = \mathbf{S}_{i+1} \cdot \mathbf{S}_i \times \mathbf{S}_{i-1}$$

Numerical results based on this parameter indicate a 'chiral glass' ordering at temperatures $T_{CG} > 0$ whereas spin glass ordering is predicted only at $T_{SG} = 0$. Later work revealed that the ordering temperatures for chiral glasses and spin glasses are the same, and a consensus has now been reached in recent numerical studies based on 3d

Heisenberg EA model that a non-zero temperature spin glass transition exists [25–29]. However, the concept of chiral ordering, and whether or not it is coupled to spin glass is still under debate [27–30].

A second question that is still of concern in 3d Heisenberg systems is the critical exponents related to T_{SG}. Experimentally observed values for the critical exponents of canonical spin glasses are $\nu \simeq 1.3$ - 1.4 and $\gamma \simeq 2.2$ - 2.3 [31–33]. However, the corresponding results from numerical methods are not yet established. Therefore, an overall understanding of the non-zero temperature spin glass transition in 3d Heisenberg systems remains inconclusive.

On the other hand, the ground state of coexisting long-range magnetic order and spin glass in Heisenberg systems is numerically confirmed by Monte Carlo simulations. The calculations consider a simple cubic lattice of Heisenberg spins having nearest-neighbor ferromagnetic interactions for which the Hamiltonian is given by Eq. 1.11 [34, 35]. Frustration is introduced in the system by randomly replacing a fraction of the ferromagnetic bonds with antiferromagnetic ones. The model calculates the evolution of the root-mean-square spin length S_{rms},

$$S_{rms} = \left[\frac{1}{N}\sum_{i=1}^{N} < S_i >^2\right]^{1/2},$$

bulk magnetization

$$M = \frac{1}{N}\sum_{i=1}^{N} < S_i >,$$

and the transverse spin freezing

$$Q_{xy} = \frac{1}{N}\sum_{i=1}^{N}[< S_i > -(< S_i > .\hat{z})\hat{z}]^2.$$

Fig.1.10 plots the temperature dependence of the three parameters S_{rms}, bulk magnetization M, and mean transverse spin length Q_{xy}. We see that S_{rms} and M are nearly equal just below the FM Curie temperature (T_C) whereas Q_{xy} is zero. At T_{xy}, this component starts to set in indicating the onset of transverse spin freezing. Also, S_{rms} starts increasing rapidly, showing a deviation from the bulk magnetization below T_{xy}. These observations are attributed to the transverse spin freezing below T_{xy}. The results suggest that the transverse component is present already above T_{xy}, although its time average vanishes due to fluctuations. Below T_{xy}, this component freezes in random directions leading to a non-vanishing time average, but the spatial average becomes zero. Therefore, the bulk magnetization M is not altered. However, the site average of the squared transverse component is non-zero, which increases the value of S_{rms}. Further, these calculations suggest that T_{xy} represents the temperature at which the short-range order in the system changes.

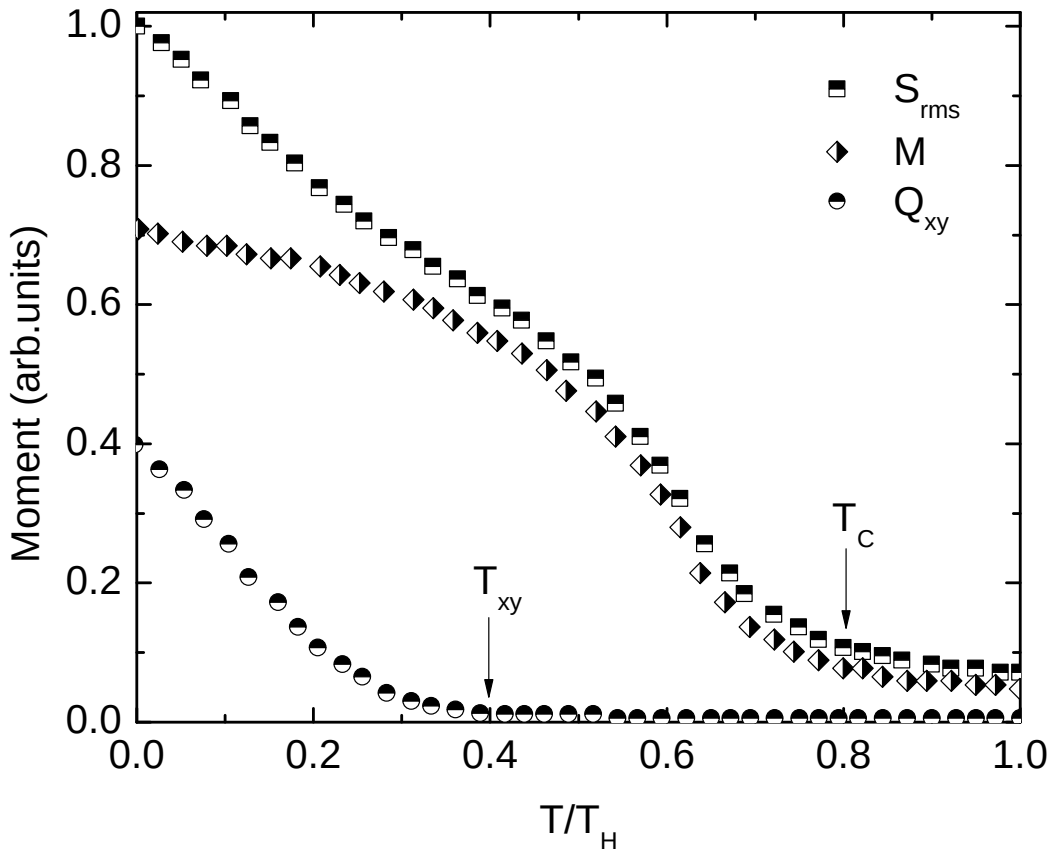

Figure 1.10: Temperature dependence of total static ordered moment S_{rms}, bulk magnetization M, and transverse spin freezing order parameter Q_{xy} as calculated with the Monte Carlo method for the Heisenberg ferromagnet with randomly replaced antiferromagnetic bonds [34]. T_C is the Curie temperature, and T_{xy} is the temperature below which transverse spin freezing occurs. The scale is normalized to the ferromagnetic transition temperature T_H for a Heisenberg system without any AF bonds.

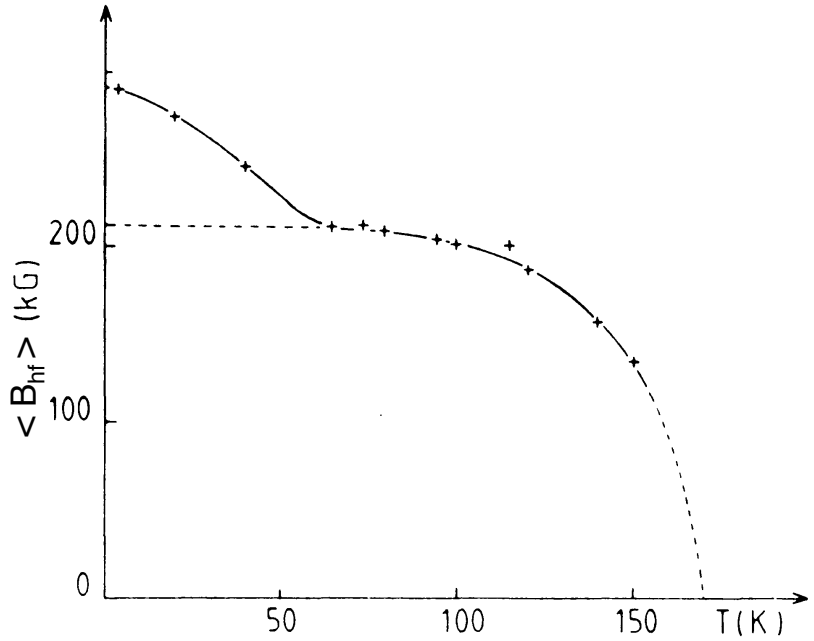

Figure 1.11: Evolution of the mean hyperfine field $< B_{hf} >$ in AuFe, which shows a rapid increase below $\sim$ 60 K indicative of spin canting [37].

1.4 Experimental realization of coexisting LRO-SG

Experimentally, many compounds have been reported to show the coexistence of spin glass and long-range magnetic order (LRO) indicating transverse spin freezing. Au-Fe is one of the first systems in which a FMSG state was observed [36, 37]. In the Fe rich limit, AuFe is a ferromagnet; for Au-15%Fe, the system becomes a spin glass. For slightly higher concentrations, for example in Au-19%Fe, the system first undergoes a ferromagnetic transition at $T_C = 170$ K and transverse spin freezing at $T_{xy} = 60$ K with a non-zero spontaneous magnetization. Another extensively studied material showing a FMSG state is Fe rich Fe_xZr_{100-x} [38]. Spin canting is reported in both of these materials based on the average hyperfine field $< B_{hf} >$ at the Fe site using Mössbauer spectroscopy, as shown in Fig. 1.11 for the Au-Fe system.

The presence of $< B_{hf} >$ in Mössbauer spectroscopy corresponds to a locally ordered magnetic moment at the Mössbauer atom, which gradually grows below the ordering temperature, in this case T_C. In Au-Fe, a rapid increase is observed in $< B_{hf} >$ below $T_{xy} = 60$ K analogous to that of S_{rms} in the numerical calculations (Fig. 1.10), leaving the bulk magnetization nearly unchanged [36, 37].

Ising-like systems such as $Fe_{0.6}Mn_{0.4}TiO_3$ [39, 40] and $Fe_{0.55}Mg_{0.45}Cl_2$ [41] exhibit a coexistence of antiferromagnetism and a spin glass state (AFSG). In these systems, T_{xy} is associated with the appearance of magnetic diffuse scattering under the AF magnetic Bragg peak, as shown in Fig. 1.12a, a feature indicating changes in local magnetic ordering. The intensity of this diffuse scattering increases rapidly on cooling while the intensity of the antiferromagnetic Bragg peak decreases slightly (in Fig. 1.12b).

The above two comparisons show that fairly good agreement exists between numerical and experimental data concerning the coexistence of LRO and SG states. The

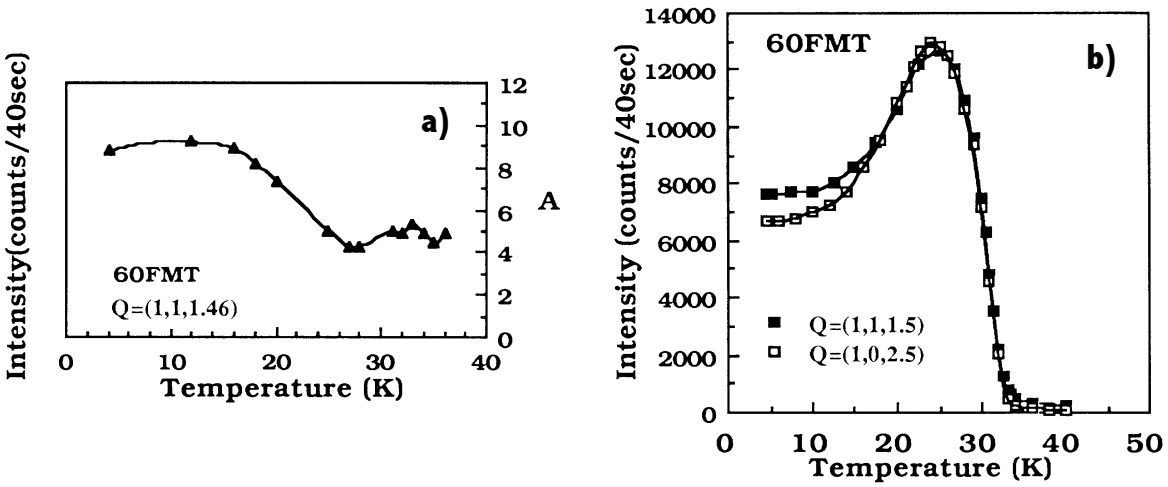

Figure 1.12: Evolution of a) the amplitude of the magnetic diffuse scattering and, b) the antiferromagnetic Bragg peak intensity measured at positions $Q = (1, 1, 1.46)$, $Q = (1, 1, 1.5)$ respectively in $Fe_{0.6}Mn_{0.4}TiO_3$ [39].

numerical results recognize T_{xy} only as an indication of the onset of short-range order, referring to it as a crossover and not a phase transition. However, the boundary between FM and FMSG states predicted by Gabay-Toulouse in the mean field approximation marks it as a true thermodynamic phase transition. Previously, the applicability of this model to real systems suffered from the fact that it led to zero temperatures for the 3d spin glass transition in contrast to the non-zero transition temperature observed in real systems. However, the latest developments considering the chirality of vector spins more or less conclude the presence of a non-zero T_{SG}. In this scenario, the 'mixed phase' or the 'LRO-SG coexistence' as predicted by the Heisenberg SK model and numerical studies is not completely understood in terms of the nature of the transition and the corresponding ground state.

1.4.1 Challenges

A major reason for the incomplete understanding of coexisting LRO-SG states is the lack of an adequate physical realization. Unlike spin glasses, the proof of coexisting LRO and SG ground states suffers from several ambiguities. One of the main experimental challenges involved is sample inhomogeneity. In many disordered materials, for example iron rich Fe-Zr or Fe-Au alloys, the coexistence is debated due to the problem of phase separation [42, 43]. X-ray and neutron scattering studies of Au-Fe identify the segregation of Fe atoms into iron-rich ferromagnetic platelets together with iron-deficient spin glass regions [44, 45]. A similar argument is used for Fe-Zr to explain the temperature behavior of $< B_{hf} >$, indicative of transverse spin freezing. Kaul *et.al.* [46] find that only 90% of the Fe spins contribute to the ferromagnetic structure, leading to speculations of spin clustering. Similarly, Mössbauer spectra of the Ising system $Fe_{0.55}Mg_{0.45}Cl_2$ also indicate the simultaneous presence of clustered and uncoupled Fe moments below the ordering temperature [47].

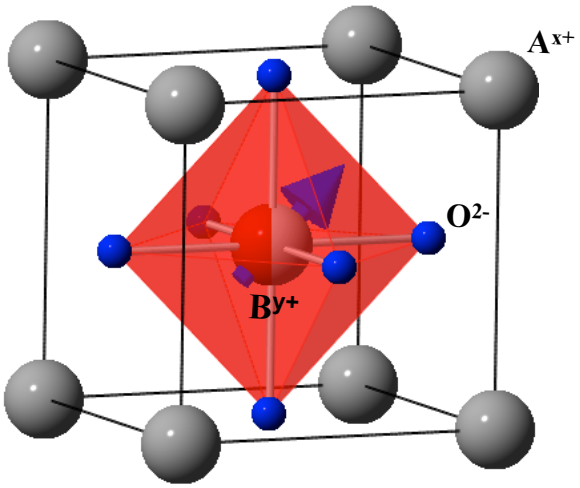

Figure 1.13: Unit cell of the perovskite crystal structure.

Another problem associated with identifying a true LRO-SG coexistence is the incomplete study of the magnetic properties, which could rule out phase separation. For example, one study of a possible AFSG state in $Mg_{1+x}Fe_{2-2x}Ti_xO_4$ [48] involved only microscopic properties whereas other systems such as $Fe_{0.6}Mg_{0.4}TiO_3$ [39] involved only bulk properties. Therefore, the identification of a true mixed state (either FMSG or AFSG) suffers from a lack of any comprehensive study that should ideally combine both bulk momentum-resolved and local magnetic properties.

1.5 Present work

As mentioned in the previous section, one of the major reasons for the lack of a clear experimental proof of coexisting LRO-SG is sample metallurgy. All of the reported compounds showing FMSG or AFSG are generally Fe-containing compounds in which the concentration of iron can be continuously varied. A fundamental disadvantage of continuous dilution is the weak control of the metallurgy of the end product. It is known that samples prepared in this fashion are likely to have a distribution of transition temperatures. Therefore, in order to overcome problems related to phase separation, systems with fixed stoichiometry come across as the best choice to study the FMSG and AFSG states because the position and concentration of the substituted ion is fixed by the stoichiometry.

Perovskites with chemical composition ABO_3 satisfy this condition. These are oxides where A, B refer to two different cations, and B generally being a 3d-transition metal ion, such that the composition of A, B in $A^{x+}B^{y+}O_3^{2-}$ is defined by the requirement of charge neutrality. Crystal structures of perovskites are generally described by a simple cubic structure as shown in Fig. 1.13. Here, oxygen ions are placed at face centers of the cube, A ions occupy corners of the cube and B ions sit at the body center forming a BO_6 octahedra. However, depending on the ionic radii r_A, r_B, r_O of ions A^{x+}, B^{y+} and O^{2-} respectively, the structure may distort. The measure of the distortion is given by a so called tolerance factor ($T.F$) defined as:

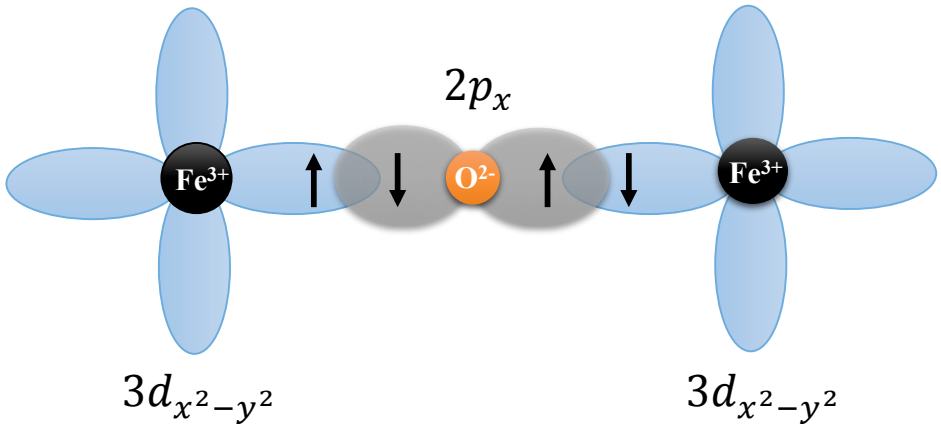

Figure 1.14: The indirect exchange interaction between two magnetic Fe^{3+} ions mediated by the non-magnetic oxygen ion.

$$T.F = \frac{r_A + r_O}{\sqrt{2}(r_B + r_O)}.$$

For T.F=1, the crystal structure is perfectly cubic and any deviation from this value leads to distortion into Rhombohedral (T.F<1) or Hexagonal structures (T.F>1). Disorder can be introduced in these systems by substituting a fraction of the A atoms or B atoms by A′ or B′ atoms respectively, so that charge neutrality is maintained.

A large number of perovskites have a magnetic ion at the B-site, leading to interesting physical properties. Some of them include long-range magnetic order, giant magnetoresistance, superconductivity, etc. In many magnetic materials the direct exchange interactions involving a direct overlap of orbitals between the magnetic ions are known to play the key role in determining long-range magnetic order. However, in a perovskite the magnetic ions are placed far from each other and are separated by oxygen ions. Therefore, the direct exchange interaction is too weak to be responsible for long-range order. On the other hand, there is an indirect exchange interaction between the two magnetic ions mediated by the oxygen ions, which generally leads to antiferromagnetic ordering. In this mechanism, the d orbital of one magnetic transition metal ion overlaps with the p orbital of the oxygen ion which then hybridizes with the d orbital of the next magnetic transition metal ion. In an octahedral environment, this picture can be illustrated as in Fig. 1.14 for an Fe^{3+}-O^{2-}-Fe^{3+} exchange path. In the Fe^{3+} state, each of the five 3d-orbitals $d_{3z^2-r^2}$, $d_{x^2-y^2}$, d_{xy}, d_{yz}, and d_{xz} contain one electron and each of the p_x, p_y, and p_x 2p-orbitals of the O^{2-} contain two electrons. The system energy is minimized when the $3d_{x^2-y^2}$ and p_x orbitals lie on the Fe-O-Fe bond axis. This bond stabilizes into an antiferromagnetic coupling due to Pauli's exclusion rule when the 2p-3d orbitals overlap so that the electrons in these orbitals are delocalized.

$PbB_xB'_{1-x}O_3$ is a class of perovskites where the B-site is randomly filled with B or B′ ions over the whole sample. If one of these B-site ions is magnetic, antiferromagnetic order is generally observed [49]. The chemical disorder at the B-site in these systems has lead to the discovery of a new kind of ferroelectricity known 'relaxors'. Relaxors do not show conventional ferroelectric ordering but only a broad maximum in the

dielectric constant that is frequency dependent [50]. For this reason, most of the work on these materials has been targeted at developing possible multiferroic system. However, the inherent disorder present in these antiferromagnets may lead to complex phase diagrams and exotic ground states. In this work, four compounds are considered from the family of Pb-based disordered perovskites namely, $PbFe_{1/2}Nb_{1/2}O_3$ (PFN), $PbFe_{1/2}Ta_{1/2}O_3$ (PFT), $PbFe_{2/3}W_{1/3}O_3$ (PFW), $PbCo_{1/3}Nb_{2/3}O_3$ (PCN) [51].

Much of the earlier research on these materials has revolved around studies of the magneto-electric (multiferroic) properties occurring at the dielectric maximum T_m or at the Néel transition T_N, which are well above 100 K. Therefore, little is known about the low temperature magnetism in these materials. In fact, even the presence of a Néel transition is uncertain in some cases, for example in PCN. Therefore, this work is aimed at developing a better understanding of the magnetic ground states of these disordered antiferromagnets via the systematic study of the magnetic properties in the following relaxor ferroelectrics:

1. $PbFe_{1/2}Nb_{1/2}O_3$ (PFN) to probe the magnetic ground state of a disordered antiferromagnet, which is a AFSG state.

2. $PbFe_{1/2}Ta_{1/2}O_3$ (PFT), to understand the role of the non-magnetic B-site cation on the AFSG state.

3. $PbFe_{2/3}W_{1/3}O_3$ (PFW), to understand the effect of higher magnetic ion concentration and the effect of displacement of all the ions present in the unit cell, on the AFSG state.

4. $PbCo_{1/3}Nb_{2/3}O_3$ (PCN), to understand the effect of lower magnetic ion concentration on the AFSG state.

To obtain an overview of the magnetic transitions in these materials, bulk magnetization techniques were used on both ceramic and single crystal samples. A deeper analysis was carried out using neutron diffraction, Mössbauer spectroscopy and μ^+SR techniques. While neutron scattering and bulk magnetization provide information about the magnetic moment averaged over the whole sample, Mössbauer spectroscopy and μ^+SR probe magnetic fields on a microscopic scale. Therefore, the combined use of these techniques enables the identification of a true coexisting AFSG state.

1.6 Thesis Outline

Thesis chapters are structured as follows:

- The second chapter presents the experimental techniques used in this work: it describes the basics of neutron scattering, Mössbauer spectroscopy, and μ^+SR techniques. The instrumentation involved in all these techniques is also briefly discussed.

- The magnetic properties of PFN are presented in the 3rd chapter. Results from bulk magnetization, neutron scattering and Mössbauer spectroscopy are interpreted to prove the coexistence of antiferromagnetism and spin glass states (AFSG) in this material. A model to explain such a coexistence is presented. The transition temperature

T_{SG} below which the coexistence occurs has been presented as a function of external field and hydrostatic pressure.

- The 4th chapter is dedicated to understanding the effect of the non-magnetic ion on the presence of AFSG by showing data for PFT . As in PFN , the magnetic phase diagram of PFT is also presented based on above mentioned bulk and local techniques. The results unambiguously prove that the phase diagram of PFT is identical to that for PFN .

- In the 5th chapter, the results of magnetization measurements are presented in two parts, one each for PFW and PCN , in order to probe the effect of the magnetic ion concentration on AFSG state. The results include bulk magnetization, neutron diffraction, Mössbauer spectroscopy, and μ^+SR spectroscopy revealing that neither of the compounds exhibit the AFSG state.

Chapter 2

Experimental Methods

2.1 Neutron Scattering

2.1.1 Neutron

The neutron is an elementary particle that has zero electric charge but non-zero magnetic dipole, which gives rise to two possible interactions with matter: 1) a nuclear interaction, 2) a magnetic interaction. When incident on an atom, the neutron directly interacts with the nucleus and is transparent to the electron cloud due to its charge neutrality. However, if the atom has unpaired electrons, it has a magnetic moment that interacts with the neutron's magnetic moment. These two interactions together make neutrons a very useful probe of nuclear and magnetic states of condensed matter using the neutron scattering technique.

2.1.2 Scattering cross-section

The relevant physical quantity in a scattering experiment is the scattering cross-section. If we consider the scattering of a beam of neutrons carrying energy E_i from a target material, the differential scattering cross-section can be defined as the number of neutrons scattered per second into a solid angle Ω in a specific direction whose final energy lies between E_f, $E_f + dE_f$ normalized to the flux of incoming neutrons. This differential cross-section is denoted as $\frac{d^2\sigma}{d\Omega dE_f}$.

Let us assume that interaction potential between neutron and the target is V. Then, the scattering event is accompanied by a transition of scattering system from λ_i state to λ_f and neutron's momentum changes from $\vec{k}_i$ to $\vec{k}_f$, energy from E_i to E_f and spin from σ_i to σ_f. Therefore, the cross-section depends directly on the probability of the transition of the scattering system from λ_i to λ_f having energy E_{λ_i}, E_{λ_f} respectively. In quantum mechanics, this transition probability is described by *Fermi's Golden Rule*.

According to *Fermi's Golden Rule*, the transition probability $\sum_{\boldsymbol{k_f}} T_{\boldsymbol{k_i},\lambda_i \to \boldsymbol{k_f},\lambda_f} = \frac{|\boldsymbol{k_f}|}{|\boldsymbol{k_i}|} |\langle \boldsymbol{k_f}\sigma_f\lambda_f|V|\boldsymbol{k_i}\sigma_i\lambda_i\rangle|^2$

$$\frac{d^2\sigma}{d\Omega dE_f} = \frac{|\boldsymbol{k_f}|}{|\boldsymbol{k_i}|}\left(\frac{m}{2\pi\hbar}\right)^2 |\langle \boldsymbol{k_f}\sigma_f\lambda_f|V|\boldsymbol{k_i}\sigma_i\lambda_i\rangle|^2 \delta(E_{\lambda_i} - E_{\lambda_f} + E_i - E_f) \tag{2.1}$$

When summed over all possible initial and final states λ_i and λ_f of the target system ,

$$\frac{d^2\sigma}{d\Omega dE_f} = \frac{|\boldsymbol{k_f}|}{|\boldsymbol{k_i}|}\left(\frac{m}{2\pi\hbar}\right)^2 \sum_{\lambda_i} p_{\lambda_i} \sum_{\lambda_f} |\langle \boldsymbol{k_f}\sigma_f\lambda_f|V|\boldsymbol{k_i}\sigma_i\lambda_i\rangle|^2 \delta(E_{\lambda_i} - E_{\lambda_f} + E_i - E_f) \quad (2.2)$$

2.1.3 Nuclear Scattering

In a solid, the interaction potential of neutron with the nucleii can be given by: $V = \sum_j \frac{2\pi\hbar 2}{m} b_j \delta(\mathbf{r} - \mathbf{R_j})$ where, $\mathbf{r}$ is the distance of neutron from an atom positioned at $\mathbf{R_j}$ having a *scattering length* b_j. Therefore, the matrix element in terms of the change in neutron state is $|\langle \boldsymbol{k_f}|V|\boldsymbol{k_i}\rangle|$. As the neutron wave function can be described by plane wave $e^{i\boldsymbol{k_i}\cdot\mathbf{r}}$ and $e^{i\boldsymbol{k_f}\cdot\mathbf{r}}$ respectively,

$$|\langle \boldsymbol{k_f}|V|\boldsymbol{k_i}\rangle| = \frac{2\pi\hbar^2}{m}\sum_j b_j e^{i\boldsymbol{k}\cdot\mathbf{R_j}}. \quad (2.3)$$

Here, $\boldsymbol{k} = \boldsymbol{k_i} - \boldsymbol{k_f}$ is known as the *scattering vector* such that $\hbar\boldsymbol{k}$ denotes the momentum transfer invovled in the scattering. The differential scattering cross-section for nuclear scattering can be written as:

$$\frac{d^2\sigma}{d\Omega dE_f} = \frac{|\boldsymbol{k_f}|}{|\boldsymbol{k_i}|}\sum_{\lambda_i} p_{\lambda_i} \sum_{\lambda_f} |\langle\lambda_f|\sum_j b_j e^{i\boldsymbol{k}\cdot\mathbf{R_j}}|\lambda_i\rangle|^2 \delta(E_{\lambda_i} - E_{\lambda_f} + E_i - E_f). \quad (2.4)$$

Using time-dependent Heisenberg operators and integral form of $\delta-$function for energy,

$$\frac{d^2\sigma}{d\Omega dE_f} = \frac{|\boldsymbol{k_f}|}{|\boldsymbol{k_i}|}\frac{1}{2\pi\hbar}\sum_{jj'} b_j b_{j'} \int_{-\infty}^{+\infty} < e^{i\boldsymbol{k}\cdot\mathbf{R_{j'}(0)}} e^{i\boldsymbol{k}\cdot\mathbf{R_j(t)}} > e^{-i\omega t} dt \quad (2.5)$$

$$\text{where } < e^{i\boldsymbol{k}\cdot\mathbf{R_{j'}(0)}} e^{i\boldsymbol{k}\cdot\mathbf{R_j(t)}} > = \sum_\lambda p_\lambda < \lambda|e^{i\boldsymbol{k}\cdot\mathbf{R_{j'}(0)}} e^{i\boldsymbol{k}\cdot\mathbf{R_j(t)}}|\lambda >$$

is the thermal average.

If all the nucleii have same scattering length b,

$$\begin{aligned} \frac{d^2\sigma}{d\Omega dE_f} &= \frac{|\boldsymbol{k_f}|}{|\boldsymbol{k_i}|} N b^2 S(\boldsymbol{k},\omega) \\ S(\boldsymbol{k},\omega) &= \frac{1}{N}\frac{1}{2\pi\hbar}\sum_{jj'}\int_{-\infty}^{+\infty} < e^{i\boldsymbol{k}\cdot\mathbf{R_{j'}(0)}} e^{i\boldsymbol{k}\cdot\mathbf{R_j(t)}} > e^{-i\omega t} dt \end{aligned} \quad (2.6)$$

known as *scattering function* in which $\omega = \frac{1}{\hbar}(E_i - E_f)$ is the energy transferred by neutron to the scattering system containing N atoms.

2.1.4 Magnetic Scattering

Dipole moment of neutron is $\boldsymbol{\mu}_n = \gamma\mu_N\boldsymbol{\sigma}$. If the target system has N electrons each with magnetic moment $\boldsymbol{\mu}_e = -2\mu_B\boldsymbol{s}$, the magnetic field produced by one electron at some distance r is $\boldsymbol{B} = \boldsymbol{B}_{dipole} + \boldsymbol{B}_{orbital}$. The interaction of this magnetic field with neutron dipole moment is given by $V = -\boldsymbol{\mu}_n \cdot \boldsymbol{B}$ such that the magnetic scattering is written as:

$$\frac{d^2\sigma}{d\Omega dE_f} = \frac{|\boldsymbol{k_f}|}{|\boldsymbol{k_i}|}(\gamma r_0)^2 |\langle \boldsymbol{k_f}\sigma_f\lambda_f|\boldsymbol{\sigma}\cdot\boldsymbol{M}_\perp|\boldsymbol{k_i}\sigma_i\lambda_i\rangle|^2 \delta(E_{\lambda_i} - E_{\lambda_f} + E_i - E_f) \tag{2.7}$$

where $\boldsymbol{M}_\perp = -\frac{1}{2\mu_B}\cdot\hat{\boldsymbol{k}}\times(\boldsymbol{M}(\boldsymbol{k})\times\hat{\boldsymbol{k}}) = -\frac{1}{2\mu_B}\left[\boldsymbol{M}(\boldsymbol{k}) - (\boldsymbol{M}(\boldsymbol{k})\cdot\hat{\boldsymbol{k}})\hat{\boldsymbol{k}}\right]$ for $\boldsymbol{M}(\boldsymbol{k})$ being the Fourier transform of total magnetization operator $\boldsymbol{M}(\boldsymbol{r})$. Therefore, $\boldsymbol{M}_\perp$ is directly related to the magnetization of the target system.

Similar to nuclear scattering, the cross-section can be written as

$$\begin{aligned} \frac{d^2\sigma}{d\Omega dE_f} &= \frac{|\boldsymbol{k_f}|}{|\boldsymbol{k_i}|} N(\gamma r_0)^2 S(\boldsymbol{k},\omega) \\ S(\boldsymbol{k},\omega) &= \frac{1}{N}\frac{1}{2\pi\hbar}\sum_{nn'}(\delta_{nn'} - \hat{k_n}\hat{k_{n'}})\int_{-\infty}^{+\infty} < M_n(-\boldsymbol{k},0)M_{n'}(\boldsymbol{k},t) > e^{-i\omega t}dt \end{aligned} \tag{2.8}$$

n, n' are x, y and z components.

Eq. 2.6 and Eq. 2.8 reveal that the scattering function $S(\boldsymbol{k},\omega)$ contains all the information about correlations in the target system and hence is the only physical quantity of interest in a neutron scattering experiment.

2.1.5 Neutron Diffraction

For a single crystal the position of nucleus R_j in Eq. 2.6 can be written as $R_j = j + u_j$ when nucleus vibrates with a displacement u_j. Then, the coherent elastic scattering cross-section can be obtained by integrating Eq. 2.6 for all the final energies.

$$\frac{d\sigma}{d\Omega} = \int_0^{+\infty}\left(\frac{d^2\sigma}{d\Omega dE_f}\right)dE_f \tag{2.9}$$

$$\frac{d\sigma}{d\Omega} = Nb^2\frac{(2\pi)^3}{V_c}e^{-2W}\sum_{\boldsymbol{G}}\delta(\boldsymbol{k}-\boldsymbol{G}) \tag{2.10}$$

where, V_c is the volume of unit cell in the crystal, $2W =< (\boldsymbol{k}\cdot u_0(0))^2 >$ is the Debye-Waller factor and $\boldsymbol{G}$ is the reciprocal lattice vector of the crystal. Therefore, the scattering is non-zero only when the momentum transfer equals that of the reciprocal lattice vector.

If the unit cell has a basis situated at distance l from the origin of the unit cell, the scattering takes following form:

$$\begin{aligned} \frac{d\sigma}{d\Omega} &= N\frac{(2\pi)^3}{V_c}\sum_{\boldsymbol{G}}\delta(\boldsymbol{k}-\boldsymbol{G})|F_N(\boldsymbol{k})|^2 \\ \text{where, } F_N(\boldsymbol{k}) &= \sum_{\boldsymbol{l}} b_l e^{i\boldsymbol{k}.\boldsymbol{l}} e^{-W_l} \text{is the } \textit{structure factor}. \end{aligned} \tag{2.11}$$

For a magnetic unit cell the coherent elastic scattering is given as:

$$\begin{aligned} \frac{d\sigma}{d\Omega} &= N_m\frac{(2\pi)^3}{V_m}\sum_{\boldsymbol{G_m}}\delta(\boldsymbol{k}-\boldsymbol{G_m})|F_m(\boldsymbol{k})|^2 \\ \text{where, } F_m(\boldsymbol{k}) &= \sum_{\boldsymbol{l}} (\gamma r_0)\frac{1}{2} g f(\boldsymbol{k}) \boldsymbol{M}_\perp e^{i\boldsymbol{k}.\boldsymbol{l}} e^{-W_l} \text{is the } \textit{structure factor}. \end{aligned} \tag{2.12}$$

Here, $f(\boldsymbol{k})$ is the *magnetic form factor* and it is the Fourier transform of normalized spin density of the ion l, $\boldsymbol{G_m}$ is the magnetic propagation vector, V_m is the volume of magnetic unit cell and N_m is the number of magnetic unit cells in the crystal.

2.1.6 Polarization analysis

For magnetic crystals, it is possible to separate out the magnetic scattering from its nuclear counterpart by using polarized neutrons. As mentioned in the section 2.1.4, the magnetic scattering is given by Eq. 2.8. If we consider spin states of neutron to be $\alpha = \frac{1}{2}\hbar\boldsymbol{\sigma}$ and $\beta = -\frac{1}{2}\hbar\boldsymbol{\sigma}$, the neutron spin-state transition depends on both nuclear moments as well as magnetic moments due to unpaired electrons in the magnetic ions and is written as $< \sigma_f\lambda_f|\sum_l C_l e^{i\boldsymbol{k}.R_l}|\sigma_i\lambda_i >$.

Here, $C_l = (\boldsymbol{A}_l + \boldsymbol{B}_l\boldsymbol{\sigma}\cdot\boldsymbol{I}_l) + \boldsymbol{\sigma}\cdot\boldsymbol{M}_\perp$, $\boldsymbol{A}$ and $\boldsymbol{B}$ are related to isotope dependent scattering lengths $\bar{b}$, $\boldsymbol{I}$ the angular momentum of the scattering nuclei. Then, the polarization dependent transition matrix for an atom has following possibilities:

$$\begin{aligned} &< \alpha|C_l|\alpha > = \bar{b} - M_{\perp z} \\ &< \beta|C_l|\beta > = \bar{b} + M_{\perp z} \\ &< \alpha|C_l|\beta > = (M_{\perp x} - iM_{\perp y}) \\ &< \beta|C_l|\alpha > = -(M_{\perp x} + iM_{\perp y}) \end{aligned} \tag{2.13}$$

As mentioned earlier, $\boldsymbol{M}_\perp = -\frac{1}{2\mu_B}\cdot\hat{\boldsymbol{k}}\times(\boldsymbol{M}(\boldsymbol{k})\times\hat{\boldsymbol{k}})$. Therefore, if the incident neutron beam is polarized and has a polarization vector $\boldsymbol{P}$ the scattered neutron intensity from a magnetically ordered crystal will follow one of the Eq. 2.13. The four transitions can be categorized as spin-flip and non spin-flip processes. From the equations above it is evident that the spin-flip transitions are purely magnetic whereas non spin-flip is a superposition of both nuclear and magnetic scattering.

By choosing a proper direction of the scattering vector $\boldsymbol{k}$ relative to the polarization vector $\boldsymbol{P}$ one can analyze the magnetic contribution of the scattering.

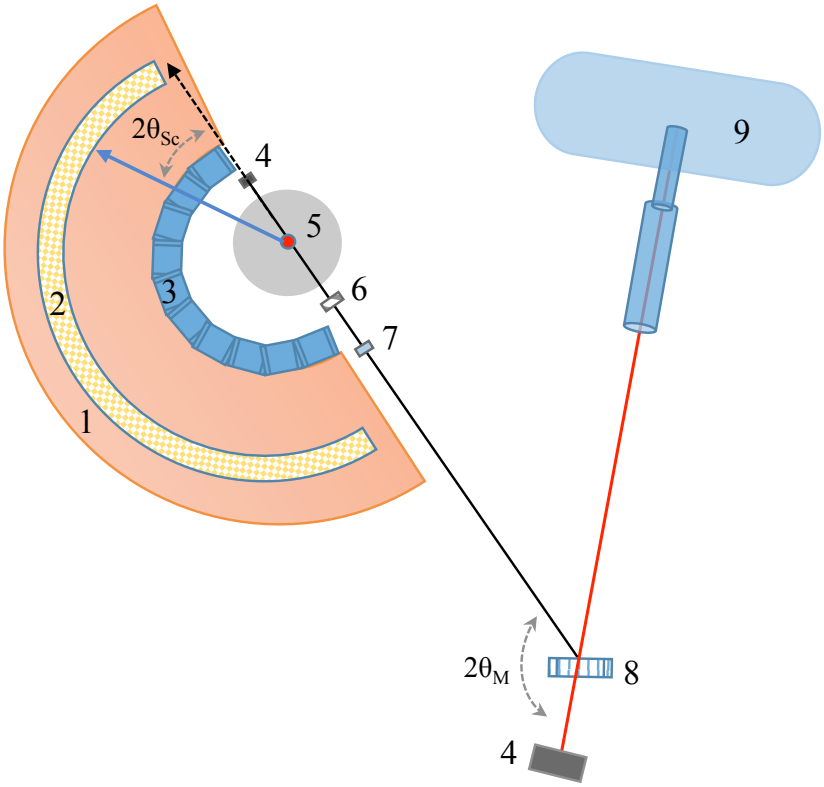

Figure 2.1: Schematic of the HRPT powder diffractometer at Paul Scherrer Institut. Components of the instrument are: 1) Detector shielding, 2) Array of He^3 detectors, 3) Radial Collimators, 4) Beam stopper, 5) Sample mounted on the sample table, 6) vertical/horizontal slits, 7) Monitor, 8) Pyrolytic Graphite monochromator, 9) Neutron moderator pool.

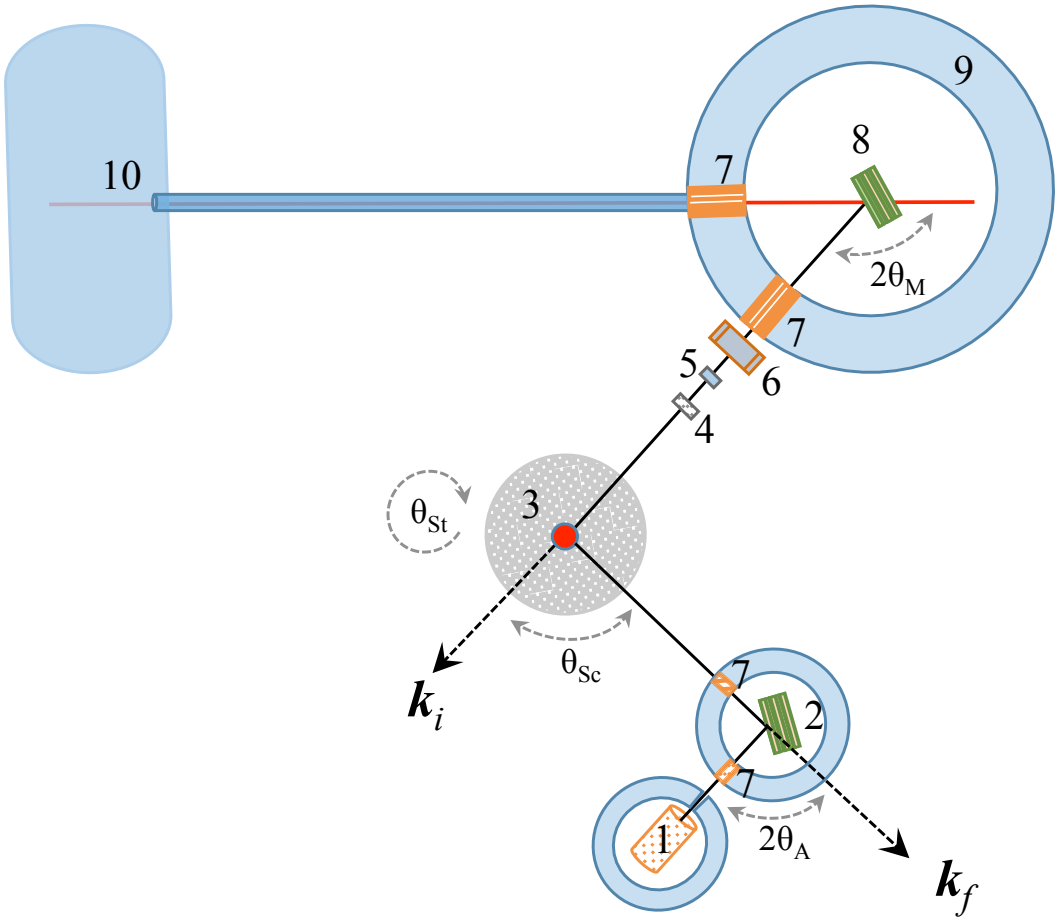

Figure 2.2: Schematic of the TASP triple axis spectrometer at Paul Scherrer Institut with 1) He^3 detector, 2) and 8) monochromator and analyzer crystals of Pyrolytic Graphite, 3) Sample table & sample, 4) vertical/horizontal slits, 5) monitor, 6) filter, 7) Soller collimators, 9) Schielding, 10) Neutron moderator pool.

2.1.7 Instrumentation

In the present work, determination of crystal and magnetic structure of powder PFW is obtained through neutron powder diffraction at HRPT (High Resolution Powder diffractometer for Thermal neutrons) in PSI. The diffractometer uses a monochromatic beam of neutrons for the scattering. The scattered neutrons pass through radial collimators and are detected by an array of He^3 detectors. The detectors cover an angle of 160 °. A schematic of the diffractometer is given in Fig. 2.1. For further details of the instrument refer to the link [52].

For a scattering from single crystal, momentum and energy conservation are written as follows:

Momentum conservation:

$$\boldsymbol{k} = \boldsymbol{G} + \boldsymbol{q} = \boldsymbol{k_f} - \boldsymbol{k_i}$$

with magnitude:

$$k^2 = k_i^2 + k_f^2 - 2\boldsymbol{k_i}.\boldsymbol{k_f}$$

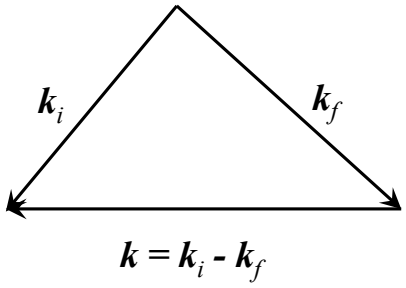

Figure 2.3: The scattering vector configuration for TASP.

Energy conservation:

$$\hbar\omega(\boldsymbol{q}) = E_f - E_i$$

In the case of elastic scattering energy transfer to the neutron is zero and hence scattering in a Brillouin zone can be measured as a function of momentum transfer $\boldsymbol{q}$. If in addition, the momentum transfer is also zero, the Bragg scattering is measured. Such freedom of controlling energy and momentum transfer is allowed by a triple axis spectrometer. In the present work, the antiferromagnetic order parameter in PFN and magnetic short range order in PFT are measured on single crystal samples using triple axis spectrometer TASP at PSI. Fig. 2.2 is the schematic of cold neutron spectrometer TASP whose scattering configuration with respect to scattering vector can be depicted as in Fig. 2.3. As components of the spectrometer are not ideal, for example, small but finite mosaicity of the analyzer/monochromator single crystals, the spectrometer has a finite resolution in energy and momentum transfer. Therefore, the scattered signal is a convolution of *resoltuion function* and *target response function*. A more detailed description of the resolution function can be found at [53]. For further details of the TASP spectrometer specifications please refer [54].

One of the extensions of triple axis spectrometer is the polarization analysis of magnetic crystals. For this, a polarized beam of neutrons is incident on the sample and the change in polarization due to sample's magnetization is revealed in the scattered beam of neutrons. Fig. 2.4 shows MuPAD setup at TASP used for polarization analysis of the diffuse scattering in PFT appearing under antiferromagnetic Bragg peak. The setup consists of two sets of coupling coils, guide field coils. Each set of the coils is used for aligning the initial polarization of the incoming neutrons and analyzing the final polarization after the scattering event. With MuPAD it is possible to obtain all elements of the $\boldsymbol{P}_{if}$ matrix where $i, f = x, y$ and z directions. The schematic shows scattering direction for the case of polarization vector $\boldsymbol{P_i}$ parallel to scattering vector $\boldsymbol{k}$. If the initial neutron polarization and $\boldsymbol{k}$ are along $z-$axis, the condition for magnetic scattering i.e, $\boldsymbol{M}_\perp = -\frac{1}{2\mu_B} \cdot \hat{\boldsymbol{k}} \times (\boldsymbol{M}(\boldsymbol{k}) \times \hat{\boldsymbol{k}})$, allows only $\boldsymbol{M}_{\perp \boldsymbol{x}}$ and $\boldsymbol{M}_{\perp \boldsymbol{y}}$ components. Therefore, Eq. 2.13 shows that spin flip channel is of purely magnetic origin. On the other hand, non-spin flip channel has only terms of nuclear origin.

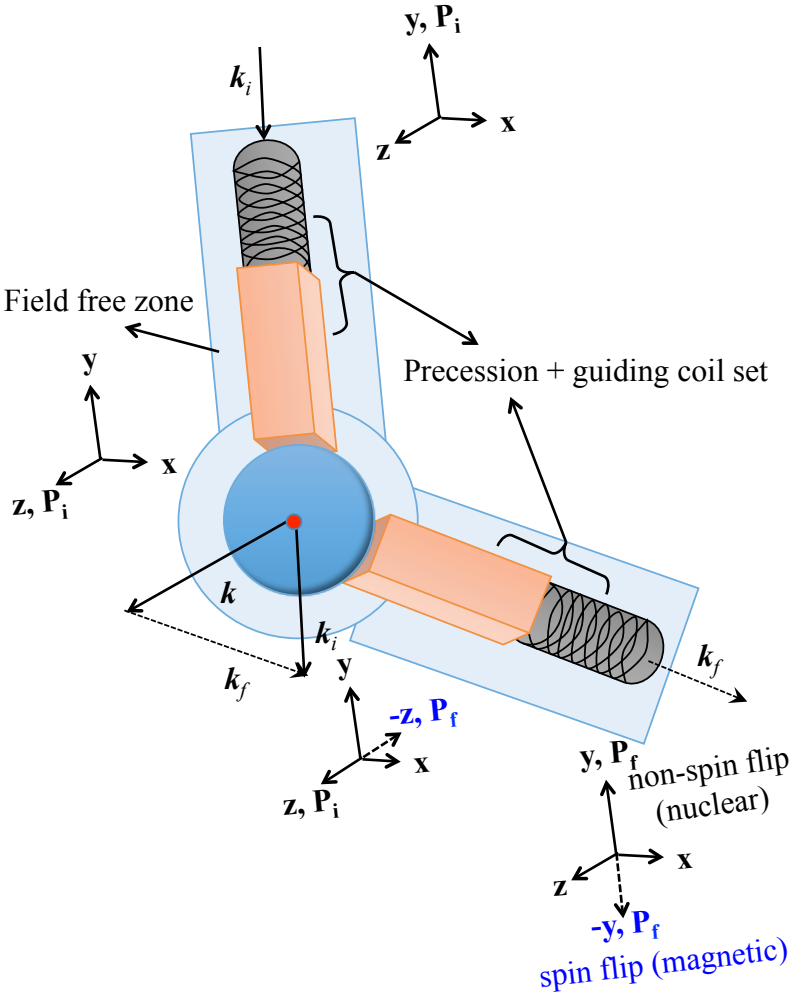

Figure 2.4: Schematic of polarization analysis setup for MuPAD at triple-axis spectrometer TASP.

2.2 Mössbauer Spectroscopy

Mössbauer spectroscopy is another tool which provides valuable information on the magnetic and structural environment of magnetic nuclei of a system. This technique uses the interaction of electromagnetic moment of the nucleus with the surrounding electronic environment leading to shifting and/or splitting of the nuclear energy levels. This is generally known as hyperfine interaction. By quantifying the changes involved in the nuclear energy levels one can obtain information on valency, structural symmetry, covalent bonding and the magnetic ordering of a Mössbauer nucleus in the target system.

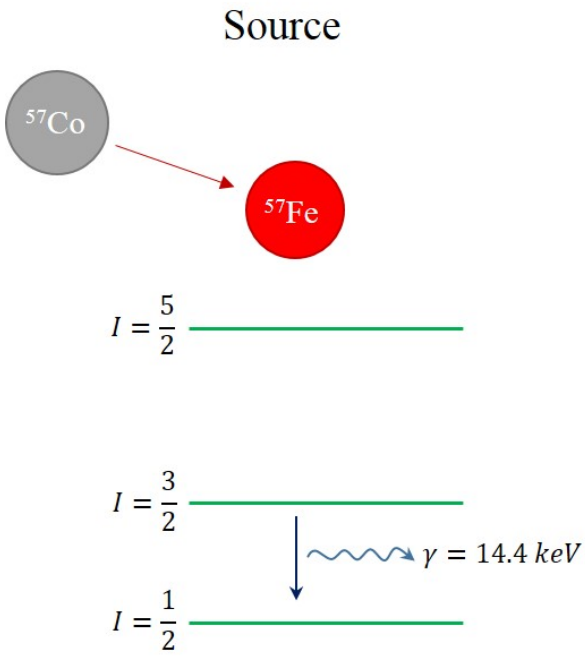

Figure 2.5: Energy level schematic of the γ-rays source ^{57}Fe Mössbauer spectrocsopy.

Mössbauer spectroscopy is a γ-ray transmission/absorption spectroscopy in which the γ-rays are produced by the decay of nuclear levels from excited to ground state. As the nuclear levels are very well defined, the emitted γ-ray energies are restricted to the difference of energy levels E_0. However, a significant amount of this energy is lost to the recoil of the decaying nucleus owing to the conservation of momentum and energy of the process. This in turn, greatly reduces/prohibits the probability of emitted γ-ray to be absorbed by a similar nucleus. If we assume that the mass of decaying nucleus is M and energy of the emitted γ-ray is E_γ, the recoil energy E_{Recoil} is given by:

$$E_{Recoil} = \frac{E_0^2}{2MC^2}$$

Meaning that the mass of the nucleus must be large enough to have a negligible in order to produce γ-rays for an absorption experiment. Many such nuclei can be found in the periodic table of elements. However, ^{57}Fe is a widely studied nucleus as well as the focus of this work and therefore further details of the technique are based on ^{57}Fe Mössbauer spectroscopy. In the source, ^{57}Fe isotope is a product of natural decay of

^{57}Co nucleus where the γ-rays of energy 14.4 keV are emitted from the decay of ^{57}Fe nucleus from level $I = \frac{3}{2}$ to $I = \frac{1}{2}$ (see Fig. 2.5). The finite life time of the excited state $I = \frac{3}{2}$ gives rise to natural line width of emitted γ photon $\Gamma_0 = 4.67 \times 10^{-9}\ eV$.

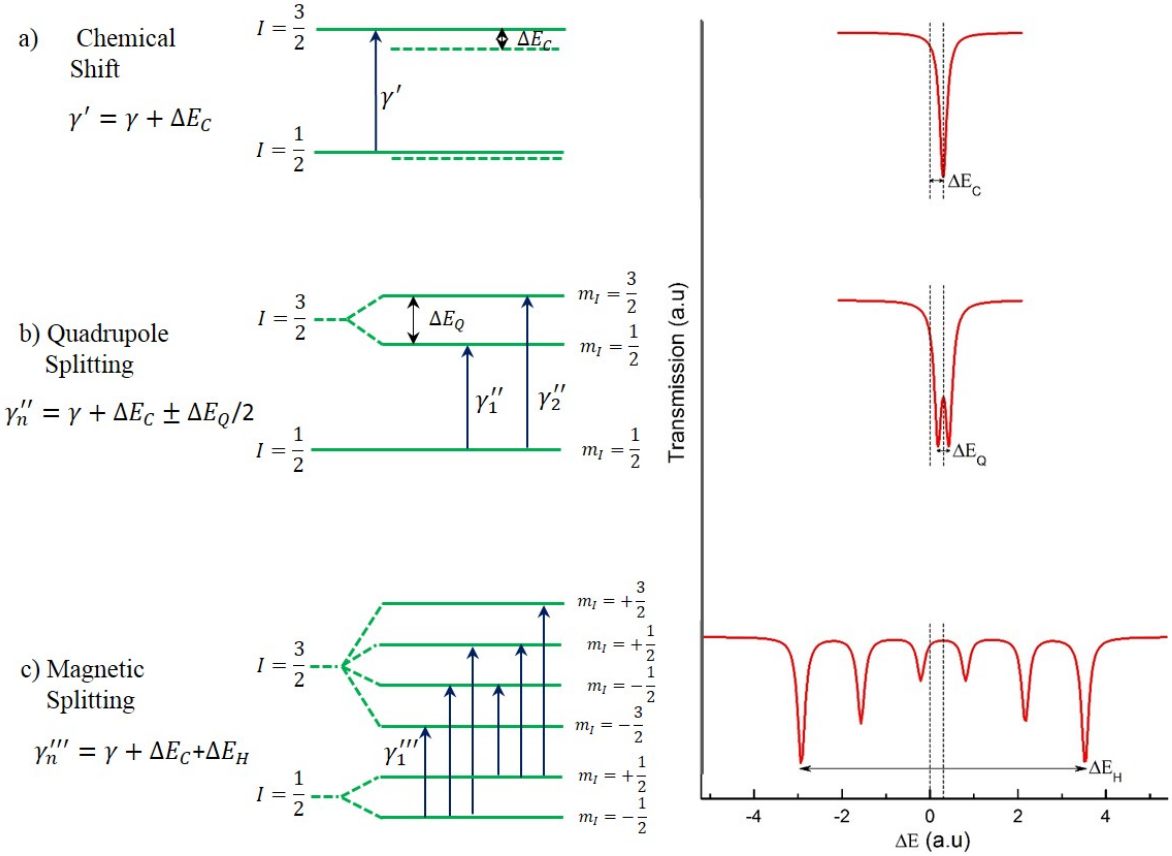

Figure 2.6: Three generally observed hyperfine interactions of Mössbauer nuclei with its lattice: a) Chemical (or isomer) shift, b) Quadrupole splitting and c) Magnetic splitting.

2.2.1 Hyperfine interactions

In a target containing 'Fe' ions, 2.2% of the nuclei are ^{57}Fe isotopes which absorb the Doppler shifted γ-rays emitted by the source nuclei. The resulting spectrum consists of absorption lines relative to the source energy level. Three basic hyperfine interactions of the target ^{57}Fe nuclei define the intensity, shape and position of the absorption lines: 1) Chemical/Isomer shift, 2) Quadrupole Splitting and 3) Zeeman splitting indicated in the right panel of Fig. 2.6. While the first two interactions are directly related to the Coulomb interaction between electron charge cloud and the proton charge distribution within the nucleus, the latter is due to the nuclear magnetic moment in a magnetic field.

Chemical Shift:

The interaction of total charge of nucleus surrounded by the total electron density shifts the ^{57}Fe nuclear energy levels. Therefore, the excitation of nucleus from $I = \frac{3}{2}$ to $I = \frac{1}{2}$ occurs at energy $E_0 + \Delta E_C$. This additional energy ΔE_C is referred to as the isomer/chemical shift and is given by:

$$\Delta E_C = \text{const.}(\rho_t - \rho_s)(R_{3/2}^2 - R_{1/2}^2)$$

where ρ_t, ρ_s are the total electron densities of target and source respectively, $R_{3/2}$, $R_{1/2}$ are radii of the nucleus in excited and ground state respectively. As the shift depends on the total electron density which in turn depends on the oxidation state of the atom, this quantity directly yields information about the valence of the target Mössbauer atom.

Quadrupole Splitting:

The nuclei with non-spherical charge distribution, i.e, if the nuclei are in states with total nuclear angular momentum $I > 1/2$, possess a quadrupole moment. When there is an asymmetric electric field around the nucleus, quadrupole moment interacts with a tensorial quantity called electric field gradient (EFG) which is a result of an asymmetric electronic charge distribution. This gives rise to the splitting of nuclear energy levels $I > 1/2$, for example $I = 3/2$ splits into two sub-levels corresponding to $m_I = \pm 1/2$, $m_I = \pm 3/2$ so that a doublet structure appears in the absorption spectrum. The interaction energy for the quadrupole splitting is given by,

$$\Delta E_Q = \frac{eQV_{zz}}{2}[3m_I^2 - I(I+1)](1 + \eta^2/3)^{\frac{1}{2}}$$

where eQ is the nuclear quadrupole moment, V_{zz} is z-component of the EFG, I is nuclear angular momentum, $m_I = I, I-1, ..-I$, $\eta = \frac{V_{xx} - V_{yy}}{V_{zz}}$ is known as the asymmetry parameter.

As the quadrupole moment for a nucleus is fixed the doublet structure is completely defined by EFG. A number of parameters such as asymmetry in the electronic structure of Mössbauer atom, asymmetric arrangement of ligands in a lattice contribute to EFG. Therefore, the quadrupole splitting gives information about the local environment of the Mössbauer atom.

Magnetic Splitting:

The magnetic field at the nucleus in an atom of non-zero spin is made of three contributions namely, contact, orbital and dipolar. The interaction of nuclear magnetic moment with magnetic hyperfine field at the nucleus is given as:

$$\begin{aligned} B_{hf} &= B_{con} + B_{orb} + B_{dip} \\ \Delta E_H &= -g_N \beta_N B_{hf}.I \\ &= -2\mu_B[\text{const.}(\kappa \frac{< \mathbf{S} >}{r^3}) + \frac{< L >}{r^3} + \frac{3\mathbf{r}(\mathbf{S}.\mathbf{r}) - \mathbf{r^2 S}}{r^5} \end{aligned} \tag{2.14}$$

This interaction lifts the degeneracy of nuclear energy levels so that $I = 3/2$ and $I = 1/2$ split into $2I+1$ levels from $-I....+I$. According to the selection rule, $\Delta m_I = 0, \pm 1$, only six of the eight transitions are allowed and corresponding absorption lines appear in the spectrum. Fig. 2.6c indicates the Mössbauer spectrum for magnetically ordered system positioned symmetrically on either side of chemical (or isomer) shift. If the system has qudarupolar splitting in addition to the Zeeman splitting this symmetry of the absorption lines is lifted as depicted in spectra Fig. 2.7.

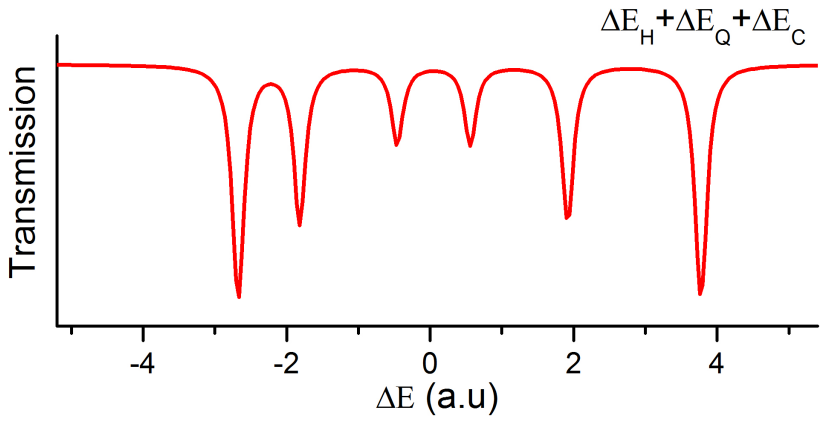

Figure 2.7: A schematic spectrum of Mössbauer transmission in the case of combined magnetic and quadrupole splitting.

2.2.2 Instrumentation

A schematic of the set up used for Mössbauer spectroscopy is shown in Fig. 2.8. It is an ensemble of three modules: mechanically driven source, sample environment, detection and synchronization. The main feature of the Mössbauer spectroscopy is the tuning of γ ray energy to be absorbed by the sample. Generally this is done by the use of Doppler shift which in turn is produced by the motion of source towards and away from the absorber/sample. Hence, the energy seen by ^{57}Fe nuclei in the sample can be written as:

$$\omega' = \frac{c}{c + v_{source}} \omega$$

For ^{57}Fe, a 1 mm/s change in velocity is approximately equivalent to $10\Gamma_0$ (Γ_0 being the natural line width of the emitted γ-ray). This motion of the source/scan in photon energy is synchronized with the observed intensity through a feedback loop by the use of Multichannel analyzer. This allows a real time mapping of the photon energy vs absorption by the Mössbauer nuclei.

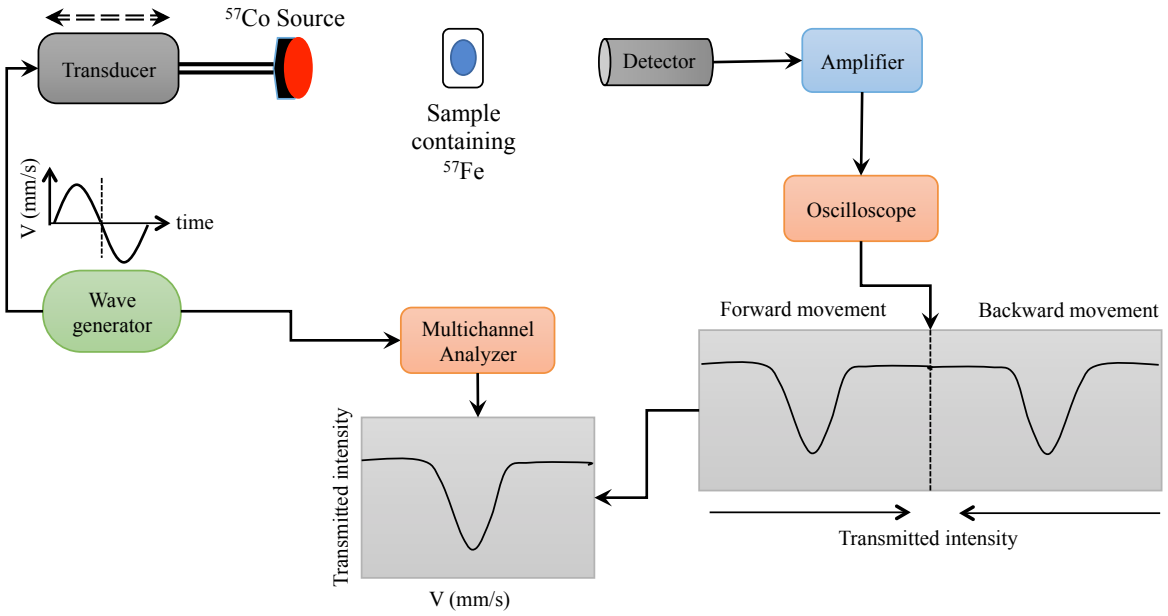

Figure 2.8: Sketch of the measurement setup of Mössbauer spectroscopy.

2.3 Muon Spin Relaxation (μ^+SR)

Muon Relaxation Spectroscopy, generally known as μ^+SR, is a local technique used to understand the structure and dynamics of matter, especially in magnetic materials, and is complimentary to neutron scattering. The technique involves implantation of spin-polarized muons into the target that then decay into positrons. The direction of positron emission is in the direction of muon spin at the time of decay, which in turn depends on its local environment. A time histogram of these emitted positrons contains microscopic information about the target system.

As the moment of the muon is approximately 9 times larger than that of the neutron, it is particularly sensitive in probing samples with small moments. Additionally, it is a highly useful technique to probe random magnetism and short-range order, as the technique yields local information about the sample.

2.3.1 Muon

Muon is a spin-1/2 particle with charge $\pm e$ and 207 times heavier than an electron. Unlike electron, muon has a finite life time of 2.2 μs after which it decays into positron as in the following process.

$$\mu^+ \rightarrow e^+ + \nu_e + \nu_\mu \tag{2.15}$$

2.3.2 Spin precession

In the above decay process direction of the emitted positron is defined by the direction of muon spin at the time of decay. For example, the muon spin precesses in magnetically ordered material around the local internal magnetic field, B_{loc} as shown in the schematic

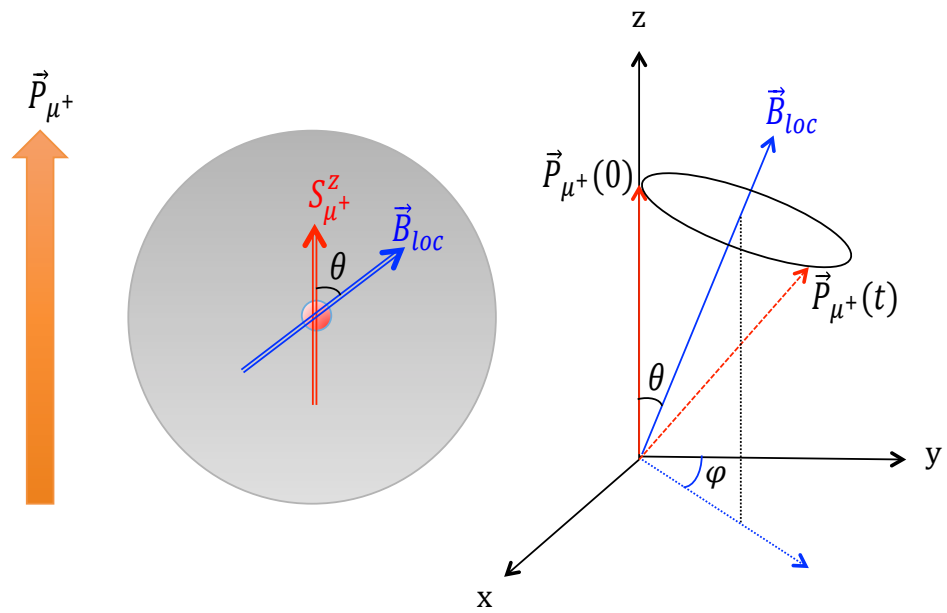

Figure 2.9: Schematic of the muon depolarization due to Larmor precession in the presence of a local magnetic field B_{loc} in the system.

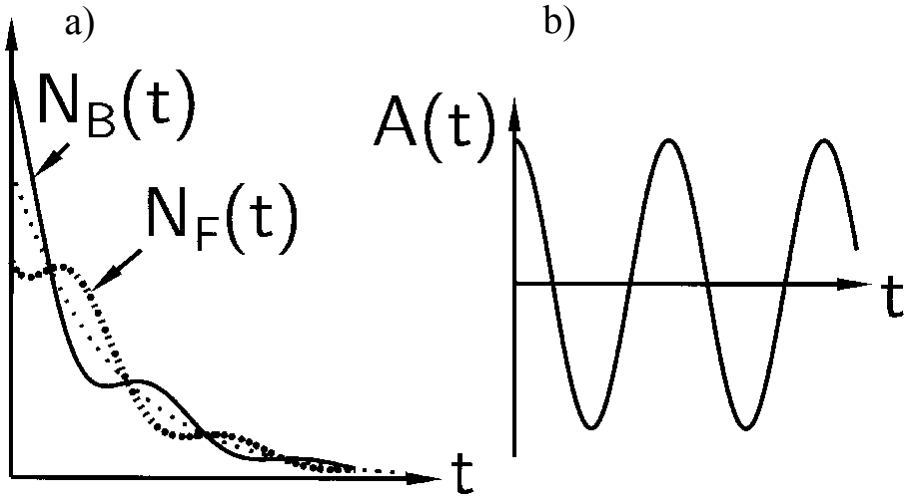

Figure 2.10: a) The time evolution of positron count in forward and backward detectors, b) Asymmetry of the signal calculated as in Eq. 2.16 [55].

Fig. 2.9. Depending on the number of precessions and the time of decay, the positron may be detected in either forward ($N_F(t)$) or backward ($N_B(t)$) detector (with respect to incoming muon direction $P(0)$) as shown in Fig. 2.10a. The evolution of muon spin polarization $P(t)$ as a function of time can be calculated as following:

$$\begin{aligned} A(t) &= \frac{N_F(t) - N_B(t)}{N_F(t) + N_B(t)} \\ P(t) &= \frac{A(t)}{A(0)} \end{aligned} \tag{2.16}$$

where, $A(t)$ is known as the asymmetry function and $A(0)$ is the maximum possible asymmetry for a given experimental configuration based on the initial spin polarization, efficiency of detectors and is generally ∼0.28. The schematic of an observed $P(t)$ is shown in Fig: 2.10b where one observes oscillations typical to magnetically ordered materials. The frequency of oscillations is related to the internal magnetic field B_{loc} by, $\omega_\mu = \gamma_\mu B_{loc}$. Here, γ_μ is the gyromagnetic ratio of muon given by $\gamma_\mu = \frac{ge}{2m_\mu}$.

2.3.3 Polarization function

Since muon is a local probe the magnetic field experienced by muon is written as B_{loc}. Apart from the single domain ferromagnetic crystals, the direction and/or magnitude of B_{loc} deviates from site to site around a mean $< B_{loc} >$. Accordingly, a generalized polarization function can be written as

$$P(t) = \frac{\int P_z(t) p(\mathbf{B}) d^3B}{\int p(\mathbf{B}) d^3B} \tag{2.17}$$

Here, $P_z(t)$ is the evolution of muon spin polarization after muon first enters the sample at t=0 with polarization in $z-$direction and $p(\mathbf{B})$ is the distribution function of the magnetic field in the sample. For magnetically ordered (ferromagnetic or antiferromagnetic) polycrystalline samples, there is a constant B_{loc} isotropically distributed in random direction so that,

$$P(t) = \left[\frac{1}{3} + \frac{2}{3}\cos(\gamma_\mu B_{loc} t)\right].$$

Here, $1/3^{rd}$ of the muon spin component is along B_{loc} and hence does not undergo precession. The remaining 2/3rd component of the spin precesses around B_{loc}.

If the material has any magnetic disorder giving rise to a small distribution around B_{loc}, the precessing part of the depolarization is accompanied by a damping factor λ_T. In addition, if the ordered spins have dynamic fluctuations, for example critical fluctuations around a phase transition, a relaxation is observed in the non-precessing part of the polarization with rate λ_L such that,

$$P(t) = \left[\frac{1}{3}e^{-\lambda_L t} + \frac{2}{3}e^{-\lambda_T t}\cos(\gamma_\mu B_{loc} t)\right]. \tag{2.18}$$

If the field distribution is too large, for example in highly disordered materials, the relaxation rates are too large and the oscillations are completely damped.

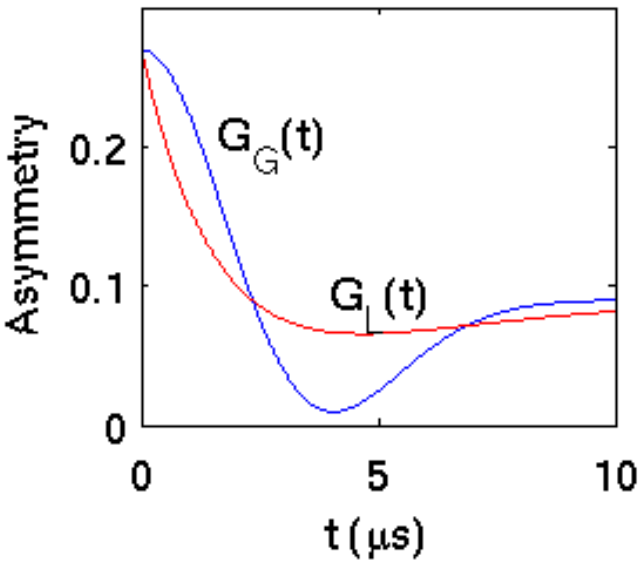

Figure 2.11: A schematic μSR asymmetry function for a paramagnet showing Kubo-Tayabe function [56].

In case of materials with randomly oriented static spins, for example in paramagnets, muons see the field created by randomly oriented nuclear moments which are static in the time scale of muon life time. Random orientation of these nuclear moments can be projected as either a Gaussian or Lorenz distribution of the fields depending on the dense or dilute arrangement of the moments. When this distribution is substituted into Eq. 2.17, the evolution of polarization takes the form a so-called Kubo-Tayabe function given by:

$$P(t)_{G-KT} = \frac{1}{3} + \frac{2}{3}(1-\sigma^2t^2)e^{-\sigma^2t^2/2} \quad \text{..... for Gaussian distribution}$$

where σ is the width of the Gaussian distribution and,

$$P(t)_{L-KT} = \frac{1}{3} + \frac{2}{3}(1-at)e^{-at} \quad \text{..... for Lorentzian distribution}$$

with a/γ_μ being half-width half maximum of Lorentzian distribution. The two functional forms are depicted in Fig. 2.11.

2.3.4 Instrumentation

Fig. 2.12 depicts a simple schematic of μ^+SR experimental set up. The muon beam arrives at the sample with its spin polarized antiparallel to its momentum. Depending on the sample magnetic properties the muon precesses and/or relaxes in the sample before decaying into a positron. The positron is then detected by the scintillating detectors placed in the front and back of the sample.

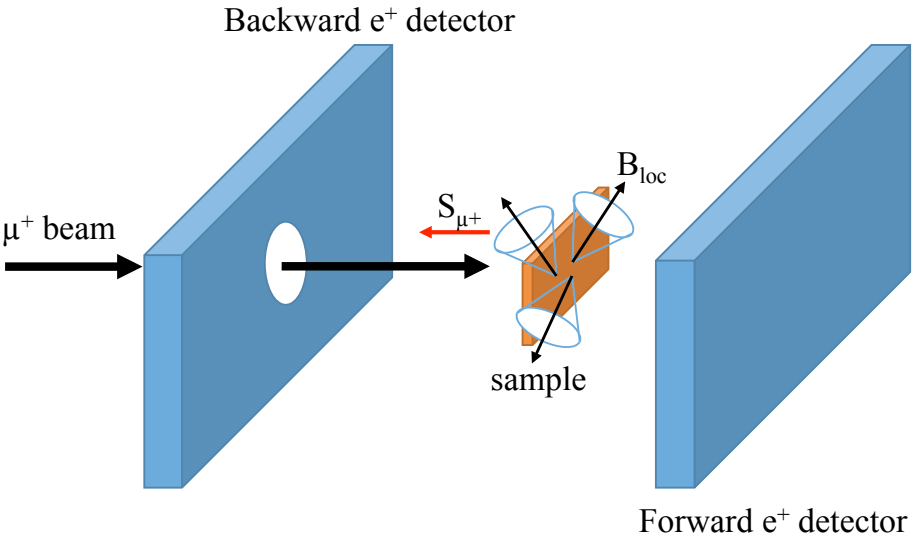

Figure 2.12: Sketch of the μ^+SR spectrometer.

Chapter 3

Coexistence of Antiferromagnetism and Spin glass states (AFSG)

$PbFe_{1/2}Nb_{1/2}O_3$

This chapter considers B-site disordered $PbFe_{1/2}Nb_{1/2}O_3$ as a model material to search for the coexistence of long-range magnetic order and spin glass state. PFN is known to be an antiferromagnet exhibiting spin glass properties at low temperatures. Earlier neutron scattering data have suggested that the antiferromagnetic Bragg peak survives into the spin glass state indicating that $PbFe_{1/2}Nb_{1/2}O_3$ is a potential candidate to look for the coexistence of antiferromagnetism and spin glass. Therefore, the present work considers a combination of neutron scattering and Mössbauer spectroscopy to probe the AFSG coexistence on a microscopic level.

3.1 Structural and magnetic properties

$PbFe_{1/2}Nb_{1/2}O_3$ has the perovskite crystal structure shown in the schematic Fig: 1.13. In the lattice, Pb^{2+} and O^{2-} ions occupy corner and face center positions of the unit cell, respectively. The magnetic Fe^{3+} and non-magnetic Nb^{5+} share the body center of the unit cell and are randomly distributed over the whole sample. The ratio of magnetic to non-magnetic ions is restricted by the requirement of charge neutrality.

At high temperatures, PFN has the *Pm3m* space group cubic symmetry with lattice parameter $a = 4.01$ $\mathring{A}$ [57]. According to this space group the Pb ions occupy $(0,0,0)$ positions, the oxygen ions occupy $(\frac{1}{2},\frac{1}{2},0)$-type positions and Fe^{3+}/Nb^{5+} are distributed over the $(\frac{1}{2},\frac{1}{2},\frac{1}{2})$ positions. As in many Pb-based complex perovskites, the Pb^{2+} ions are shifted from their $(0,0,0)$ positions at rather high temperatures. These shifts, however, are only weakly correlated so that the space group is still *Pm3m* on average [58].

At low temperatures, PFN undergoes a ferroelectric transition accompanied by a structural transition from a *Pm3m* (cubic) to *P4mm* (tetragonal) crystal structure at $T_m = 375$ K. For T$<$ 355 K, there is an additional transition into a *Cm* monoclinic structure, which is retained down to base temperature [58]. However, the monoclinic deviations of the lattice parameter do not exceed 5×10^{-4} from the cubic structure and

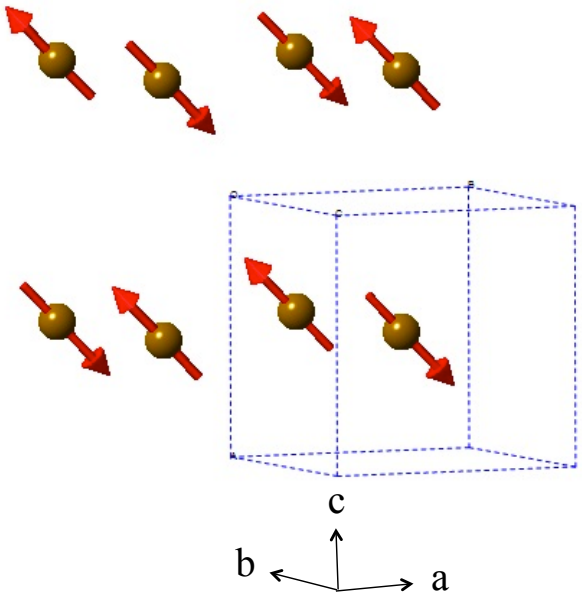

Figure 3.1: Magnetic unit cell of the G-type AF $PbFe_{1/2}Nb_{1/2}O_3$.

the monoclinic angle is only 0.12° away from 90°. So far there has been no evidence of chemical ordering of the Fe^{3+}/Nb^{5+} ions.

PFN is an antiferromagnet below T_N ~143 K. The Fe^{3+} moments are arranged in a simple *G*-type structure [59] as shown in Fig. 3.1. The spin glass state emerges at the temperature $T_{SG} \sim 12$ K. It is manifested by a difference between the magnetization curves measured under zero-field-cooled (ZFC) and field-cooled conditions [60]. From a combined muon-spin rotation (μ^+SR) and neutron scattering study, it is known that the long-range AF order in PFN is not destroyed by the appearance of the SG state [61]. Neutron scattering also revealed the presence of magnetic short-range order by means of diffuse scattering, which greatly increases below ~50 K. Based on the magnetoelectric (ME) experiments, the coexistence of AF and SG orders below T_{SG} is credited by Kleemann et al., to phase separation [62] in the sample arising from the disorder at the magnetic site. In their model, two types of magnetic order emerge independently on separate subsystems: an infinite-range percolation cluster (AF) and isolated Fe^{3+} ions and unblocked superantiferromagnetic Fe^{3+} clusters (SG). However, these results are inconclusive regarding the nature of coexistence due to the lack of microscopic information about the magnetic system.

3.2 Samples and Methods

Experimental proof of a true AFSG state can be obtained only by a combination of both momentum-selective and local-probe techniques. Momentum-resolved techniques probe microscopic quantities averaged over the entire sample, whereas local-probe resonant methods are ideal tools for validating homogeneity on the microscopic scale. Therefore, neutron scattering and Mössbauer spectroscopy data were collected on PFN samples. Further, the dependence of the properties of PFN on metallurgy requires the study of both ceramic and single crystal samples.

Ceramic samples of PFN were synthesized by mixing $FeNbO_4$ with PbO and sintering at 1050° C for one hour leading to perovskite $PbFe_{1/2}Nb_{1/2}O_3$. These powder samples are used as starting materials for the synthesis of single crystals via spontaneous crystallization. In this process a mixture of polycrystalline $PbFe_{1/2}Nb_{1/2}O_3$ and $PbO\text{-}B_2O_3$ solvent is sealed in a platinum crucible. This crucible is sintered at 1200° C for 5 hours resulting in crystals of PFN about 4x4x4 mm^3 [1].

Bulk magnetization measurements of PFN were performed on a physical property measurement system (PPMS) using a vibrating sample magnetometer (VSM) and an AC magnetometer (ACMS). Neutron scattering experiments were performed at the 3-axis spectrometer TASP using a wave vector 2.662 $Å^{-1}$. From the neutron guide to the detector the horizontal collimation was $25' - 80' - 80' - 80'$. With that configuration, the elastic (vanadium) resolution is 1.3 meV (FWHM). A 5 cm thick PG filter was used to eliminate higher-order neutrons. The sample was loaded to a standard "orange" cryostat to track the evolution of the magnetic Bragg peak. Conventional ^{57}Fe Mössbauer absorption spectroscopy experiments in transmission geometry were performed on 60 mg/cm^2 samples. All Mössbauer data were collected on powder samples prepared by grinding either single crystals or ceramic material.

3.3 Results

3.3.1 Bulk magnetization

In the single crystal PFN samples, two phase transitions are readily observed in macroscopic experiments. Fig. 3.2 shows magnetic *dc* susceptibility versus temperature obtained using ZFC (sample is first cooled in zero field to base temperature and measurements are performed while warming after an external bias field is applied) and FC (sample is first cooled to base temperature in the presence of a bias field and measurements are performed while warming with the field still on) protocols. The hump at T_N ∼144 K in both ZFC and FC curves reflect the transition from paramagnet to antiferromagnetic phase. Below $T_{SG} \sim 12$ K the two curves diverge, a typical feature observed in spin glasses. SG behavior is further evidenced by the gradual frequency dependence of the rounded peak in *ac* susceptibility. Fig. 3.3 shows the real part of magnetic *ac* susceptibility of PFN taken at selected frequencies where T_{SG} shifts to higher temperatures with increasing frequency. Unlike the anomaly around T_{SG}, the cusp at T_N does not shift as a function of frequency. Additionally, this cusp at T_N also does not show any noticeable history effects. These observations are in agreement with previous reports [60,62,63], confirming that our samples behave essentially identical to those used by other groups. The χ_{ac} taken at 100 Hz and χ_{dc} are close to each other but do not coincide. The reason is that at the necessarily low probing magnetic fields the accuracy of the magnet of PPMS is limited due to remanence.

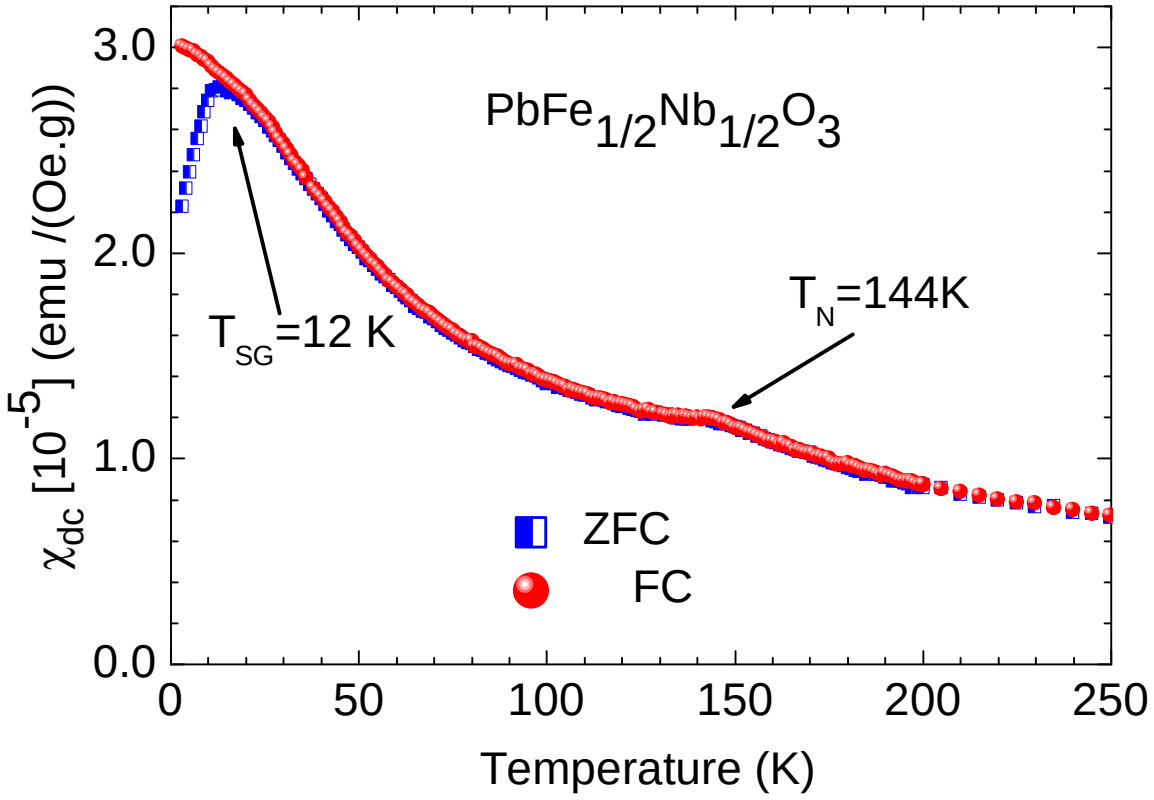

Figure 3.2: The *dc* susceptibility of PFN measured in 100 Oe external field following ZFC and FC protocols.

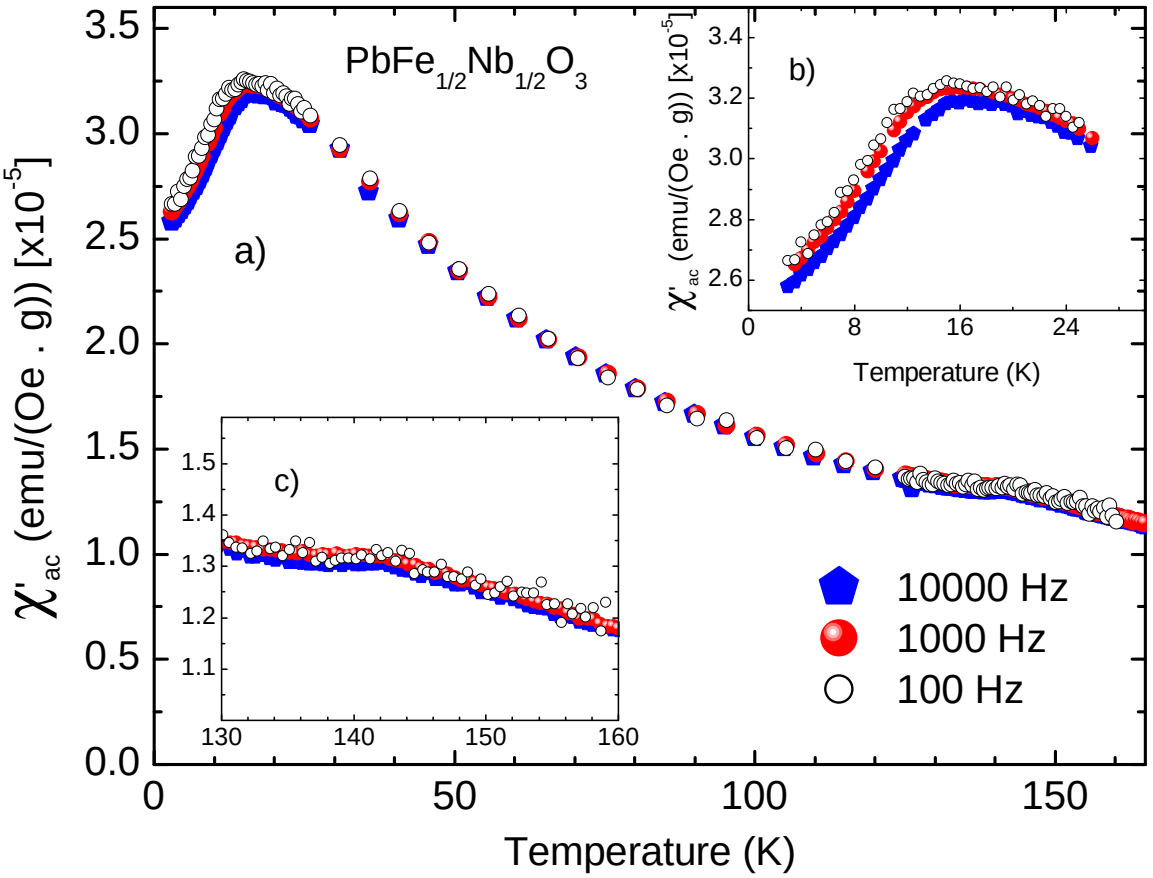

Figure 3.3: a) Real part of the magnetic *ac* susceptibility of PFN measured at selected frequencies. Panels (b)&(c) magnify the data in the vicinity of T_{SG} and T_N, respectively.

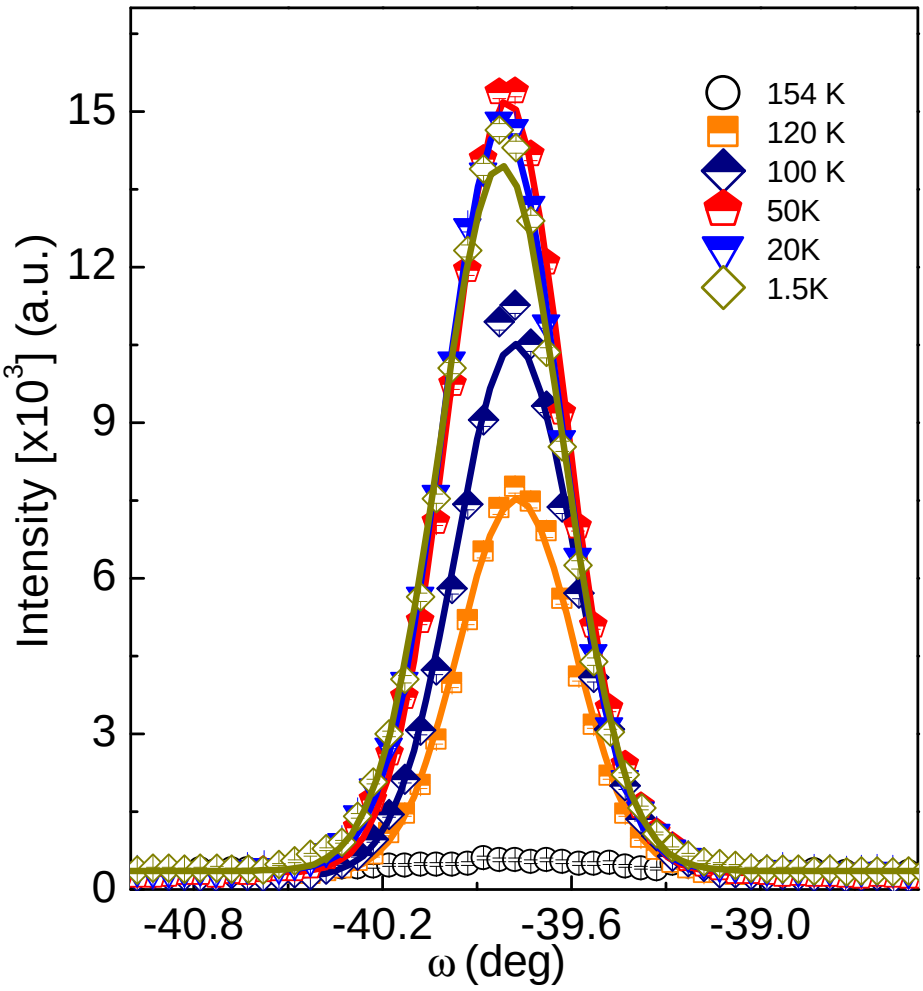

Figure 3.4: AF Bragg peak of PFN at $\mathbf{Q} = (1/2,\ 1/2,\ 1/2)$ at various temperatures indicating an AF order.

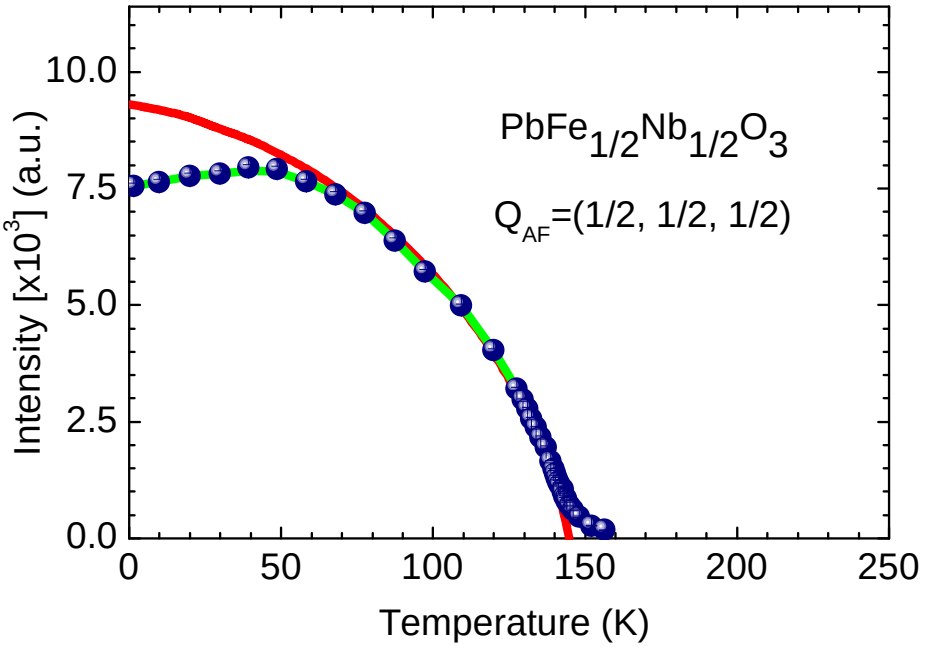

Figure 3.5: Temperature evolution of the AF Bragg peak intensity of PFN at $\mathbf{Q} = (1/2,\ 1/2,\ 1/2)$. The solid lines are guides to the eye where red line indicates the approximate intensity for a collinear antiferromagnet.

3.3.2 Neutron Scattering

Neutron scattering was performed to track the evolution of the long-range antiferromagnetic order in PFN . Below T_N, this AF order results in the emergence of new Bragg peaks in neutron diffraction. In PFN , the magnetic Bragg peak at (1/2, 1/2, 1/2) was followed with the help of rocking scans. Fig. 3.4 shows some of these rocking curves through the (1/2, 1/2, 1/2) AF Bragg peak at selected temperatures. The Bragg peak gradually grows on cooling, however, a slight reduction of intensity is observed for T<50 K. In these scans the magnetic diffuse scattering, as seen in [61] appears in the form of flat background as its angular width in ω is around 20°, Ref. [61], which is $\sim$ 30 times larger than the width of the Gaussian Bragg peak. In PFN the AF Bragg peak is (typically) two orders of magnitude more intense than the magnetic diffuse scattering, thus this background is weak and its temperature dependence has no effect on the results presented here.

Integrated intensity of the Bragg peak can be quantified by fitting the rocking curves with Gaussian functions. The measured temperature dependence of the $\mathbf{Q} = (1/2,\ 1/2,\ 1/2)$ Bragg intensity is plotted in Fig. 3.5. As expected for an AF, the intensity of the magnetic Bragg peak (*i.e.* square of magnetization) increases smoothly below T_N. However, the non-vanishing intensity from critical fluctuations in the region of T_N does not allow a reliable extraction of critical exponent of the transition. Therefore, the solid line in Fig. 3.5 represents only a guide to the eye. Below $\sim$ 50 K, a small decrease of the AF Bragg peak intensity is observed, while retaining the Gaussian line-

[1]All the samples were prepared by the group of Prof. Sergey Lushnikov at the Ioffe Physico-Technical Institute, Russia

shape. This observation is reminiscent of that seen in certain reentrant systems [39,64], and may be attributed to spin-canting.

3.3.3 Mössbauer Spectroscopy

Verifying the coexistence of the SG and AF phases at the microscopic level requires the use of microscopic local probes. For this purpose Mössbauer spectroscopy employs magnetic nuclei already present in the material, which in the case of PFN are ^{57}Fe. In paramagnetic state, the position of the nuclear absorption line is shifted relative to the source and this is known as isomer (or chemical) shift. As described in Sec. 2.2, this is related to the valence state of the Mössbauer ion. Absorption spectrum of PFN in paramagnetic state (T = 200 K), shown in Fig. 3.6a, exhibits doublet structure. This additional feature is due to the quadrupolar splitting arising from a non-spherical charge distribution around the ^{57}Fe ion resulting in an electric field gradient at the nuclear site. In this case, isomer shift defines the shift of center of the doublet with respect to source which in Fig. 3.6a is ∼0.4 mm/s. This value lies within the 0.3-0.6 mm/s interval corresponding to the trivalent state of iron ion and the quadrupolar splitting may be attributed to the small monoclinic distortion of cubic lattice.

In the long-range ordered AF phase, the degeneracy of the nuclear energy levels is further lifted by the local hyperfine field at the nuclei, generated by the static sublattice magnetization. The resulting energy intervals between the lines are then a measure of the iron magnetic moment. Fig. 3.6b-d show the spectra of PFN in AF phase. Two important observations can be made from these spectra.
1) The Zeeman splitting gradually increases as the temperature is lowered, in accordance with increasing Fe moment in the AF phase. This is clearly seen in Fig. 3.7 where temperature dependence of the measured average hyperfine field $\langle B_{hf} \rangle$ is presented. In the AF phase, it follows the magnetic order parameter, as expected.
2) Absence of doublet structure from paramagnetic phase at all the temperatures $<T_N$. If one were to consider the phase separation model for the coexistence of antiferromagnetic order and spin glass, the presence of a doublet, like the one above T_N is expected to be in the spectra at $T_{SG} < T < T_N$. This immediately rules out the possibility of PM clusters in magnetically ordered AF phase and proves that all the Fe^{3+} ions are involved in the AF structure.

Similar spectra obtained on ceramic powders reflect identical results to that of powdered single crystal. This consistency proves that all effects described below are robust and sample-independent.

For an extensive analysis of the spectra, following fit strategy is used to extract relevant parameters like temperature dependent B_{hf}.

In the paramagnetic phase, a reliable fit of the spectrum is obtained by considering two types of Fe^{3+} ions which share a similar isomer shift but have distinct values of quadrupole splitting. Attempts to fit the paramagnetic spectra with a single contribution gave less satisfactory agreement factors and a significant broadening. The two effects become progressively more pronounced in the AF phase, suggesting that the one-component model is inappropriate. As discussed elsewhere [65], the two different sites may correspond to local variations in chemical short range order. In our analysis, the two contributions are distributed in 50:50 ratio and are represented by green and

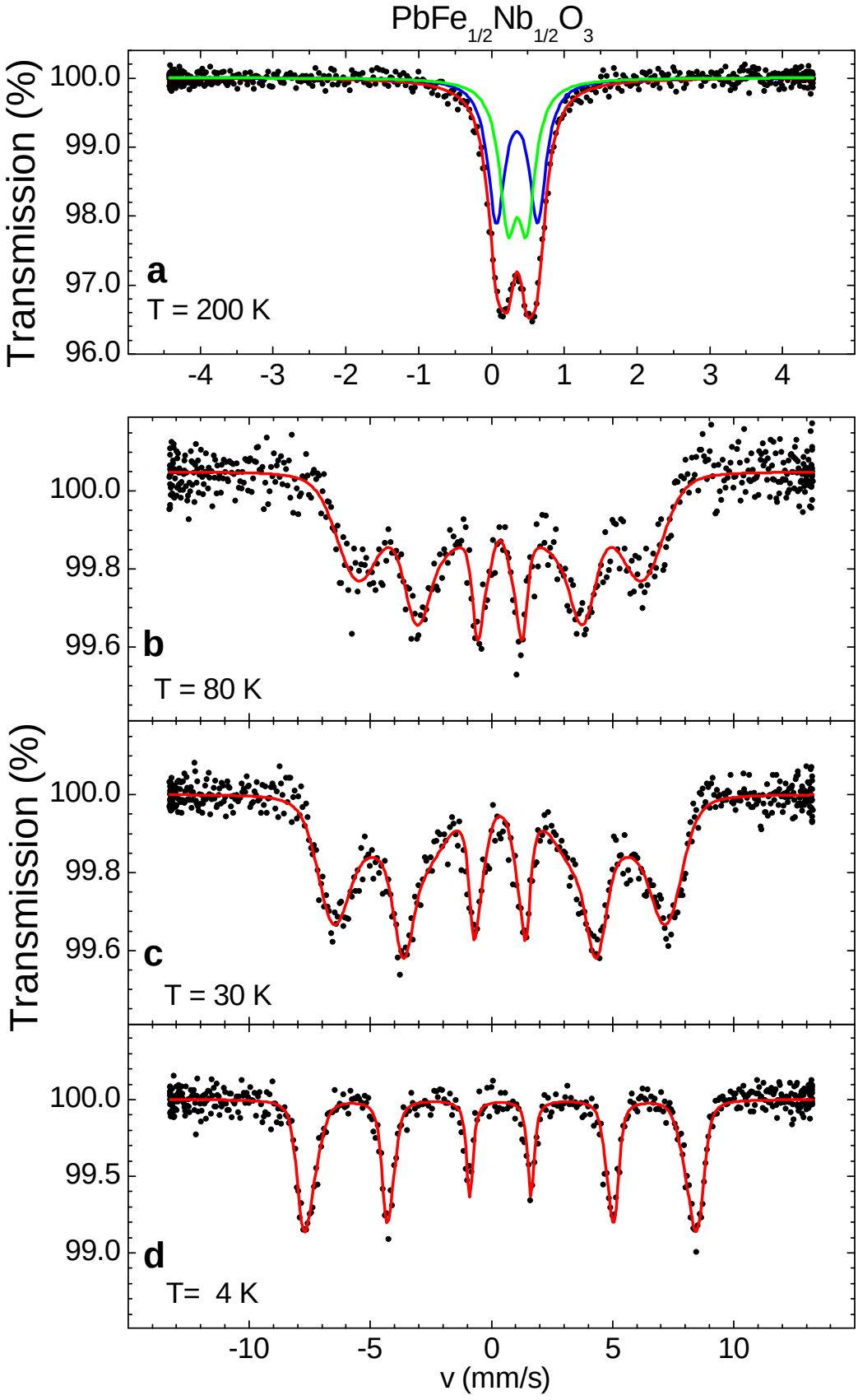

Figure 3.6: Representative Mössbauer spectra of PFN taken in the paramagnetic phase (a) and below its Néel temperature (b-d). Note a reduced velocity scale in panel (a).

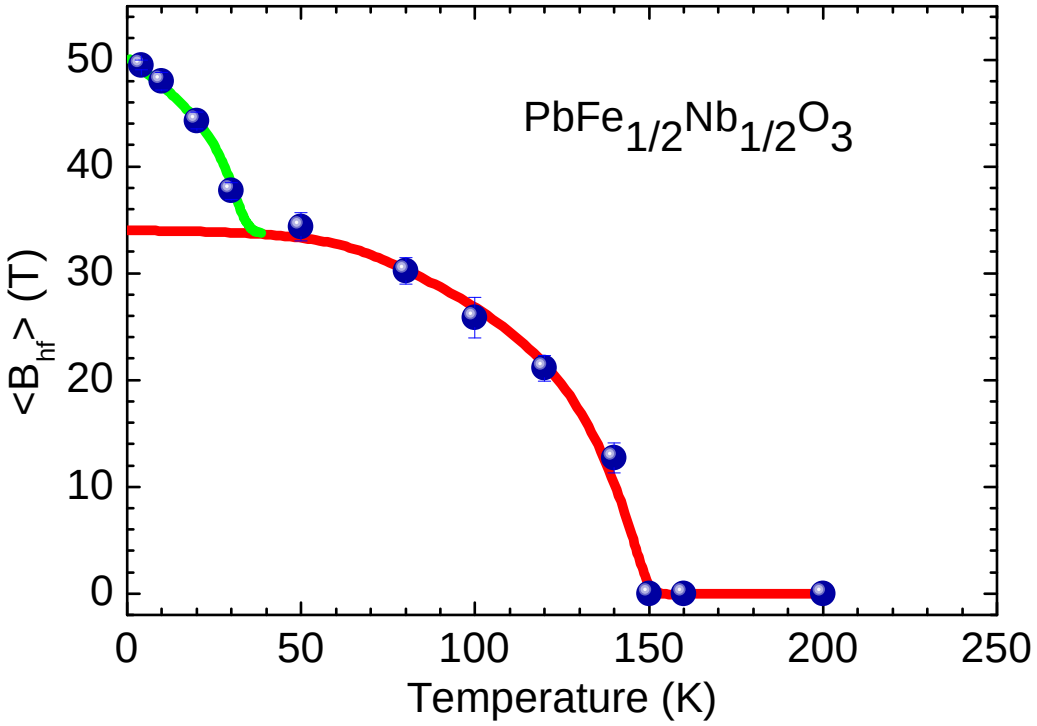

Figure 3.7: Evolution of mean hyperfine field at Fe site. The solid lines are only guide to the eye.

blue lines in Fig. 3.6a whereas red line indicates the total fit.

In antiferromagnetic phase, the six symmetric absorption lines indicate that the contribution of quadrupolar splitting is nearly zero (unlike in Fig. 2.7). This can be explained on the basis of a random relative orientation of EFG tensor and B_{hf} at every site. However, consistent fits of the spectra at all temperatures below T_N yield two contributions to the hyperfine field with relative areas 50:50. Furthermore, to obtain a good fit, one has to allow for an intrinsic and temperature-dependent broadening of the absorption lines, which implies a distribution of magnetic hyperfine fields in the sample. These hyperfine fields are assumed to have Gaussian distribution as in Fig. 3.8.

Temperature evolution of the hyperfine field distribution $P(B_{hf})$ changes from a pronounced double-peak shape just below T_N to a nearly perfect single peaked function with a slight shoulder below $\sim$ 10 K . This behavior is exactly opposite to the expectations for a phase separated cluster-like scenario where the two Gaussians are clearly distinguishable in the whole temperature range [46].

Variation of the maximum in $P(B_{hf})$ reflects the increase of the sublattice magnetization towards base temperature, as plotted in Fig. 3.9a for the two hyperfine field contributions. In both the samples, the hyperfine field reaches a mean value of $\sim$50 T at the base temperature (see Fig. 3.7). This value is very close to the saturation hyperfine field observed in many other Fe^{3+}-based perovskites [66], suggesting a full recovery of the Fe^{3+} moment at the lowest temperature.

Another experimental result that firmly supports a microscopic coexistence of AF and SG orders is the measured temperature dependence of the width σB_{hf} of the hyperfine field distribution (Fig. 3.9b). For both sites, σB_{hf} gradually increases on

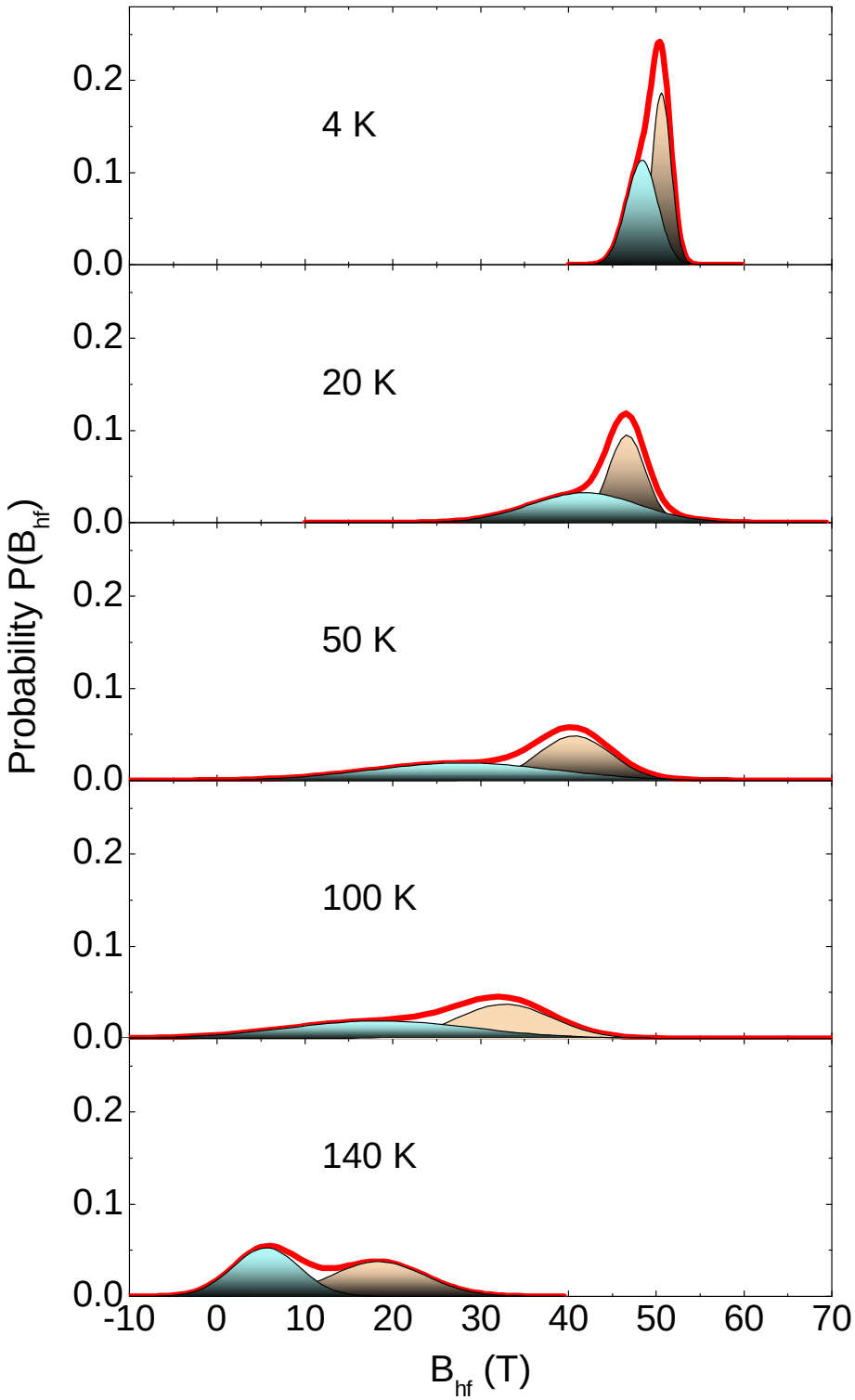

Figure 3.8: Temperature evolution of the P(B_{hf}) of PFN. The two Gaussian components are shown by shaded areas and the resultant distribution is reprsented by thick red line.

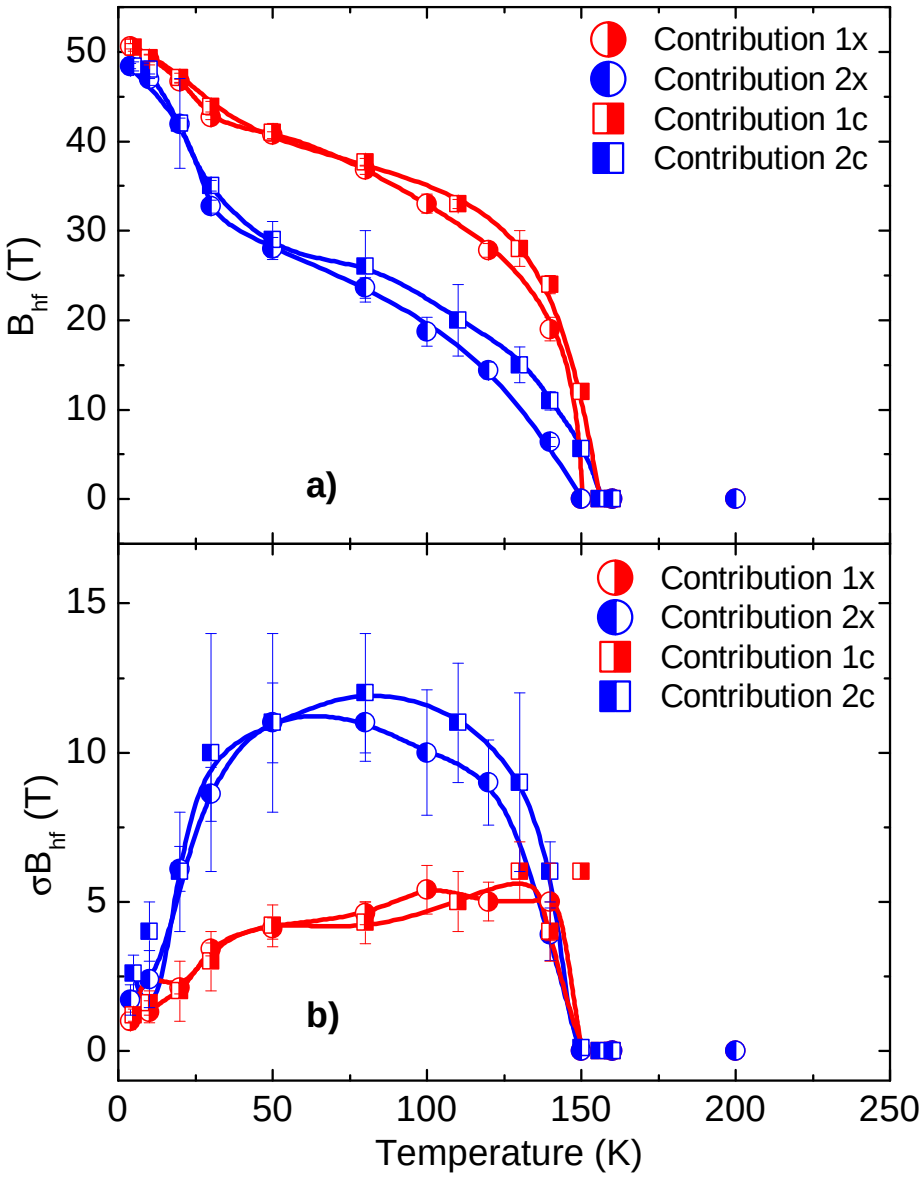

Figure 3.9: a) Mean and b) widths of the magnetic hyperfine fields for the two Fe^{3+} sites (1,2) as deduced from the measured Mössabuer spectra, as described in the text. Labels "x" and "c" stand for crystalline and ceramic samples, respectively.

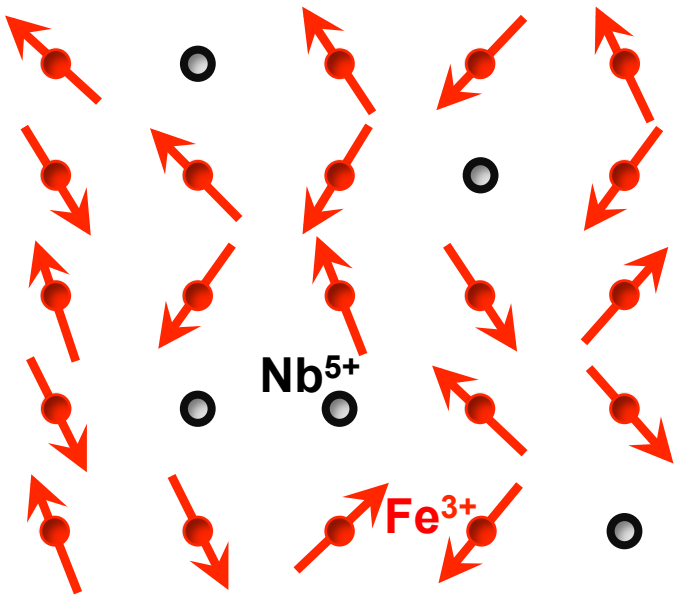

Figure 3.10: Antiferromagnetic G-type order of the Fe^{3+} moments in the proposed model for the speromagnetic-like ordering in the antiferromagnetic spin glass phase. The tilt angle randomly varies from site to site averaging to zero while the longitudinal components gives a mean AF structure.

cooling below T_N in the AF phase and reaches a broad maximum between 120 K and 50 K. Below $T \sim 50$ K, the distribution width decreases drastically, and remains constant at a very small value below T_{SG} ~12K. The most natural interpretation of such behavior is that line broadening is due to slow fluctuations of local magnetic fields within Mössbauer frequency window (MHz to GHz) which freeze at base temperature. In this scenario, all of the available Fe spins are involved in creating the AF order, and the simultaneous narrowing of all lines at low temperatures corresponds to all of them being involved in SG freezing. Such behavior is totally inconsistent with the above-mentioned inhomogeneous model [62] because, a partition into smaller dynamic clusters and infinitely connected static AF cluster would result in narrower lines in the high temperature AF phase.

3.4 Microscopic model

The results of AF order parameter from neutron scattering and the homogeneous magnetic hyperfine field sensed by Mössbauer nuclei allow us to propose a model for the low-temperature magnetic structure of PFN . As mentioned, the variation of B_{hf} above 50 K (Fig. 3.7) roughly follows that of the AF long range order parameter determined by neutron diffraction (Fig. 3.5). It stands to reason that in this regime it mainly reflects the evolution of the collinear long range ordered AF component $\langle S^z(T) \rangle$ of Fe^{3+}. The increase of mean magnetic hyperfine fields on cooling below 50 K (Fig. 3.7, green

line), is reminiscent of precursor phenomena in ferromagnetic re-entrant spin-glass systems like AuFe [36, 67] or the mixed spinel $Mg_{1+t}Fe_{2-2t}Ti_tO_4$ [68]. It represents a gradual freezing of transverse spin components within Mössbauer frequency window. In other words, there occurs a tilting of the ionic moments from the z direction set by the AF long-range order (Fig. 3.10, red arrows). The process culminates in a complete (static) freezing at T_{SG}. From the change of B_{hf} observed between 50 K and 4 K, we can roughly estimate the typical tilt angles to be $\sim 30^o$ and $\sim 55^o$.

Unlike the longitudinal component, the transverse component does not show long-range correlations. At the time-scale of $\sim 10^{-11}$ s it contributes to the static diffuse neutron magnetic scattering with a correlation length ~ 15 Å [61], but adds nothing to the AF Bragg peak intensity. In our proposed model, the progressively more pronounced transverse correlations cause a canting of spins below T$\sim$50 K, and become liable for the reduction of the latter (Fig. 3.5, green line).

To get a complete picture of the proposed microscopic model, knowledge of the relevant exchange interactions is necessary. These exchange interactions, together with their radii, constitute essential parameters for an appropriate theory aimed to reproduce the phase diagram of a disordered AF. Therefore, we have attempted to measure spin waves in $PbFe_{1/2}Nb_{1/2}O_3$ using inelastic neutron scattering from which exchange interactions can be extracted by fitting the dispersion to an appropriate spin Hamiltonian. However, the measured spectra along $< 001 >$, $< 110 >$ and $< 111 >$ directions from AF Bragg peak do not reveal a clear dispersion even up to an energy transfer of 12 meV. Therefore, quantitative information of the magnetic interactions of PFN cannot be obtained.

For further details of the inelastic magnetic scattering from PFN , please refer to the Appendix. A.1.

3.5 Phase diagram

As the attempt to obtain strengths of magnetic interactions was not successful, the essential ingredients to calculate magnetic phase diagram of disordered antiferromagnets, and hence of the coexisting AFSG phase remain missing. Therefore, an indirect attempt is made in this regard by probing the change in T_{SG} as a function of external stimuli like external field and hydrostatic pressure. The AFSG phase in PFN can be described as a result of competition between spin glass and antiferromagnetic orders. While the Fe moments are connected through Fe-O-Fe exchange path to form AF order, it is believed that the next nearest neighbors are frustrated contributing to SG. Also, the correlation length ($\sim$ 4×lattice parameter) associated with the magnetic diffuse neutron scattering observed by [61] had revealed that the exchange interactions extend at least up to next-nearest neighbors. It is possible to modify these interactions by applying an external magnetic field and pressure. The measured phase diagram can then be compared with one of the existing models which predicted a coexistence of LRO and spin glass.

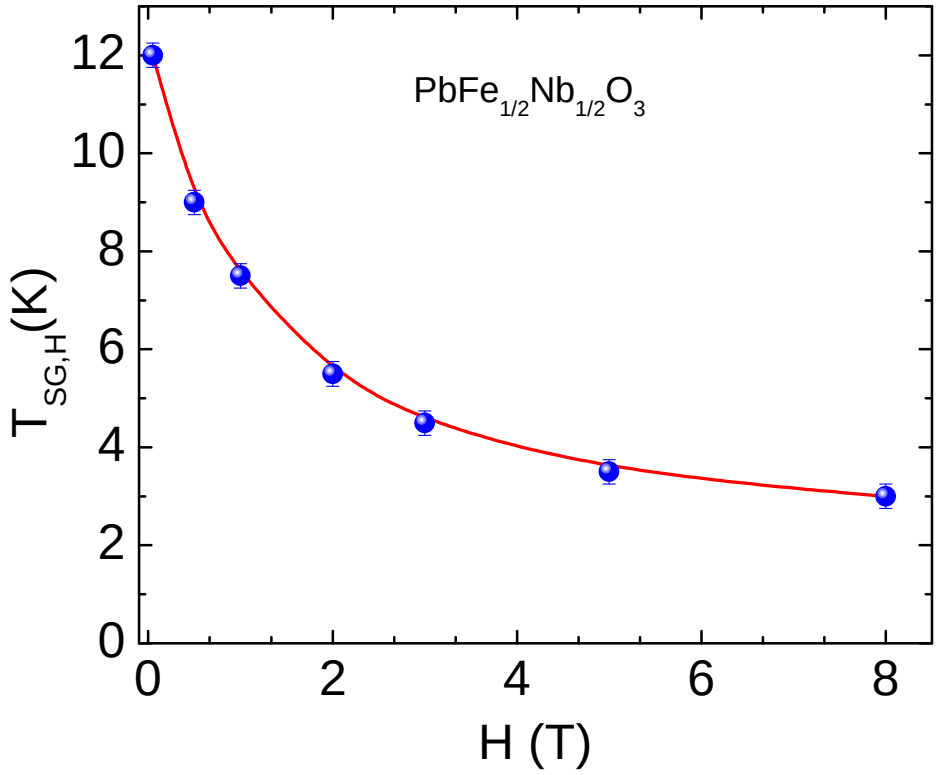

Figure 3.11: Phase diagram of T_{SG} as a function of external applied magnetic field in PFN. The red line a guide to the eye.

3.5.1 Field dependence

The field dependence of spin glass transition is obtained by measuring FC-ZFC curves which were repeated in dc bias fields of 0.01 T-8 T. T_{SG} is determined by the maximum of ZFC susceptibility. Fig. 3.11 shows that T_{SG} gradually decreases as the applied field increases indicating a conventional behavior observed in spin glasses [37, 69].

Mean field theory based on the infinite range model predicts that the transition temperature below which LRO and SG coexist follows Gabay-Toulouse line in Heisenberg systems as a function of applied magnetic field. According to Gabay-Toulouse line, only the transverse components of the spins freeze below T_{SG} and the long-range magnetic order is sustained by the longitudinal components. In the presence of external magnetic field, the transition temperature varies as:

$$T_{SG}(H) \propto T_{SG}(0)\left[1-(\frac{H}{A})^2\right]$$

Although, the microscopic model for AFSG in PFN suggests transverse spin freezing below T_{SG}, we can clearly see that this characteristic temperature does not fall of with an H^2 dependence. Therefore, we can conclude that although the glass transition temperature of PFN decreases with increasing field, it does not follow the functional form given by MFT.

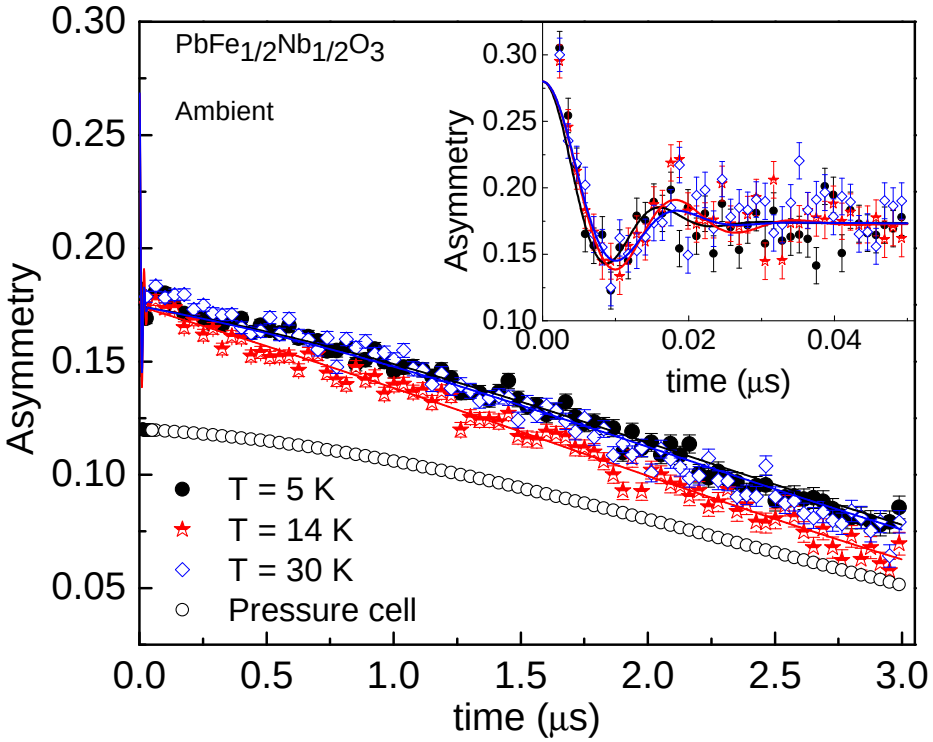

Figure 3.12: μ^+SR spectra of PFN taken in ambient conditions around the T_{SG} transition.

3.5.2 Pressure dependence

Application of pressure allows us to retain the disorder at Fe^{3+}/Nb^{5+} while affecting the exchange interactions. This helps us to understand if disorder plays a major role for AFSG phase.

Since the effect of pressure on the magnetic transitions of PFN is unknown, μ^+SR spectroscopy appears as an ideal probe due to its high sensitivity to the spin glass transition in the sample. The measurements are performed on powder sample of PFN at DOLLY and GPD stations in ambient and several hydrostatic pressures respectively. The resulting spectra at ambient pressure close to T_{SG} are shown in Fig. 3.12. In all the measured spectra, the initial muon depolarization falls to its $2/3^{rd}$ value with oscillations (inset of Fig. 3.12) indicating the precession of the muon spin due to a static local field as discussed in Sec. 2.3. This observation is complementary to the sextet seen in Mössbauer spectra and the magnetic Bragg peak seen in neutron diffraction related to the AF long-range order in the sample. However, the oscillations decay very rapidly within 0.05 μs exhibiting only one clear wiggle. This strong relaxation indicates the distribution of local internal field. After 0.05 μs, the depolarization continues to decay until $1/3^{rd}$ of the initial asymmetry is retained. This is typical for a polycrystalline magnetic system with static long-range order, as $1/3^{rd}$ of the muon spin component points in the direction of local internal field. Therefore, this fraction of the muon beam does not undergo Larmor precession. However, the signal relaxes due to dynamic fluctuations of the spins.

To accommodate these two observations, the μSR spectra are consistently fitted

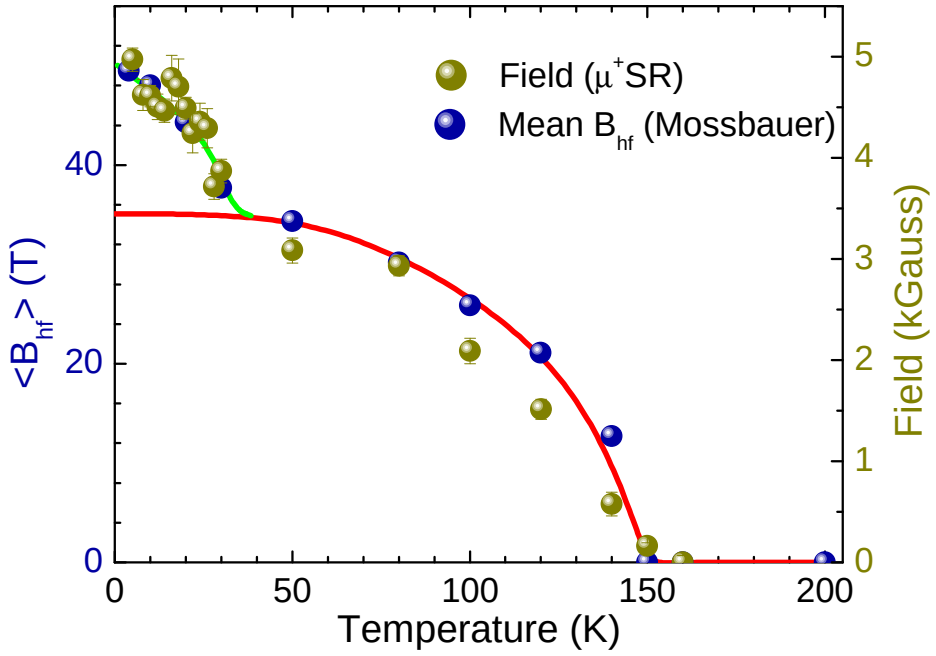

Figure 3.13: The comparison of temperature dependence of internal field seen by μSR spectra in PFN from the fits of ZF spectra with Eq. 3.1 and hyperfine field seen by Mössbauer spectroscopy.

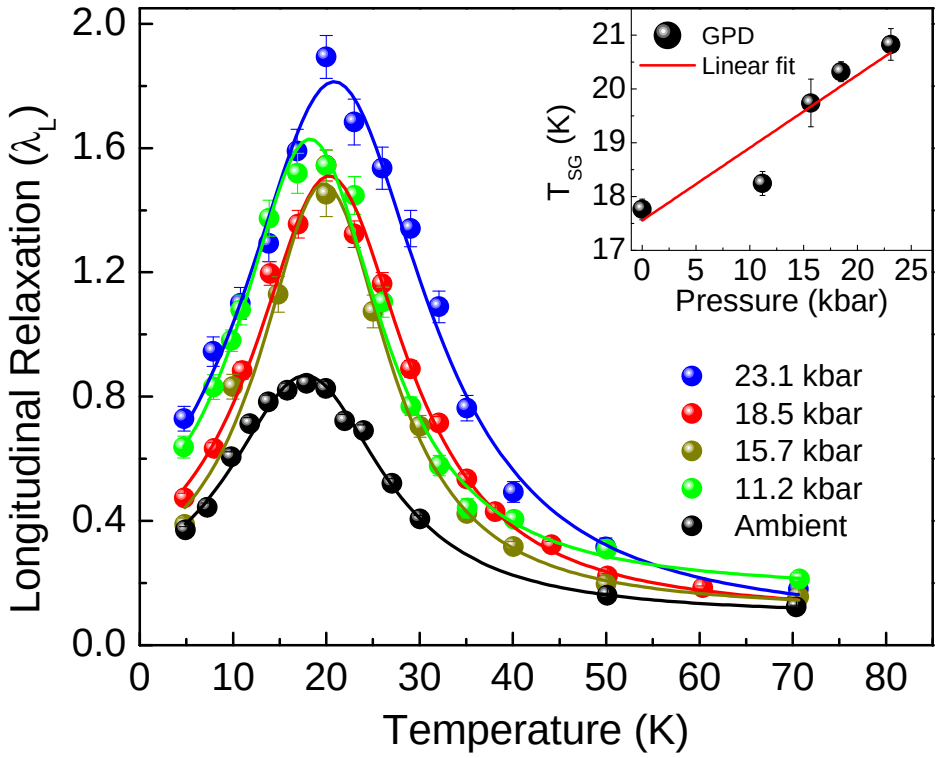

Figure 3.14: Longitudinal relaxation rate of the μ^+SR signal, as fitted by Eq. 3.1, of PFN at various applied pressures around the T_{SG} transition.

with the following empirical function in order to extract the temperature dependencies of local field, relaxation rates of precessing and non-precessing parts of the muon decay:

$$A(t) = A_{sample}[\frac{2}{3}e^{-\frac{1}{2}(\sigma_T t)^2} j_0(\gamma_\mu B_{max} t) + \frac{1}{3}e^{(-\lambda_L t)}] + A_{bkg}e^{(-\lambda_{bkg} t)} \tag{3.1}$$

where A_{sample}, A_{bkg} are contributions from sample, background respectively. When the sample was put in a pressure cell, the background contribution is correspondingly adjusted by writing

$$A_{bkg}e^{(-\lambda_{bkg} t)} = A_{pc}e^{(-\lambda_{pc} t)}[\frac{1}{3} + \frac{2}{3}(1 - \sigma^2 t^2)e^{(} - \frac{1}{2}\sigma^2 t^2)].$$

The contribution of pressure cell to the total asymmetry was measured by calibrating the total signal for every applied pressure. Since the spectra show only half an oscillation and there is no knowledge of the number of muon sites in the material, the internal field in PFN is approximated by the zeroth-order Bessel-function $j_0(\gamma_\mu B_{max} t)$ where B_{max} is the maximum field in the double comb shaped field distribution centered at zero.

At ambient pressure, B_{max} gradually increases below T_N as the temperature is lowered (see Fig. 3.13) with a rapid change below ∼50 K. This is consistent with the change in Mössbauer hyperfine field below ∼50 K (plotted in Fig. 3.13) confirming the local behavior of the ordered Fe moments. We observe that λ_L, indicative of dynamics in the system peaks up at ∼17.5 K in ambient conditions similar to the observation made in Fe-Zr alloys when a spin glass transition occurs at T_{SG} [70]. Upon increasing the hydrostatic pressure, this peak shifts to higher temperatures. To obtain a systematic temperature dependence of this shift, λ_L is fitted with a Lorentzian function for all the applied pressures. Fig. 3.14 shows the maximum of peak in λ_L referring to a linear increment of T_{SG} with pressure as shown in the inset of Fig. 3.14. This is in contradiction to the decrease of T_{SG} in the presence of external magnetic field (see Fig. 3.11). The reason is that unlike external field the hydrostatic pressure effects only the lattice parameters directly modifying the magnetic exchange interactions.

3.6 Summary

The results of neutron scattering confirm that the long-range AF order persists into the SG state. In addition, these results show that the intensity of the AF Bragg peak reduces below ∼50 K, pointing to the canting of spins ordered in a collinear AF structure. On a microscopic scale, this is reflected in the rapid increment of local hyperfine field felt by the ^{57}Fe nuclei which ultimately reaches a saturation moment at the base temperature. Therefore, all these results point to the fact that the long-range AF and short-range SG coexist in the system. A speromagnet-like model is proposed to understand spin-arrangement of the system which considers: randomly tilted frozen transverse components giving rise to SG and a mean AF on longitudinal components. Further, the transition temperature T_{SG} into AFSG state is studied by the application of an external magnetic field and hydrostatic pressure.

Chapter 4

Effect of non-magnetic ion on AFSG

$PbFe_{1/2}Ta_{1/2}O_3$

An extensive study of influence of the non-magnetic ions at the disordered site on the phase diagram of PFN allows a better understanding of the AFSG ground state. Hence, a fully substituted stoichiometric lead iron tantalate, $PbFe_{1/2}Ta_{1/2}O_3$ (PFT), a close relative of PFN is considered as the next system for a systematic study of AFSG in this chapter. In this case the non-magnetic Nb^{5+} ion is isovalently substituted by Ta^{5+}.

4.1 Structural and magnetic properties

The chemical structures of PFN and PFT are essentially identical [57, 58]. At higher temperatures PFT crystallizes in $Pm3m$ cubic structure as in Fig. 1.13. Here, Pb^{2+} ions occupy corners of the unit cell, while oxygen octahedra surrounds Fe^{3+}/Ta^{5+} ions. The Fe^{3+} and Ta^{5+} ions are believed to be randomly distributed over the B-site of the lattice. Below 250 K, PFT undergoes a structural phase transition into tetragonal $P4mm$ phase finally settling into a monoclinic Cm structure at base temperature. Similar to PFN, the monoclinic distortions in PFT are rather insignificant [50, 71]. Also, Pb ions are found to be displaced from their (0, 0, 0) position in the whole temperature range as in other lead-based perovskites.

Despite the strong structural similarities, the magnetic properties of PFT are not very well understood in contrast to the generally accepted antiferromagnetic (∼143 K) and spin glass (12 K) transitions in PFN [61–63, 72]. One of the challenges with PFT is that indications of the magnetic transitions in *dc* magnetic susceptibility are strongly sample-dependent. For example, various sources reported AF transitions through anomalies in the *dc* magnetization in the range of 130-180 K [71, 73–75]. This transition was confirmed by the appearance of AF Bragg peak in neutron diffraction [76] suggesting a simple G-type structure with $\sim 3\mu_B$ magnetic moment per Fe^{3+} ion at base temperature [76]. However, first principle calculations of the electronic structure of PFT suggested the possibility of a second AF transition [77] at 48 K. This was claimed to be observed experimentally at ∼55 K by *Martinez* et.al [75]. In addition, the *dc*

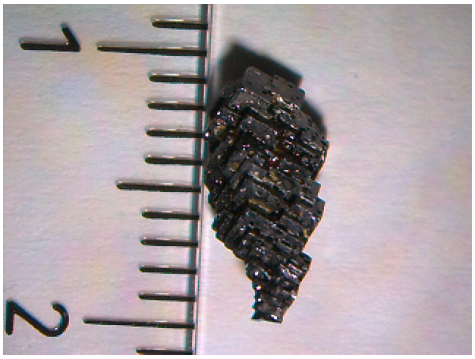

Figure 4.1: A photo of PFT single crystal (1x0.5x0.3 cm^3) used in the neutron scattering experiments.

susceptibility results by *Falqui* et. al showed a maximum in ZFC data around 9 K which exhibits properties of a spin glass transition [60]. Overall, there is uncertainty in the number and types of magnetic phases in PFT .

In the present work magnetic phase diagram of $PbFe_{1/2}Ta_{1/2}O_3$ is probed aiming to look out for a possible AFSG ground state. For this purpose bulk magnetization, neutron scattering and Mössbauer spectroscopy are employed to elucidate magnetic phase diagram. In order to eliminate metallurgical problems in identifying the temperatures of magnetic transitions, both ceramic and single crystal specimens are studied.

4.2 Samples & Experimental Methods

The PFT samples used in the present study were synthesized with the same procedure as employed for PFN , with sintering temperatures of 1100 °C, 1250 °C for ceramics and single crystals respectively.

Macroscopic measurements were made on ceramics and single crystals of PFT using a Physical Property Measurement System (PPMS). Conventional Mössbauer absorption spectroscopy experiments were conducted with the help of He-flow cryostat in transmission geometry on a powder of PFT with natural abundance of ^{57}Fe. Neutron scattering experiments were performed at the cold 3-axis spectrometer TASP (SINQ, Switzerland). A high-quality single crystal of PFT (see Fig. 4.1) was aligned in the $< hh0 > / < 00l >$ scattering plane in cubic notation so that the AF Bragg peak at the $\mathbf{Q}_{AF} = (\frac{1}{2}, \frac{1}{2}, \frac{1}{2})$ [71] position is reachable. Most of the neutron data were collected using $k_f = 1.55$ $\mathring{A}^{-1}$ and a collimation of *open-80′-sample-80′-80′*. Higher resolution results were obtained with collimation of *open-20′-sample-20′-20′*. A liquid nitrogen cooled Be-filter was used to suppress higher order contaminations. For polarized neutron diffraction, the MuPAD setup [78] was employed with a spectrometer configuration $k_f = 1.97$ $\mathring{A}^{-1}$, leading to an effective collimation *open-80′-sample-80′-open*. All the neutron data are analyzed by convoluting the respective scattering function with resolution of the spectrometer using *ResLib* package [79]. Details of the resolution calculation are provided in Appendix. B. The calculated resolution reproduces the measured Bragg peaks (110) and $(\frac{1}{2}, \frac{1}{2}, \frac{1}{2})$ leading to effective sample mosaicity values of 12′ and 20′ respectively in 20′-collimation and 80′-collimation setups. The effective mosaicity that is

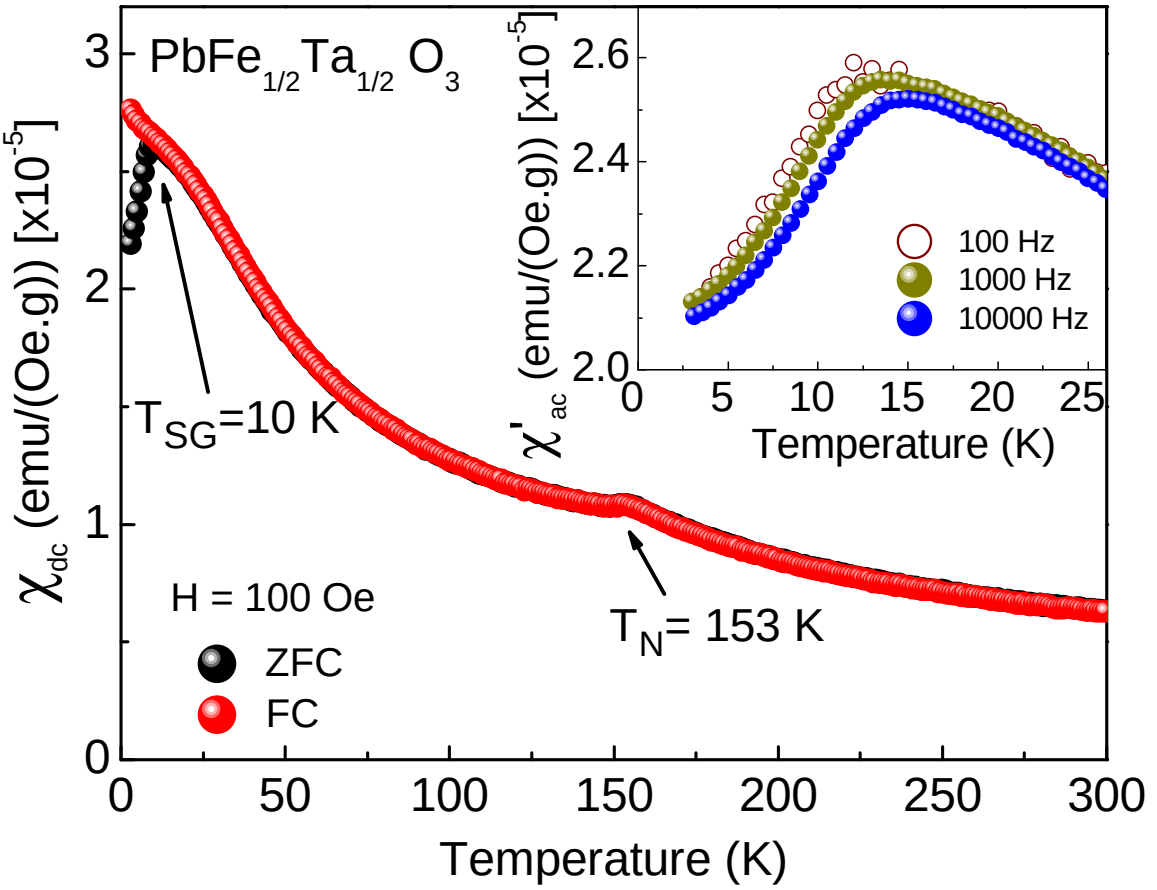

Figure 4.2: The *dc* susceptibility of PFT measured in a field of 100 Oe in standard ZFC and FC protocols for a ceramic sample. Inset (real part of *ac* susceptibility) shows frequency dependence of the broad peak at 10 K referring to the SG transition in PFT .

obtained for polarized data is 27′.

4.3 Results

4.3.1 Bulk Magnetization

An overview of the number of magnetic transitions in PFT is immediately revealed in macroscopic experiments. In Fig. 4.2, the *dc* magnetic susceptibility of ceramic PFT is shown for field-cooled (FC) and zero-field-cooled (ZFC) protocols as a function of temperature. At T_N ∼153 K, PFT undergoes paramagnetic (PM) to AF transition [71, 73–76]. Whereas, the low-temperature anomaly seen as a splitting of ZFC and FC data around 10 K suggests a second transition from AF into SG phase [60, 75]. The SG nature of this transition can be verified by the slow nature of dynamics. This result is further verified by gradual frequency dependence of the *ac* susceptibility. Inset of Fig. 4.2 shows a rounded peak around T_{SG} in *ac* susceptibility whose maximum shifts to higher temperatures upon increasing the field frequency. Magnetization in spin glass phase has another characteristic feature known as thermo remnant magnetization.

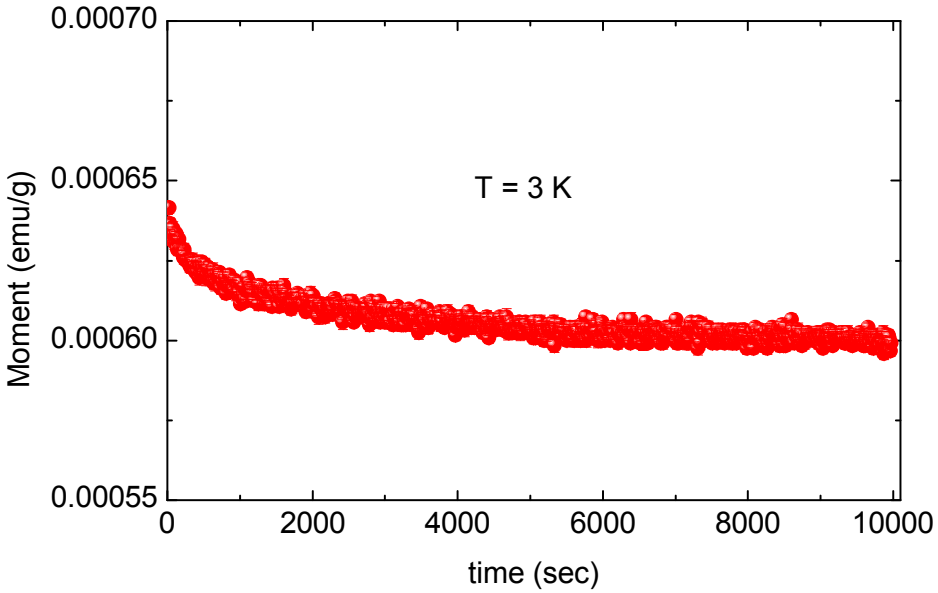

Figure 4.3: The relaxing thermo remnant magnetization measured in PFT below T_{SG}. Here, the sample was field cooled at 100 Oe to 3 K at a constant rate and the field was switched off to measure relaxation of the magnetization.

Here, if the system is cooled in a small external field to a temperature below T_{SG} (FC), the magnetization slowly relaxes to its ZFC value after the field is switched off. This behavior is clearly visible in Fig. 4.3. Similar measurements are performed on collections of small single crystals of PFT . These also give essentially the same results as for ceramic samples with T_N ∼158 K and T_{SG} ∼9 K concluding that the PFT samples with very different metallurgy have similar macroscopic properties as in PFN .

Further magnetic measurements of PFT are performed on a single crystal sample in order to better explore its magnetic phases. These measurements, through neutron scattering, allow us to study the evolution of short range magnetic correlations and presence of AF long-range order (LRO) in the SG state.

4.3.2 Neutron Scattering

As mentioned earlier, PFT has G-type [76] long-range AF order which produces a Bragg peak at $\mathbf{Q}_{AF} = (\frac{1}{2}, \frac{1}{2}, \frac{1}{2})$ position in neutron diffraction. Fig. 4.4 shows a color map of this Bragg peak measured in a high-resolution set up above and below T_{SG}. As depicted in the figure, a sharp resolution limited AF Bragg peak is observed that remains undisturbed while passing through the SG transition. Meaning, the true LRO persists into the SG phase.

In addition to the LRO, short-range correlations can also be observed by neutron diffraction in the form of diffuse scattering (DS). In PFT , these short-range correlations give rise to a broad peak under the sharp AF Bragg reflection as shown in Fig. 4.5.

Having observed these short-range correlations, the first step is to verify their magnetic origin. For this, polarized neutron scattering is used with neutron polarization vector parallel to the scattering vector $\mathbf{Q}$ (Fig. 4.6). In this geometry, scattering due to

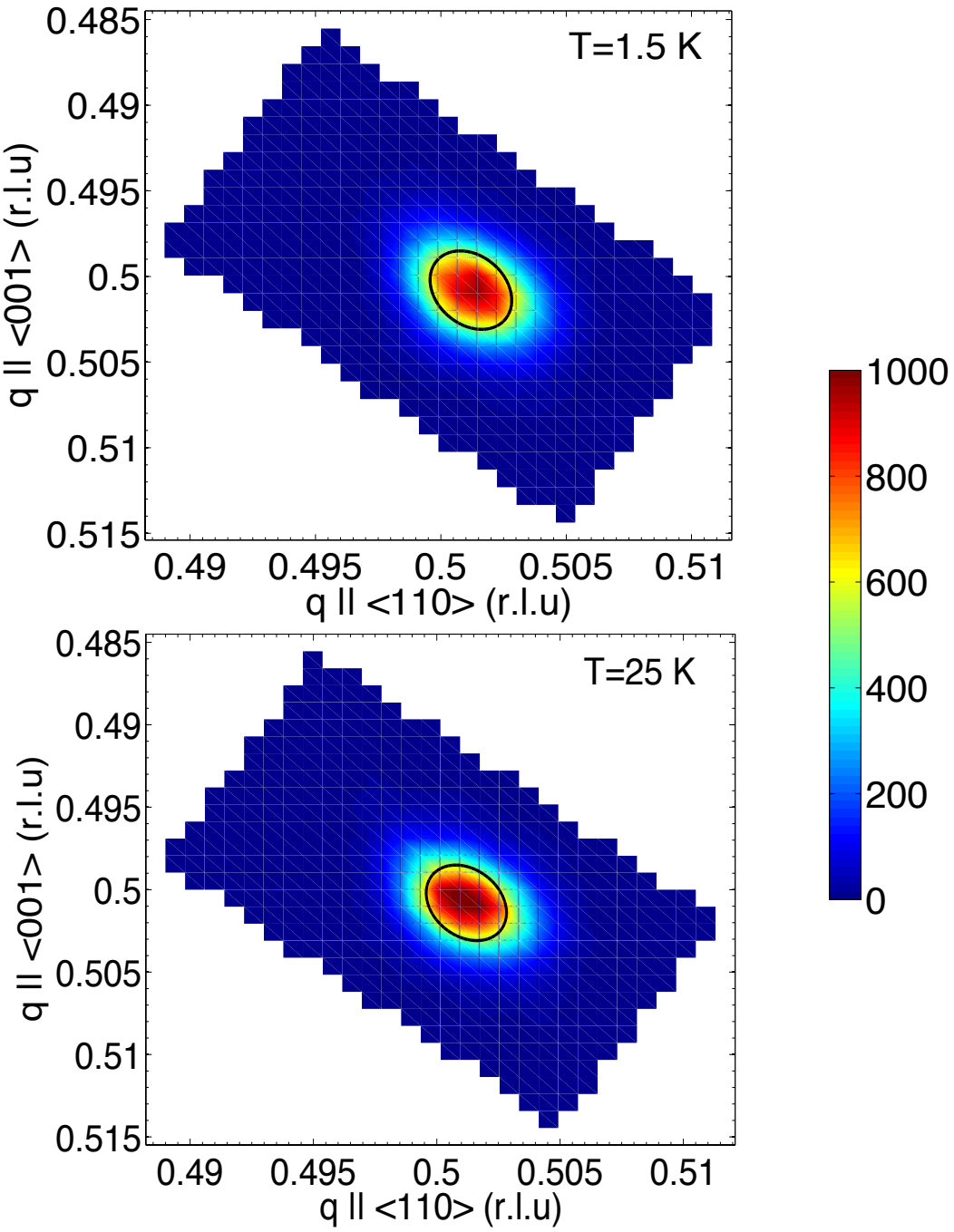

Figure 4.4: False color map of the elastic neutron intensity around AF Bragg peak at 1.5 K and 25 K respectively. Weak intensity surrounding the Bragg peak is a contribution from DS, which on this scale of wave vectors appears as (nearly) flat background. The resolution ellipse (black line), calculated from spectrometer parameters matches with the observed contour at half the maximum intensity.

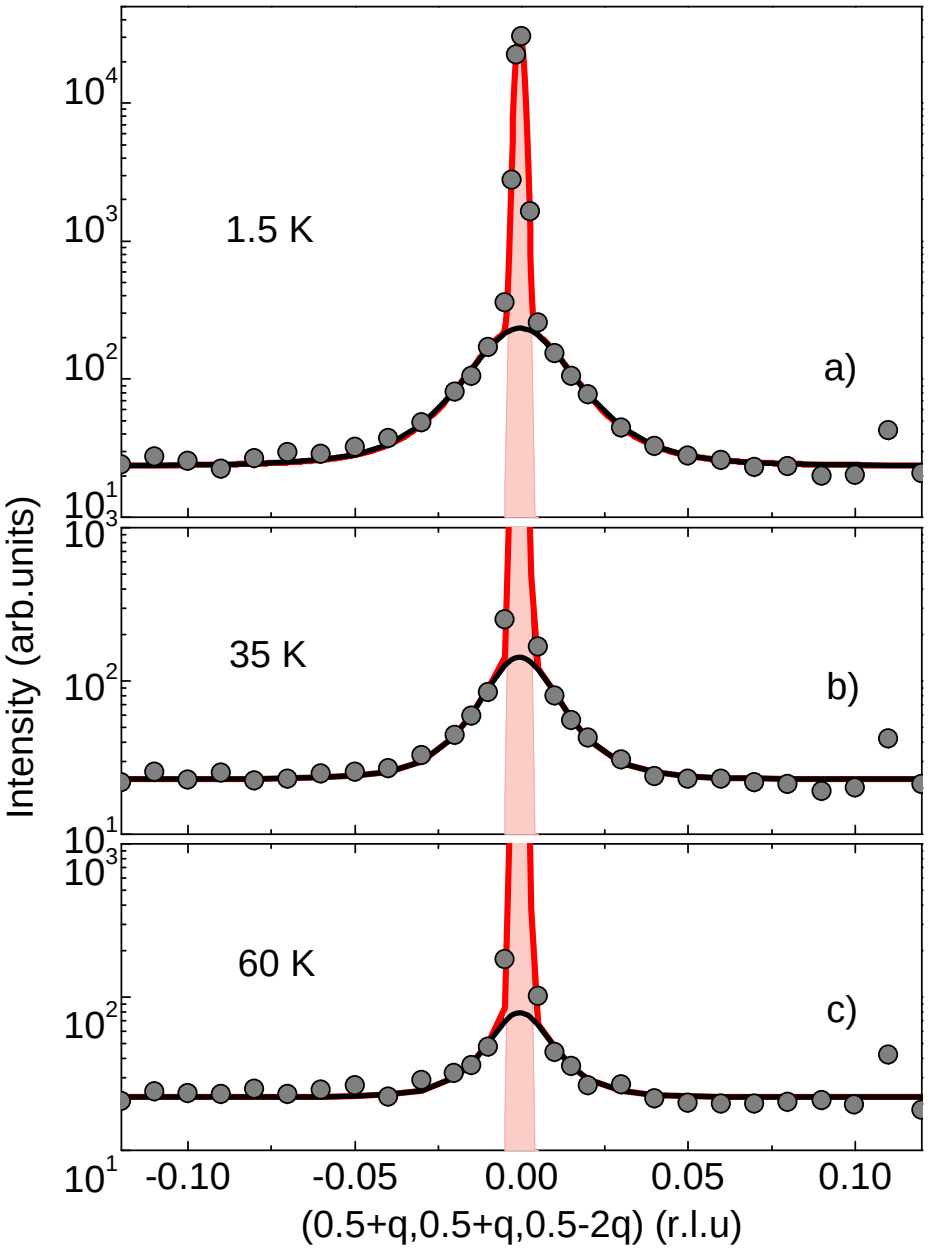

Figure 4.5: Elastic neutron diffraction scans around $\mathbf{Q}_{AF} = (\frac{1}{2}, \frac{1}{2}, \frac{1}{2})$ measured transverse to the scattering vector demonstrating temperature evolution of the AF Bragg peak and of the diffuse scattering. The data are collected using unpolarized neutrons. Logarithmic scale is used on Y-axis to highlight the relatively weak magnetic DS intensity. Solid lines are fits to the function Eq. 4.1-4.3 as described in the text. Red lines correspond to the best-fit results, shaded areas highlight the AF Bragg peak, and the black lines refer to the contribution from DS due to short-range correlations.

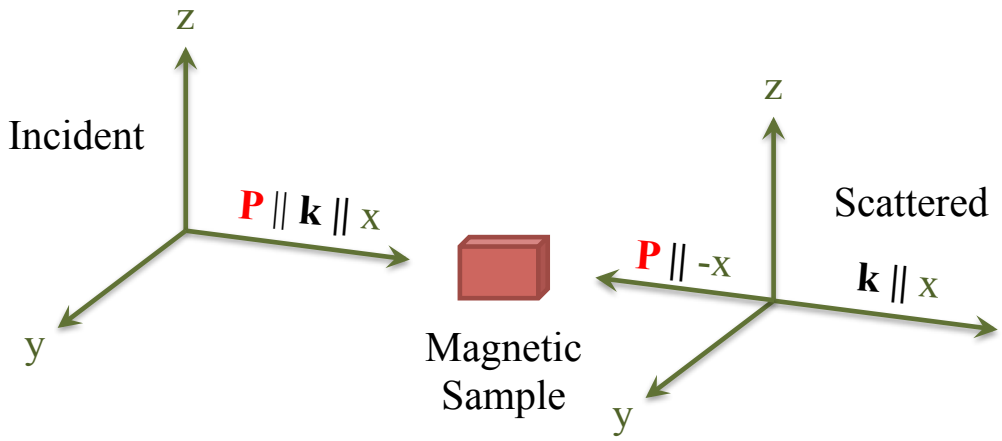

Figure 4.6: Sketch of the MuPAD geometry used for analyzing neutron spin polarization of diffuse scattering in PFT .

magnetic moments flips the direction of polarization whereas, the polarization state is retained if the scattering is of coherent nuclear origin. In PFT , the entire AF and DS intensity is observed in the spin-flip channel as shown in Fig. 4.7. There is nearly no scattering in non spin-flip channel as indicated in the the inset of Fig. 4.7a. Therefore, these short-range correlations are concluded to be of magnetic origin.

To obtain the time scale of the short-range correlations, several inelastic scans are measured through magnetic DS around AF Bragg peak. Fig. 4.8 shows one of the measured inelastic scans at (0.485 0.485, 0.53) close to the Q_{AF} in transverse direction. The observed inelastic peak is fitted with a single Lorentzian that describes exponential relaxation in energy convoluted with spectrometer resolution. Width of this Lorentzian function gives an estimate of the relaxation time of these short-range correlations. The fit results in width of $\sim 10^{-5}$ meV corresponding to fluctuations on the timescale longer than 10^{-11} s. Therefore, these correlations can be considered as quasi-static in nature.

Having established that the short-range correlations are magnetic and essentially static, a further assumption is made that they decay exponentially ($e^{-|\vec{r}|/\xi}$) with distance with some characteristic correlation length ξ. An exponential decay implies a lorentzian-squared form for the structure factor of the diffuse scattering. The total structure factor for quasielastic scattering is then written as:

$$S(\boldsymbol{k},T) = S_{AF}(\boldsymbol{k},T) + S_{DS}(\boldsymbol{k},T) \tag{4.1}$$

$$S_{AF}(\boldsymbol{k},T) = A(T)\delta(\boldsymbol{k}-\mathbf{Q}_{AF}) \tag{4.2}$$

$$S_{DS}(\boldsymbol{k},T) = B(T)\frac{\kappa}{\left[(\boldsymbol{k}-\mathbf{Q}_{AF})^2+\kappa^2\right]^2} \tag{4.3}$$

where $S_{AF}(\boldsymbol{k},T))$ and $S_{DS}(\boldsymbol{k},T)$ are the Bragg and the DS contributions, respectively. $A(T)$, $B(T)$ are temperature dependent integrated intensities of the AF and DS contributions respectively and κ, inverse correlation length of DS such that $\kappa = \frac{1}{\sqrt{\sqrt{2}-1}}\frac{1}{\xi}$.

The best fits of the data to the resolution convoluted scattering function defined above are shown by solid lines in Figs. 4.5, 4.7. This analysis is performed at each

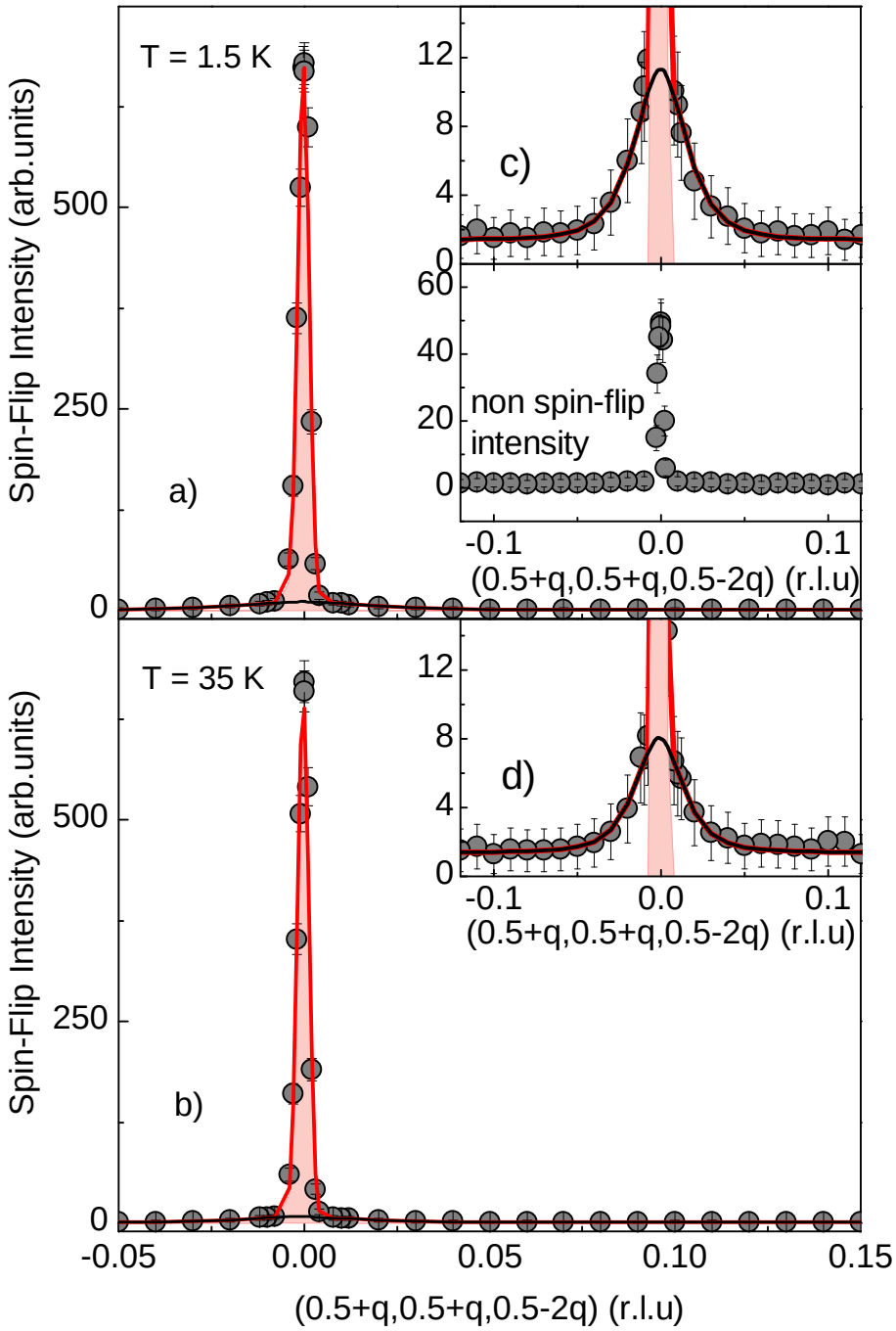

Figure 4.7: Polarized neutron elastic scans from PFT around $\mathbf{Q}_{AF} = (\frac{1}{2}, \frac{1}{2}, \frac{1}{2})$ demonstrating magnetic origin of the Bragg peaks and DS intensity. i.e, intensity in the non spin-flip channel (inset of a)) is negligible compared to that observed in the spin-flip channel (a)). c)-d) highlight the respective DS intensity in a)-b). Solid lines are fits to the functions Eq. 4.1-4.3 as described in the text. Red lines correspond to the best-fit results, shaded areas refer to the AF Bragg peak, and black lines emphasize contribution from the magnetic DS.

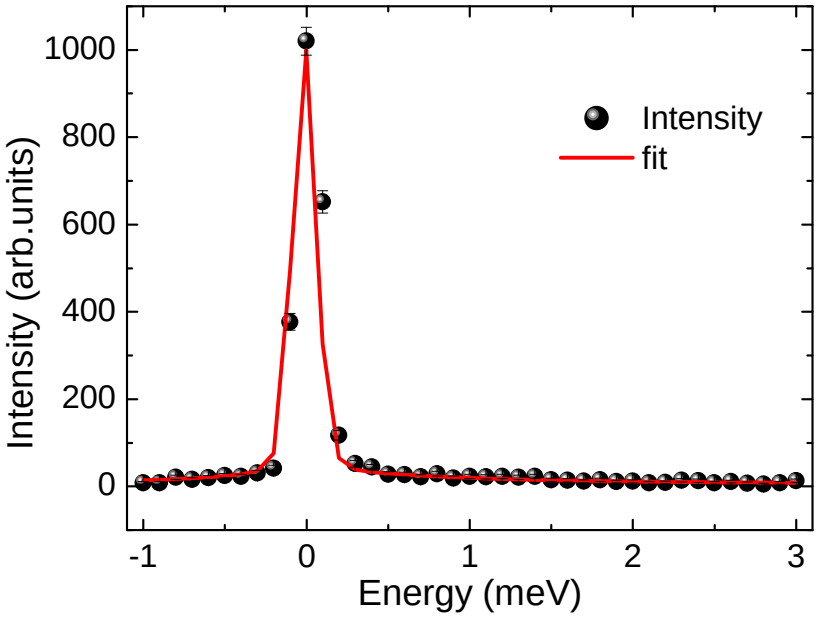

Figure 4.8: Inelastic scan of PFT centered at (0.485 0.485, 0.53) position in transverse direction from magnetic Bragg peak (0.5, 0.5, 0.5). Magnetic DS appears in this direction.

temperature to obtain the T-dependence of the inverse correlation length κ, as well as the intensities of the Bragg and diffuse components (Fig. 4.9). Intensity of the AF Bragg peak remains nearly unchanged in the covered temperature range as shown in Fig. 4.9a. The intensity of DS is weak and remains nearly constant for T$\geq$ 50 K. However, it increases rapidly upon lowering the temperature below 50 K. The width of the DS remains almost constant as shown in Fig. 4.9b, and the corresponding average correlation length is $\sim$ 10$\pm$2 Å.

4.3.3 Mössbauer spectroscopy

Similar to the approach used in PFN , Mössbauer spectroscopy experiments are performed on PFT for a clear proof of coexisting AF and SG order parameters.

Fig. 4.10 shows some of the ^{57}Fe Mössbauer spectra of PFT above and at several temperatures below T_N. The spectrum taken above Néel temperature, at T = 300 K, is shown in Fig. 4.10a. It exhibits a doublet structure with its center of weight shifted to δ = 0.301(2) mm/s (with respect to energy of $^{57}CoRh$ source kept at room temperature). As mentioned in the previous sections (Sec. 3), this isomer shift is mainly determined by the chemical shift and clearly corresponds to trivalent state of Fe. The doublet shape in the spectrum arises due to the quadrupolar splitting produced by a non-spherical charge distribution around the Fe^{3+} ion. Attempts to fit the spectrum of Fig. 4.10a assuming only one electric field gradient acting at Fe^{3+}, lead to unsatisfactory description with high χ^2 and an excessive line broadening similar to PFN . Instead, an adequate fit is achieved by assuming two contributions to the quadrupolar splittings $\Delta E_1 = 0.26(1)$, $\Delta E_2 = 0.50(2)$ as shown in Fig. 4.10a. Having two quadrupolar splittings at a single iron site is not surprising, as PFT is already in the ferroelectric phase

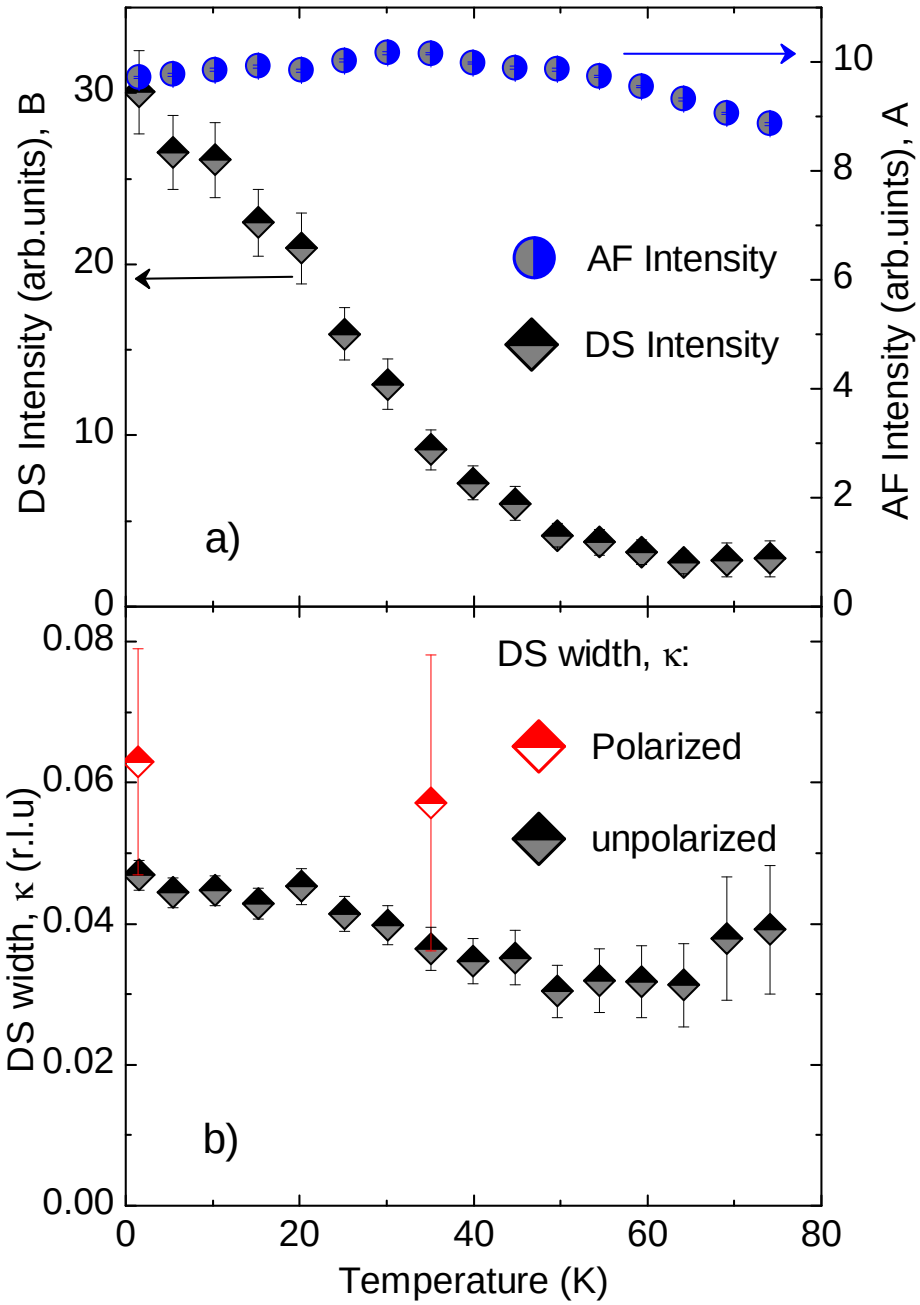

Figure 4.9: a) Integrated intensities of the diffuse scattering DS (left Y-axis) and the AF Bragg peak (right Y-axis) of PFT, b) Width of the neutron DS from PFT. The values of κ inferred from polarized and unpolarized data are in agreement.

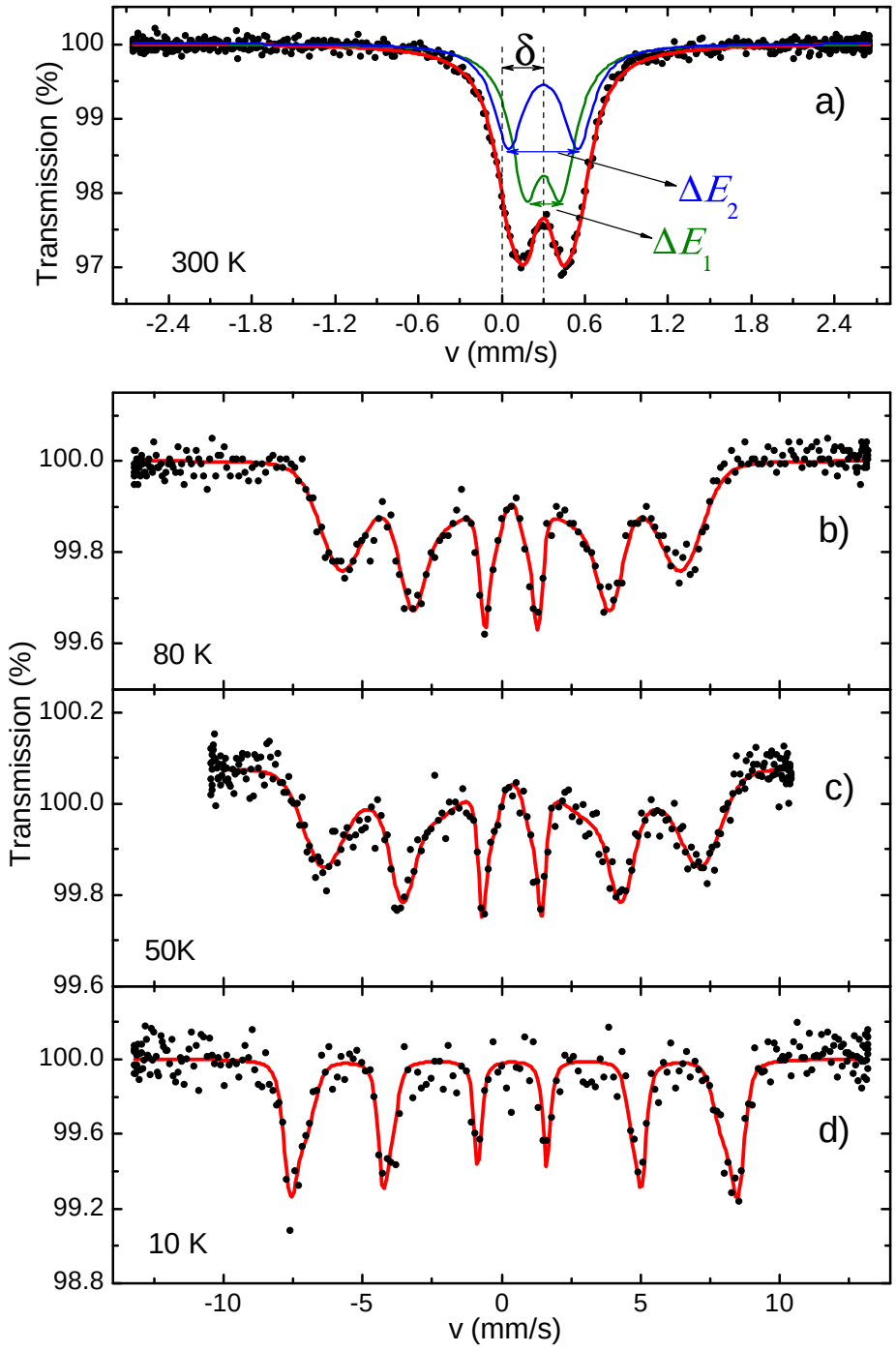

Figure 4.10: Mössbauer ^{57}Fe absorption spectra of PFT taken (a) above and (b)-(d) below T_N. Red lines are fits to the spectra as described in the text. Two components of the spectrum shown in Fig. 4.10(a) result from different quadrupole splittings ΔE_1, ΔE_2 detected in PFT .

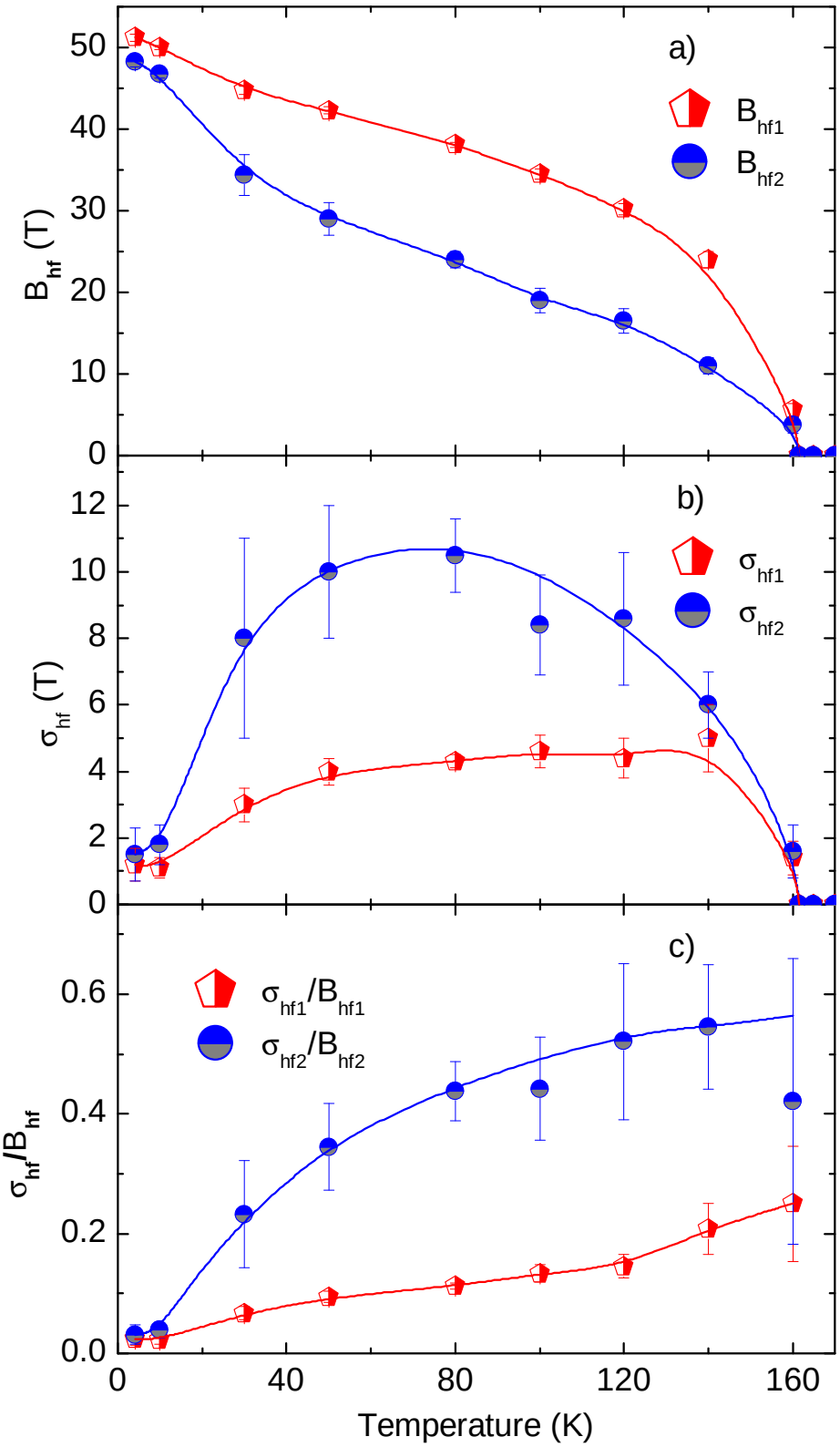

Figure 4.11: Temperature dependence of the model parameters obtained from fits of the Mössbauer spectra of PFT . Here, B_{hf1}, B_{hf2} are the mean values, and σ_{hf1}, σ_{hf2}: are widths of the two Gaussian hyperfine field distributions. $\frac{\sigma_{hf}}{B_{hf}}$ gives a measure of the relative distribution widths of the hyperfine fields. The lines are guide to the eye.

at T = 300 K and an additional deviation from the spherical approximation can be induced by different formal charges of disordered Fe^{3+} and Ta^{5+} ions. The ratio of areas of two components in the spectra is found to be 0.57(3):0.43(3).

Below Néel temperature (Figs. 4.10b-d), the Mössbauer spectra of PFT exhibit a sextet pattern. This is to be interpreted as a direct evidence of Zeeman splitting of the ^{57}Fe nuclear levels induced by the spontaneous magnetization of the material. No central (unsplit doublet) contribution similar to the spectrum shown in Fig. 4.10a could be detected. This rules out the existence of remaining paramagnetic clusters [74] below T_N and clearly indicates that all Fe^{3+} in PFT are involved in creating AF long range order. The nuclear-quadrupole splitting which was the dominant effect of the spectra in the paramagnetic state is not detected below T_N. This points to a wide distribution of the angles between the iron spins and the local axes of the electric field gradient tensor in the AF state. The sextet itself is noticeably broadened at higher temperatures. At base temperature, this broadening nearly vanishes and sharp absorption lines are observed indicating static and rather uniform local fields around Fe^{3+} sites.

To obtain more quantitative information from Mössbauer data, the spectra taken below T_N were fitted with hyperfine fields having Gaussian distributions (see Fig. 4.10b-d). A consistent fit for all the spectra can be obtained with a single isomer shift for Fe^{3+} assuming two distributions of the hyperfine fields in the same ratio as was inferred from the data in paramagnetic phase. Fig. 4.11a shows the temperature dependences of the amplitudes of both hyperfine fields B_{hf1} and B_{hf2}. B_{hf} for the two contributions increases smoothly on cooling from T_N down to ∼50 K. Below 50 K a faster increase of B_{hf} is observed, and both finally reach essentially the same value of ∼50 T at 4 K. This value is very close to the saturated hyperfine field in other Fe containing oxides [72], [66] and thus suggests that Fe^{3+} in PFT recovers its full moment at base temperature. The strong temperature dependence of the gaussian widths σ_{hf1}, σ_{hf2} (see Fig. 4.11b) suggests that the origin of observed distributions of the hyperfine fields is due to dynamic fluctuations. This dynamic nature is seen even better through the temperature evolution of the ratio $\frac{\sigma_{hf}}{B_{hf}}$ shown in Fig. 4.11c. These relative widths of B_{hf1} and B_{hf2} decrease monotonically as temperature is lowered. For both contributions it reaches the same and vanishingly small value at base temperature. This implies negligible contribution from static fluctuations to the broadening of the Mössbauer spectra.

The features of the Mössbauer spectra below T_{SG} unambiguously confirm a homogeneous environment for all Fe^{3+} ions in the system, and a uniformity of the *magnitude* of the moments at saturation. Since neutron scattering demonstrated an *increase* of short-range correlations in this regime, the disorder at low temperature is concluded to be purely orientational. In addition, slowing down of the hyperfine field fluctuations results in a rapid increase of the local Fe moment below 50 K. In contrast, the ordered magnetic moment seen by neutrons remains nearly unchanged (possibly reduces slightly) below this temperature. A clear difference in the behavior of local and staggered magnetic moments below ∼ 50 K indicates canting of Fe moments. A similar behavior was observed in amorphous metallic glasses Fe-Mn, Fe-Zr, Au-Fe and was ascribed to the spin canting [80–82]. This further validates our interpretation of the observations in PFT . Therefore, these results for PFT support the same scenario for the AFSG phase, as was suggested for PFN (Sec. 3.4).

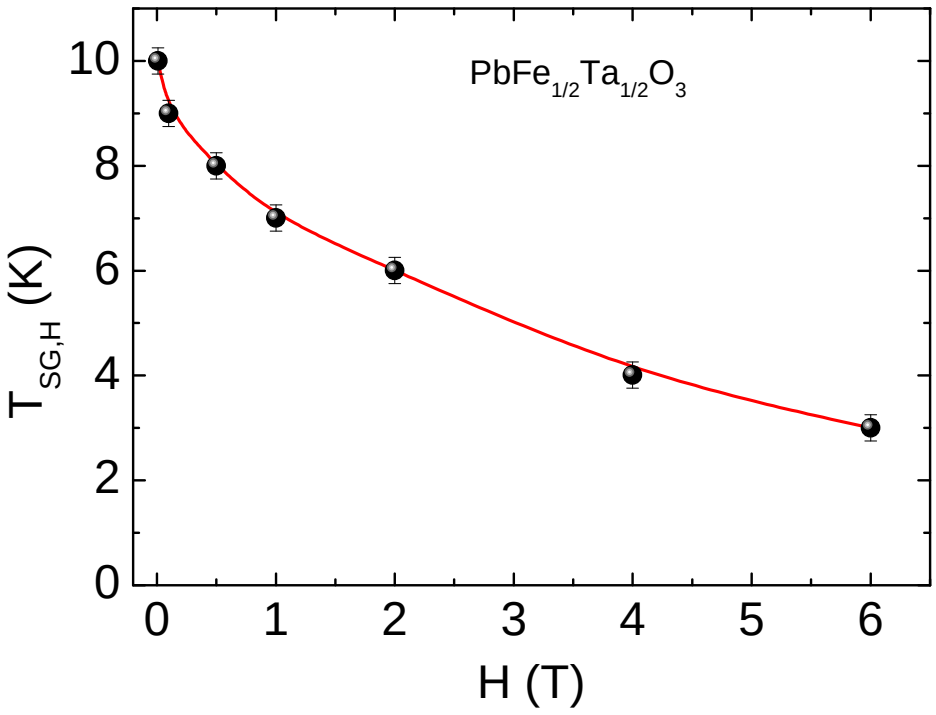

Figure 4.12: Phase diagram of T_{SG} as a function of external applied magnetic field in PFT.

4.4 Field dependent phase diagram

PFT is an alternative material to understand the magnetic interactions responsible for the AFSG ground state. The obvious choice to quantitatively measure these interactions is through the measurement of spin wave dispersion. However, as shown in Appendix. A.2, the inelastic neutron scattering in PFT does not reveal magnetic excitations and therefore, the exchange constants are still unknown.

Therefore, H-T phase diagram is measured so that the result can be compared to one of the existing models in order to qualitatively understand the interplay of magnetic interactions responsible for AFSG. Here, the static field is applied on a mosaic collection of PFT single crystals. We see that T_{SG} continuously decreases as the external field increases (Fig. 4.12). However, this decrease does not follow the G-T line predicted for transition from long-range FM to coexisting FMSG Heisenberg systems. This behavior is again identical to PFN .

4.5 Summary

The magnetic properties of PFT are essentially identical to those of PFN , similar to their structural counterpart. PFT undergoes only two magnetic phase transitions: one of which is AF (T_N ~153 K) and the other is SG (T_{SG} ~10 K) to the AFSG ground state, contrary to the previous claims of two Néel temperatures, namely T_{N1} ~160 K and T_{N2} ~48 K [75, 77]. The neutron scattering experiments allow the association of latter temperature with the enhancement of magnetic short-range correlations in

the sample which are further developed as T_{SG} is approached. These correlations are revealed by an increase of the integrated intensity of the DS scattering (Fig. 4.9a), a feature also observed in PFN [61]. In PFT , the measured correlation length 10 ± 2 $\mathring{A}$ corresponds to nearly two lattice constants which clearly suggests that magnetic interactions beyond first nearest-neighbor are important.

Temperature evolution of Mössbauer spectra show that the fluctuations in hyperfine field slow down as T_{SG} is approached, in accordance with increasing intensity of short-range correlations. These fluctuations nearly vanish at the base temperature and hyperfine field attains saturation meaning that a ground state has been approached.

The spin glass transition temperature T_{SG} below which AFSG exists is seen to decrease upon the application of an external magnetic field. This indicates that the external field reduces the degree of competition of short-range (spin glass) and long-range (AF) orders while preferring the latter.

Considering the overwhelming number of similarities in the magnetic properties of PFT to that of PFN , the same speromagnet-like model can be attributed to the spin arrangement of AFSG ground state as depicted in Fig. 3.10.

Chapter 5

Effect of magnetic ion concentration on AFSG

$PbFe_{2/3}W_{1/3}O_3$

In the previous chapter, we have seen that the substitution of a non-magnetic ion at the disordered site does not disturb the magnetic ground state in PFN. Therefore, we now consider a system having higher magnetic ion concentration at the disordered site i.e, 67% compared to 50% in PFN and PFT. However, the condition of charge neutrality to maintain stoichiometric composition in this complex perovskite does not allow us to retain the same non-magnetic ion while increasing the magnetic ion concentration. Therefore we consider $PbFe_{2/3}W_{1/3}O_3$ *as our system of interest.*

5.1 Structural and magnetic properties

PFW is a cubic perovskite at room temperature with lattice parameter $a = 3.989$ Å. X-ray and neutron diffraction data suggest that the cubic structure with space group *Pm3m* is retained at all temperatures [83, 84]. The structure of unit cell of PFW is similar to PFN and PFT . Here, Fe^{3+}/W^{6+} sit at the center of the octahedron formed by oxygen ions (c.f. Fig. C.1) and Fe^{3+}/W^{6+} are randomly distributed in the sample. The Pb^{2+} ions at the corners of the cubic unit cell are known to be displaced from their ideal (0, 0, 0) positions, a feature typical to the family of Pb-based perovskites [83]. However, the displacements of Fe^{3+}/W^{6+}, and oxygen have also been suggested [85].

There are very few reports on the magnetic properties of PFW. An anomaly in *dc* magnetization has been reported at T_N= 340–370 K indicating a paramagnetic to antiferromagnetic phase transition [83–85]. The magnetic structure of PFW is found to be a G-type antiferromagnetic arrangement of Fe^{3+} ions through powder and single crystal neutron diffraction [83]. The magnetization data also suggest a second anomaly at lower temperatures ranging from 7–20 K. This is interpreted as an evidence for a possible second AF phase transition in PFW [84] or a transition into weak ferromagnetic phase [85]. However, neither of these two interpretations are conclusive because: a) *dc* magnetization at different FC/ZFC protocols was not measured, b) the *ac* susceptibility measurements in the vicinity of this second anomaly were not performed. Moreover,

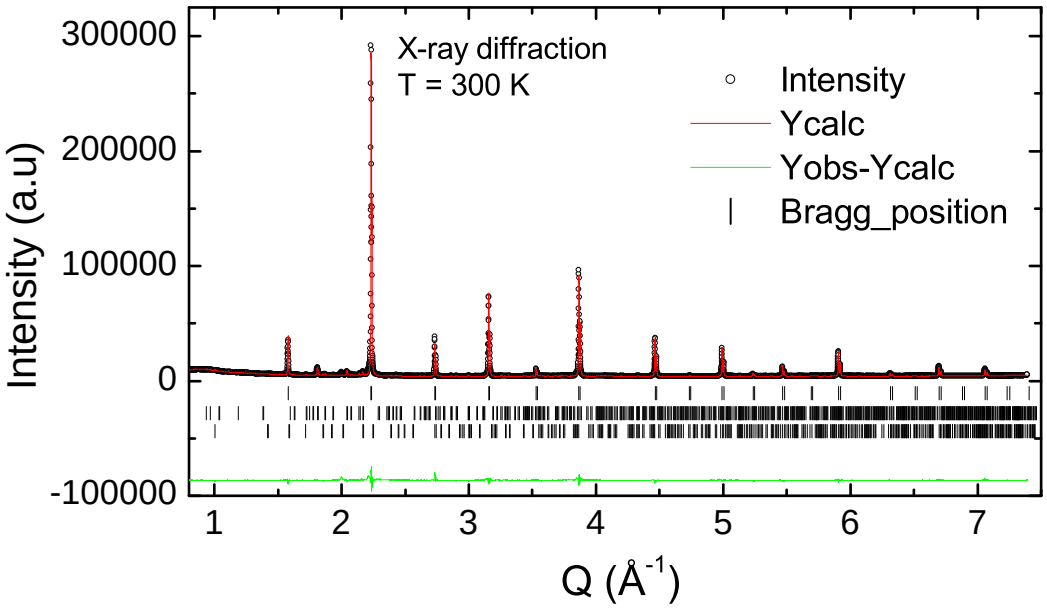

Figure 5.1: X-ray diffraction pattern of PFW taken at room temperature.

this anomaly is not consistent in all the reported magnetization data adding to the ambiguity [83, 86].

The sequence of two anomalies i.e, AF at high temperature and a second anomaly at low temperature resemble the AF and spin glass transitions respectively, observed in PFN and PFT . Considering the similarity, one may expect to see the appearance of a spin glass phase in PFW below ∼20 K anomaly. As the FC/ZFC magnetization was not measured before, the possibility of a spin glass phase at low temperatures cannot be verified. Therefore, the goal of this study is to probe the sequence of magnetic transitions in $PbFe_{2/3}W_{1/3}O_3$ and verify its magnetic ground state.

5.2 Experimental methods

Ceramic samples of $PbFe_{2/3}W_{1/3}O_3$ are used to measure bulk magnetization using Physical property measurement system (PPMS). The ceramic sample is prepared following the same technique used for PFN samples. Chemical purity of the sample is verified by x-ray diffraction at room temperature. The resulting pattern shown in Fig. 5.1 is fitted with Rietveld method using FullProf program (described in Appendix. C.1). The refinement results in a cubic perovskite structure for PFW with ∼99% volume fraction and a non-magnetic impurity of ∼1% in the form of Pb_2WO_5. Therefore, the sample can be used to measure magnetic properties of the system.

Neutron diffraction studies were performed at the High-Resolution Powder diffractometer HRPT at SINQ in Paul Scherrer Institute (PSI), Switzerland. The powder sample was filled in a vanadium can (of 6 mm diameter) and measured in temperature range of 5–550 K with a neutron wavelength λ=1.1545 $\AA$. The measurement covers a 2θ angle of 10-160°. All the obtained diffraction data is refined with the Rietveld method using FullProf program. Further details of the refinement strategy are explained in the Appendix. C. ^{57}Fe Mössbauer spectra of PFW are obtained using a CoRh source for

several temperatures between 6–360 K using a He flow cryostat.

5.3 Results

5.3.1 Bulk Magnetization

Bulk *dc* susceptibility of PFW is measured in ZFC and FC protocols between 2–390 K as shown in Fig. 5.2a. The ZFC curve clearly shows three anomalies in the susceptibility. The anomaly at T_N = 350 K matches with the reported antiferromagnetic transition.

A second anomaly in ZFC occurs at T_{an} = 7 K, consistent with the previous reports. The reduction of *dc* susceptibility below T_{an} resembles that of the spin glass transition in PFN and PFT at T_{SG}∼10K, however with a marked difference. In the latter two compounds, ZFC strongly deviates from FC susceptibility only below T_{SG}. The two curves collapse on to the same line above this temperature indicating the appearance of magnetic irreversibility below T_{SG}. Whereas, the ZFC and FC in PFW do not merge together in the entire temperature range even above T_N into the paramagnetic state. This strong history dependence of χ_{dc} in ZFC/FC points to the presence of a possible ferromagnetic impurity in the sample. In addition, ZFC shows a third anomaly at T_m = 170 K whose origin is not accounted for.

To verify the nature of the two anomalies at T_{an} = 7 K and T_m = 170 K magnetization of PFW is further measured through *ac* susceptibility. Fig. 5.2b shows real part of χ_{ac} in PFW clearly reproducing both these anomalies. However, the susceptibility shows frequency dependence for temperatures below T_m = 170 K down to 3 K. Moreover, the position of the anomaly at T_{an} = 7 K does not shift with frequency. Hence, a spin glass transition can be ruled out in PFW below ∼7 K. Secondly, the magnitude of the anomaly in χ_{ac} at 170 K is highly pronounced compared to its value in χ_{dc}. Such a behavior is common to the anomalies of ferromagnetic nature in contrast to the antiferromagnetic anomalies. For example, the T_N anomaly in PFN is of nearly same magnitude in both *ac* and *dc* susceptibilities (Fig. 3.2). Altogether, the temperature dependent susceptibilities hint to the presence of ferromagnetic impurity in the sample.

A sure way of detecting the ferromagnetic contribution is through the evolution of remanence magnetization in a sample. Therefore, magnetization of PFW sample is measured as a function of external field (-9–9 T) covering the temperature range 4–380 K. The M-H curve at 4 K, in Fig. 5.3, is strongly non-linear due to the antiferromagnetic ordering in the sample. However, a small hysteresis loop with remanence magnetization 0.087 emu/g is observed indicating a ferromagnetic contribution. At 190 K, the curve is less non-linear compared to 4 K but the hysteresis loop persists with remanence magnetization pinned to the value observed for 4 K. As the temperature is increased further, we observe that this remanence survives even above AF transition up to 380 K(inset of Fig. 5.3). This implies a consistent ferromagnetic contribution to the magnetization of the sample whose remanence magnetization changes very little in the temperature range of 4–380 K. However, bulk magnetization data does not allow us to identify the nature of this ferromagnetic contribution i.e., whether it is an intrinsic property of PFW or a ferromagnetic impurity.

The bulk magnetization of PFW leaves two questions to be answered. First, what kind of magnetic phase transition does PFW undergo below 7 K. Second, is the fer-

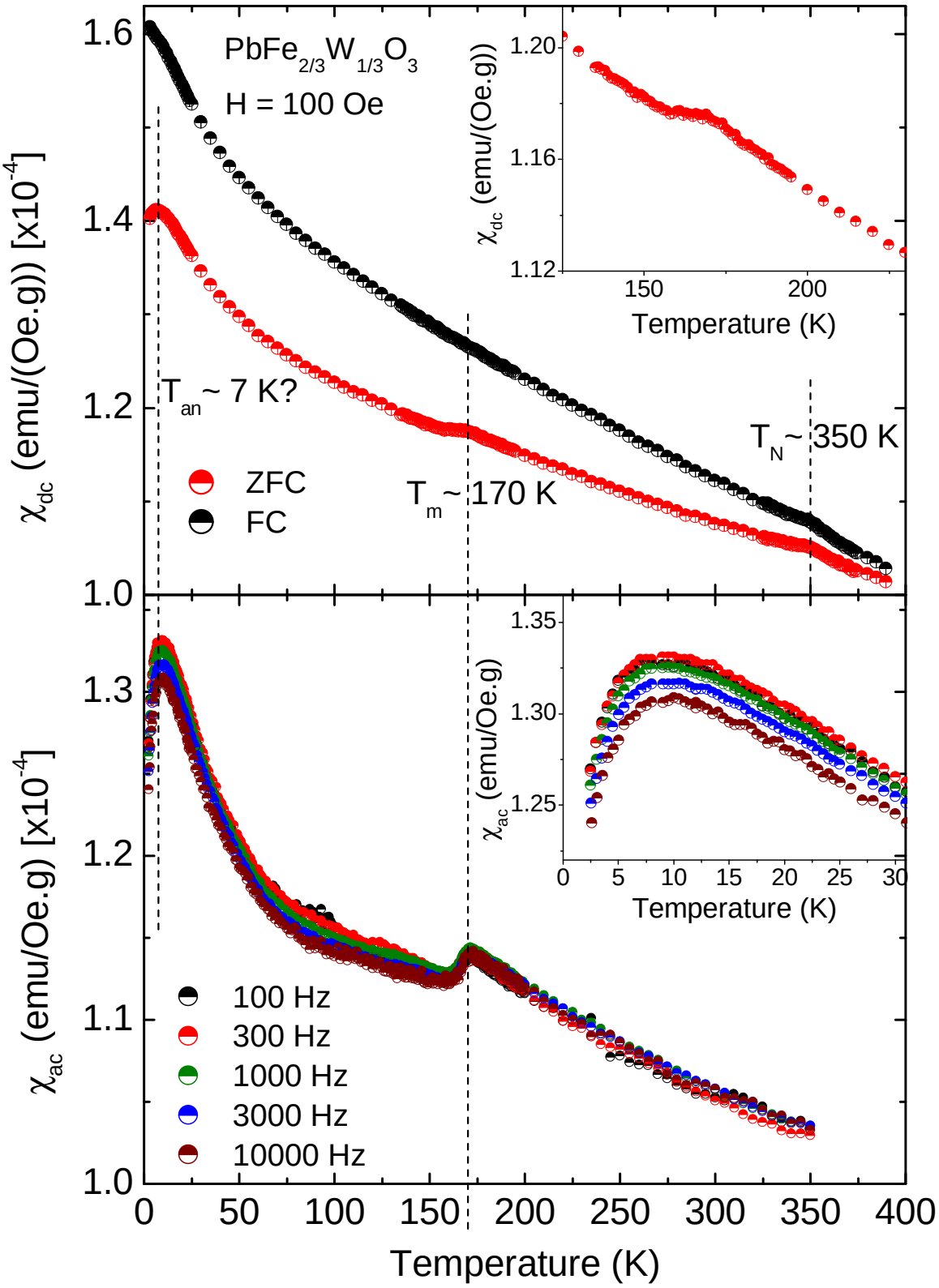

Figure 5.2: (a) The *dc* susceptibility of ceramic PFW measured in 100 Oe applied field following ZFC and FC protocols. (b) The *ac* susceptibility taken in the range 10^2 - 10^4 Hz.

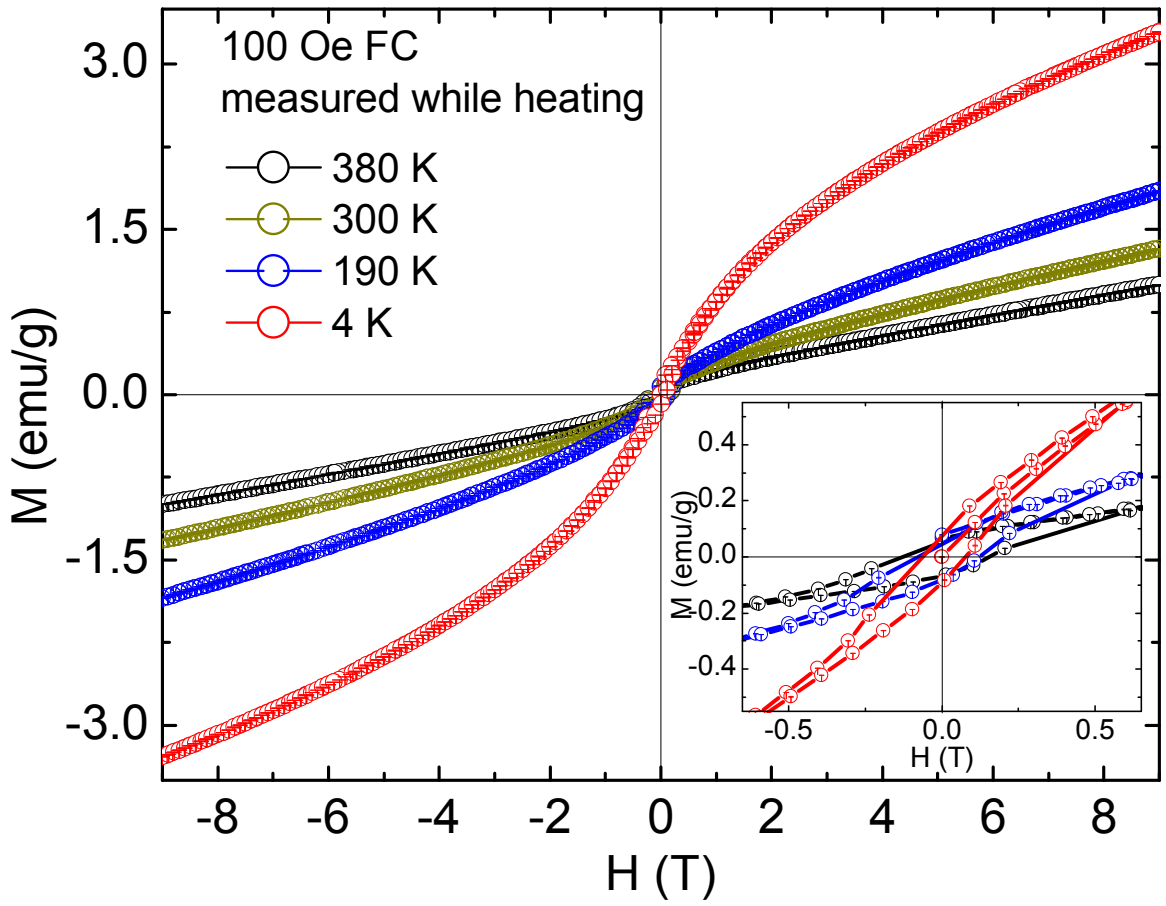

Figure 5.3: Magnetization of PFW ceramic sample measured at various temperatures for T = 4 K, 190 K, 300 K and 380 K. The inset clearly shows unchanging remanence magnetization in the sample even in the paramagnetic state.

romagnetic contribution to the magnetization intrinsic to PFW . To answer the first question one has to first establish the antiferromagnetic structure that sets in at 350 K and track changes in the magnetic structure below 7 K. This is best done by analyzing neutron diffraction pattern as a function of temperature. The second question is addressed through Mössbauer spectroscopy which will allow us to differentiate between sample's intrinsic and impurity contribution to the local magnetic hyperfine field of ^{57}Fe.

5.3.2 Neutron powder diffraction

Fig. 5.4 shows some of the measured neutron diffraction patterns on powder sample of PFW . The patterns below T_N =350 K readily confirm the AF transition by the appearance of a magnetic Bragg peak at wave vector $(\frac{1}{2}, \frac{1}{2}, \frac{1}{2})$. This magnetic Bragg peak survives down to 1.5 K. A consistent description of the nuclear and magnetic structure of PFW at all temperatures are obtained by refining the data considering cubic structure in *Pm3m* space group which is combined with G-type antiferromagnetic structure below T_N. The moment of antiferromagnetic structure gradually evolves (in Fig. 5.5) without any significant anomalies in the Fe moment at 175 K, assuring that the corresponding anomaly in χ_{dc} and χ_{ac} does not originate from antiferromagnetic PFW . However, a dip in the moment is observed at low temperature, consistent with T_{an} anomaly in χ_{dc} and χ_{ac}. Although, this reduction does not correspond to any changes in the description of antiferromagnetic Bragg peak. Therefore, we can conclude that PFW is a G-type antiferromagnet for all the temperatures below T_N. For further details of the neutron diffraction results related to the chemical structure please refer to Appendix. C.

To clarify the nature of ferromagnetic contribution in the sample we probe the magnetization in PFW with a local technique, Mössbauer spectroscopy.

5.3.3 Mössbauer Spectroscopy

Fig. 5.6 shows some of the ^{57}Fe Mössbauer spectra of PFW above and below T_N. Above Néel temperature, the spectrum exhibits a doublet structure similar to PFN and PFT . The center of gravity of this spectrum is shifted by $\delta = 0.301(2)$ mm/s (with respect to energy of $^{57}CoRh$ source) indicating that the Mössbauer Fe is in trivalent state. However, unlike PFT or PFN the doublet cannot be associated with a quadrupole splitting in the sample as there is no evidence for charge asymmetry at ^{57}Fe nuclei which could lead to electric field gradient. Below T_N, the doublet structure disappears with simultaneous emergence of a sextet as a result of Zeeman splitting of the energy levels due to antiferromagnetic ordering of Fe^{3+}, similar to the observations of Ref. [87].

An important clue to the nature of ferromagnetic contribution in PFW can be extracted from the absence of a corresponding magnetic sextet in all the spectra. From the M-H loops in 4–380 K temperature range, it is clear that the remanence magnetization in the sample remains nearly constant. Meaning, this contribution is nearly at its saturation. In this case, one should expect a sharp sextet from the ferromagnetic part in the Mössbauer spectra. At 360 K (where no AF ordering occurs), this should lead to two clearly separated inner lines of the sextet (like the ones at 20 K). Instead,

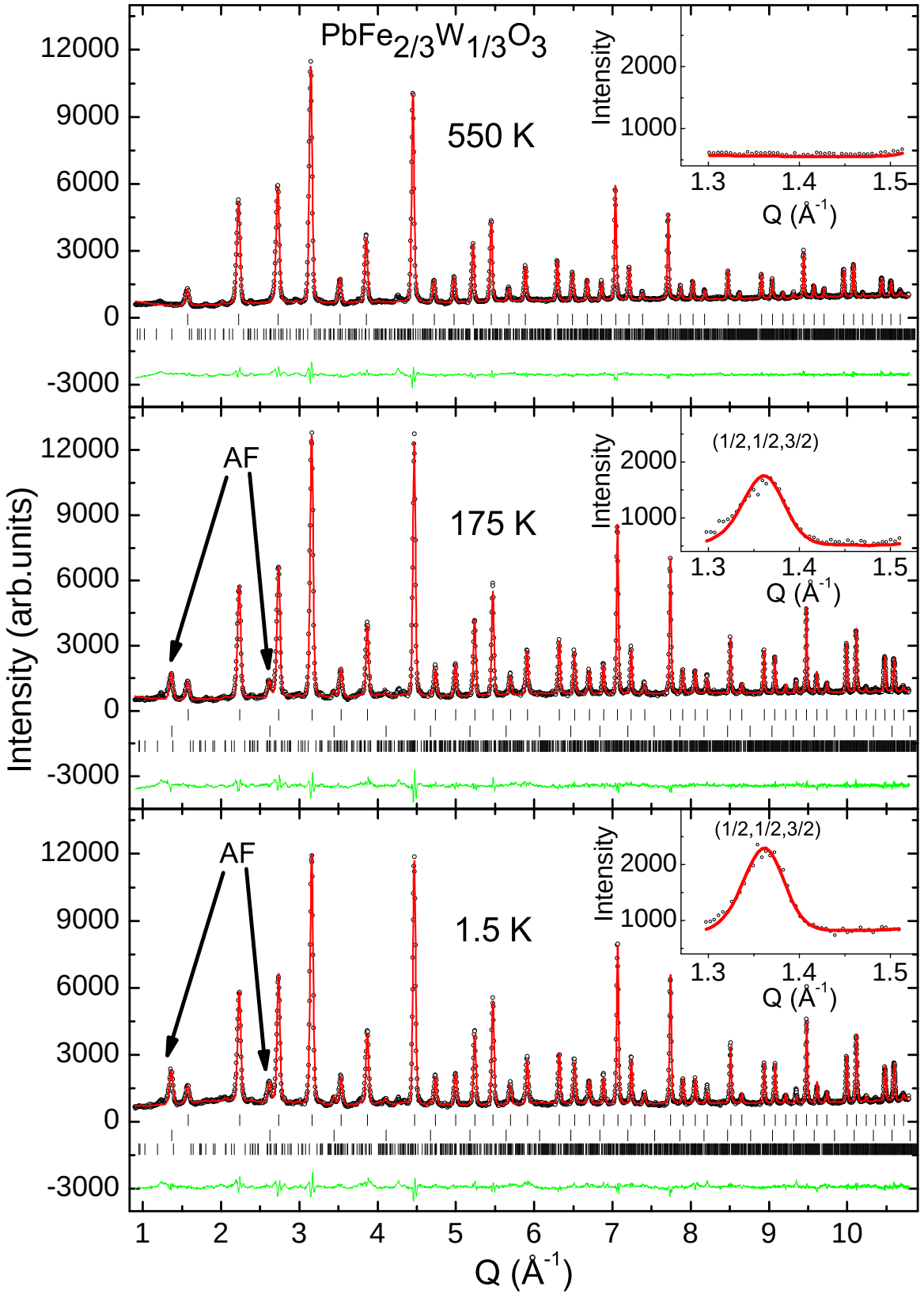

Figure 5.4: Representative neutron powder diffraction patterns of PFW taken in the paramagnetic phase and below its Néel temperature. The insets clearly show the evolution of magnetic peak at $(\frac{1}{2}, \frac{1}{2}, \frac{3}{2})$ position.

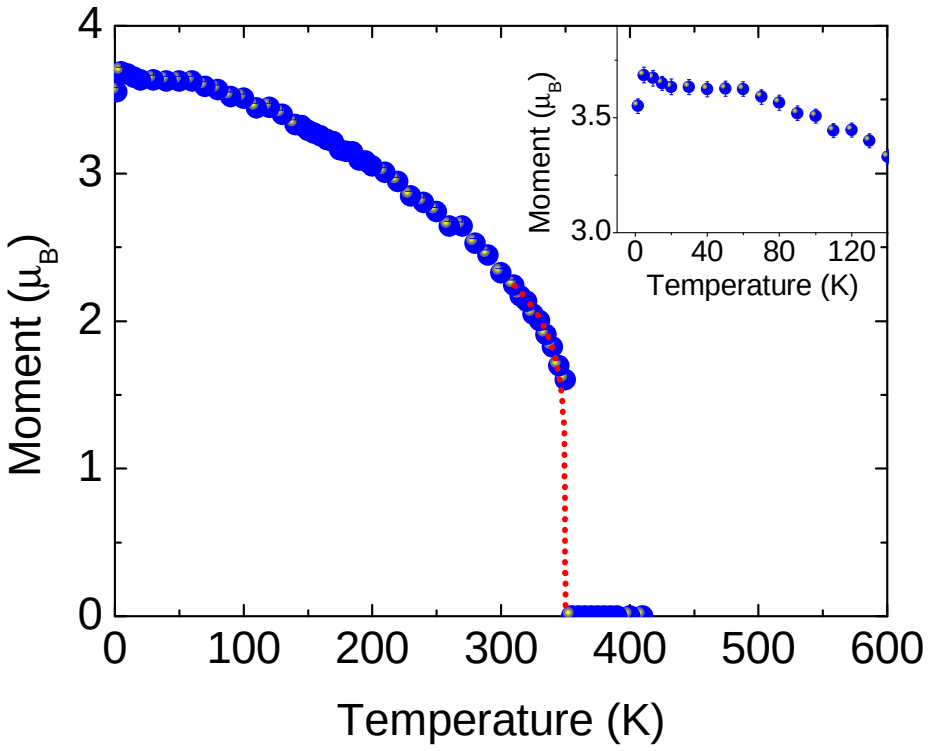

Figure 5.5: Evolution of magnetic moment per Fe^{3+} ion in PFW as observed through neutron powder diffraction.

only the doublet structure is visible. Therefore, we can conclude that the ferromagnetic contribution to the sample is due to a ferromagnetic impurity whose concentration is very small and hence the signal is lost in the background.

5.4 Summary

The Bulk magnetization data of PFW reproduce the AF anomaly at $T_N = 350$ K and low temperature anomaly at T_{an}=7 K. The latter anomaly cannot be ascribed to a spin glass transition due to its frequency independent nature of the ac susceptibility. Rather, neutron diffraction suggest that PFW remains a G-type antiferromagnet below this temperature. However, a strong proof of ferromagnetic contribution is observed in the sample through the presence of remanence magnetization in M-H loops and history dependence of FC/ZFC susceptibilities in the entire temperature range (4–380 K). The absence of corresponding sextet in the Mössbauer spectra therefore, suggests that it belongs to a ferromagnetic impurity whose concentration is too small (less than 1%, as observed from x-ray diffraction) to be detected. Therefore, these results are not entirely reliable to conclude the magnetic ground state of PFW .

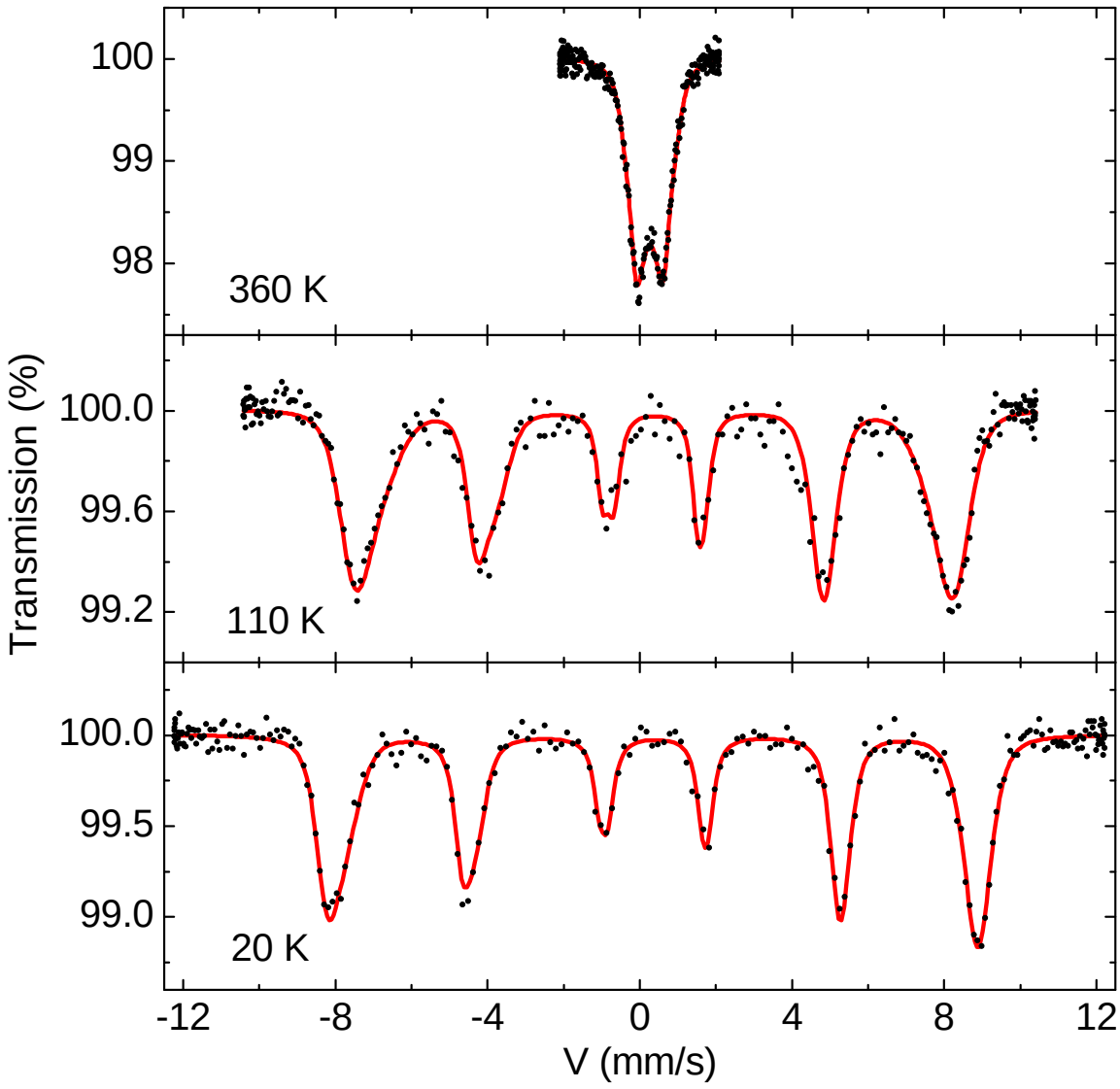

Figure 5.6: Mössbauer spectra of PFW measured in paramagnetic phase and below Néel temperature. The solid lines are guides to the eye.

$PbCo_{1/3}Nb_{2/3}O_3$

In this section, we consider a system with lower magnetic ion concentration. The ideal choice to obtain such a system would be to reduce Fe concentration in PFN . However, this will lead to non-stoichiometric chemical composition in the system leading to undesirable effects such as clustering or multiple valancies of Fe. This problem can be avoided by choosing a stoichiometric concentration, in which case the magnetic ion in PFN is substituted with 33% Co leading to $PbCo_{1/3}Nb_{2/3}O_3$. Even though the absolute magnetic concentration in PCN is small, it is higher than the percolation threshold for a site disordered simple cubic system. Therefore, the system is expected to have magnetic ordering.

5.5 Structural and magnetic properties:

$PbCo_{1/3}Nb_{2/3}O_3$ has a perovskite crystal structure as shown in Fig. 1.13 for PFN and PFT . Owing to the charge neutrality, the chemical composition leads to a random distribution of Co^{2+} and Nb^{5+} ions at the B-site. At room temperature, single crystals of $PbCo_{1/3}Nb_{2/3}O_3$ (PCN) have a cubic symmetry with lattice parameter of 4.04 Åand space group $Pm3m$ [50, 88]. It is seen that the Pb^{2+} ions are shifted by ∼0.3 Åfrom their (0, 0, 0) positions as in PFW [89], an observation generic to other Pb-containing complex perovskites.

$PbCo_{1/3}Nb_{2/3}O_3$ undergoes a diffuse phase transition (DPT) into a relaxor state with a broad and frequency dependent maximum around T = 250 K [50, 88, 89] in real component of the dielectric permitivity. It is generally observed that disorder is a key ingredient for exhibiting relaxor properties in Pb-containing complex perovskites. Also, the absence of any superlattice reflections in x-ray data supports that B-site (i.e. Co/Nb) in PCN is disordered.

On the magnetic part, there is nearly no information about the ordering of Co^{2+} ions except for one report suggesting an antiferromagnetic phase transition at 130 K [90]. However, there is no data on the temperature dependence of magnetic susceptibility. Consequently, there is no clear understanding of the number and types of magnetic ordering that PCN undergoes. Therefore, our goal is to first measure the bulk magnetic properties of PCN which will allow us to decipher its ground state. As PCN is a disordered material, evolution of local field is probed with μ^+SR spectroscopy which has high sensitivity to magnetic environment. Similar to PFN and PFT , ceramic and single crystal samples of PCN are studied in order to eliminate metallurgy related problems in identifying magnetic transitions.

5.6 Experimental details

The ceramic and single crystal sample of PCN are prepared in a same manner as PFN samples as described in Sec. 3.2. Bulk magnetization of PCN is carried out on powder and mosaic spread of single crystals of PCN using VSM on PPMS. The measurement covered temperature range of 2–300 K.

The μ^+SR spectra of PCN are obtained on ceramic pellet and mosaic spread of

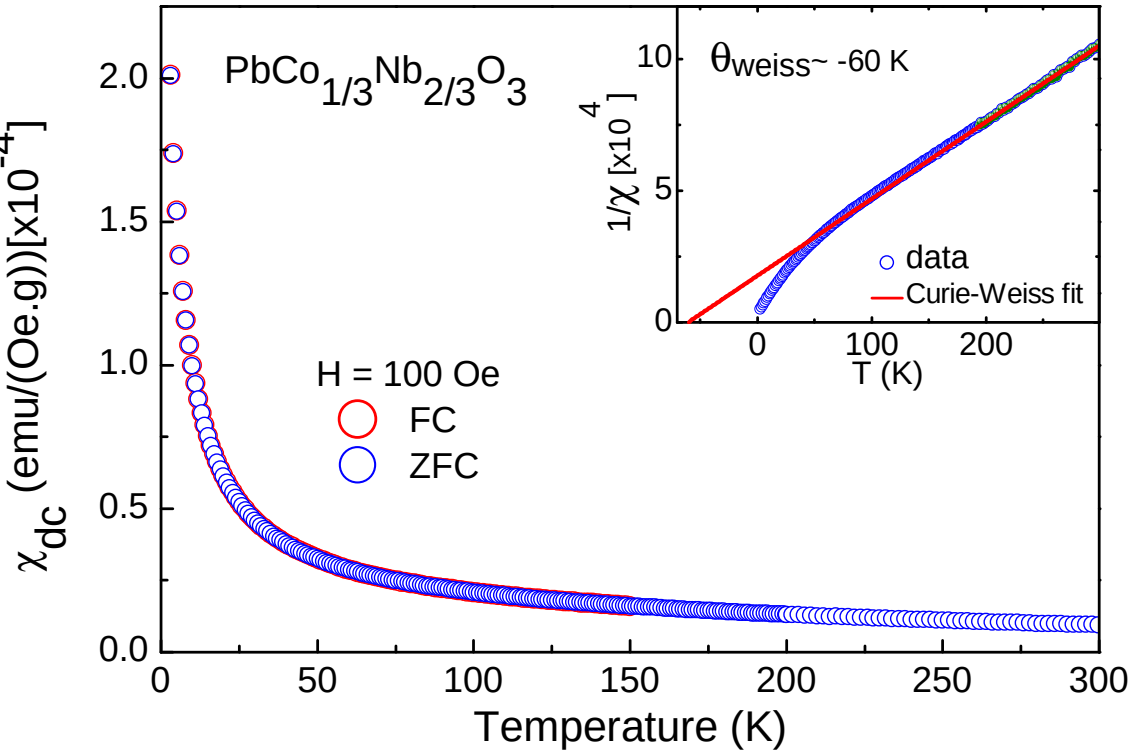

Figure 5.7: Magnetization of single crystals of PCN as a function of temperature between 300–2 K in a field of 100 Oe using ZFC and FC protocols.

single crystal samples separately. In both cases the sample was placed in a very thin Al-coated Mylar tape envelope and then attached to a low-background fork-type sample holder. In order to make certain that the muons stopped primarily inside the sample, we ensured that the side facing the muon beam-line was only covered by a single layer of Mylar tape. A muon veto counter was used for the single crystalline sample case. Subsequently, μ^+SR spectra were measured at the Swiss Muon Source (SμS), Paul Scherrer Institut, Villigen, Switzerland. By using the surface muon beamline πM3.2, longitudinal-field (LF) and zero-field (ZF) spectra were collected at the General Purpose Spectrometer (GPS). The Low Temperature Facility (LTF) is used for obtaining spectra at temperatures as low as 20 mK. In this case, powder sample was placed on silver plate which gives a constant background.

5.7 Results

5.7.1 Bulk magnetization

The *dc* susceptibility of PCN measured in ZFC and FC (shown in Fig. 5.7) does not show any anomalies between 2–300 K. Instead, both the curves follow a paramagnetic behavior without any signature of either an antiferromagnetic or spin glass transition contradicting with the earlier report of antiferromagnetic phase transition at ∼130 K [90]. For T>200 K, χ_{dc} can be nicely fitted with the Curie-Weiss law

$$\chi_{dc} = \frac{C}{T - \theta_{weiss}}.$$

The fit leads to θ_{weiss}∼-60 K, a value much smaller compared to the previously reported, -130 K [90]. Identical result is observed in the χ_{dc} measurements of powder samples ruling out the evidence of any anomalies related to magnetic order. However, at this point the absence of signs of magnetic transition in PCN are unclear. Especially because even though the concentration of magnetic Co^{2+} is low, it exceeds the percolation threshold required to form long-range magnetic order for a site disordered cubic system [91]. The percolation threshold refers to the minimum concentration of magnetic ions in a non-magnetic matrix below which the individual moments do not correlate with each other to form a long-range order. Therefore, the absence of anomalies in χ_{dc} may be explained due to either the transition being at lower temperature than 2 K or the presence of high degree of disorder at B-site resulting in very subtle anomalies which go undetected with bulk methods. These results therefore necessitate probing magnetic properties with highly sensitive, local technique at low temperatures.

The μ^+SR technique has been established as a unique and powerful method to study local magnetic fields and spin ordering in a wide range of materials [92–94]. By implanting highly spin polarized muons ($S = \frac{1}{2}$) into a compound and monitoring the angular and temporal decay into positrons, the muons act as a unique and highly *localized* magnetic probe.

5.7.2 μ^+SR study

The μSR signal for PCN is obtained in zero-field environment in both ceramic and mosaic single crystal samples. All the measured spectra, shown in Fig. 5.8 for powder sample demonstrate a clear absence of oscillations in the asymmetry function ruling out any direct evidence of a static long-range magnetic order in the sample. Instead, the muon polarization shows a slow exponential-like decay in the whole temperature range from 200 K down to 20 mK, whose damping rate gradually changes with temperature. This observation is reminiscent of the temperature evolution of the relaxation time in spin glasses close to T_{SG} [95] below which, the spin degrees of freedom freeze and a static polarization function similar to that of Kubo-Tayabe (in Sec. 2.3) is observed with a dip at short time scales. Therefore, the ZF spectra in PCN are fitted consistently with the following polarization function (Eq. 5.1) to extract the relaxation time.

$$A(t) = A_0 P_{\mathrm{ZF}}(t) = A_0 exp\left[(-\lambda t)^{\beta}\right] + A_{bkgr}\ , \tag{5.1}$$

where $\lambda = \frac{1}{\tau}$ is the relaxation rate, β is the measure of deviation from exponential decay (β=1). In the case of $\beta < 1$, the decay signifies a distribution of spin relaxation rates λ. A_{bkgr} is the constant non-relaxing background.

This function is generally used for disordered systems when the signal exhibits a strong relaxation due to the static or dynamic fluctuations whose distribution is unknown. The equation enables the extraction of relaxation rate and the parameter β. It is widely used to fit the depolarization spectra of spin glasses to describe the presence of many independent relaxation channels [96]. For spin glass systems β in Eq. 5.1 is understood as originating from a distribution of relaxation times. In systems

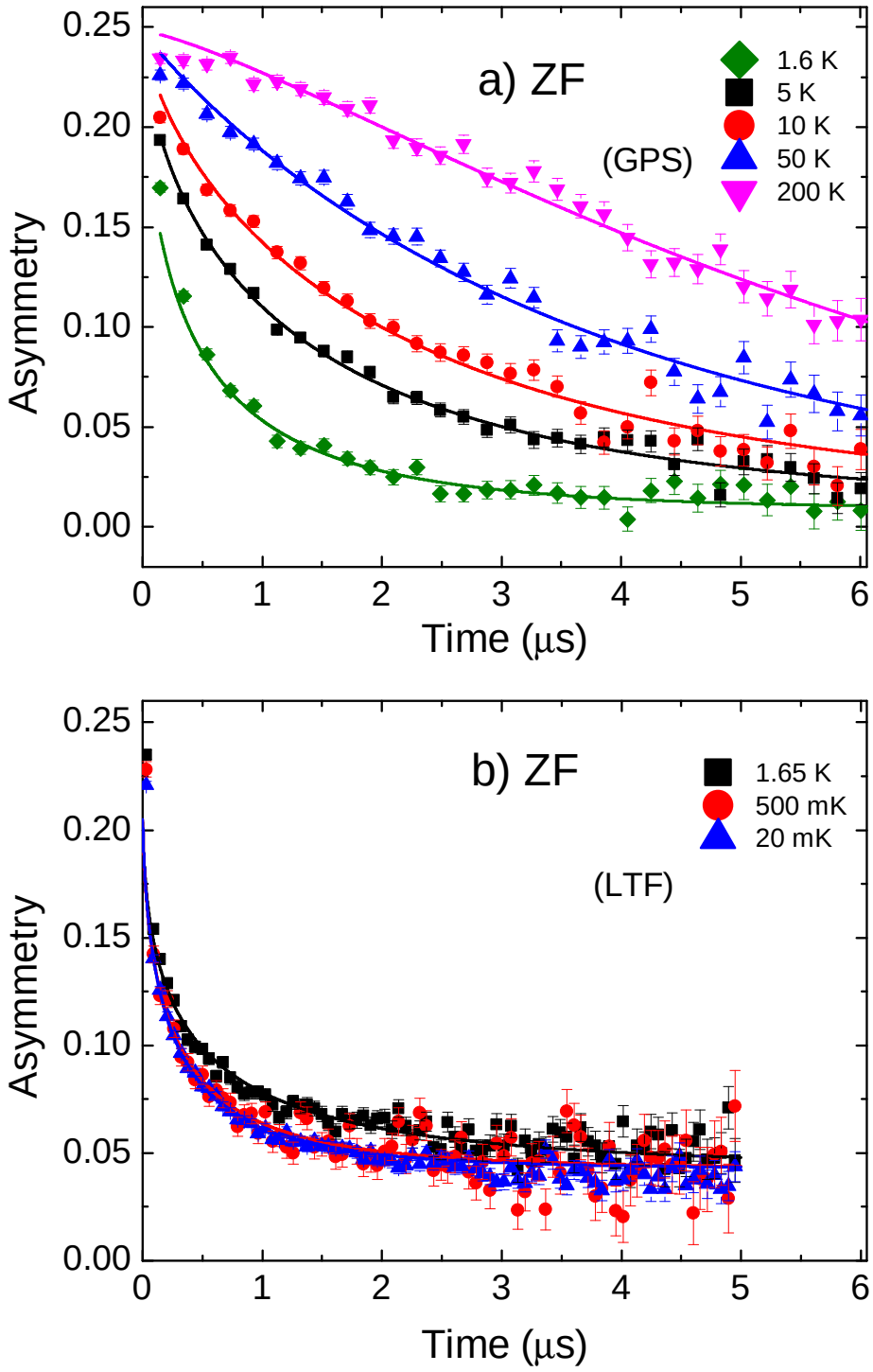

Figure 5.8: Zero-field (ZF) spectra of PCN collected for powder sample. The two panels a), b) show representative spectra obtained form GPS, LTF stations respectively.

like Ag-Mn, $\beta \rightarrow \frac{1}{3}$ for T$\rightarrow$T$_{SG}$ whereas the depolarization rate λ rapidly increases and reaches a maximum at T$_{SG}$. Below T$_{SG}$, β remains $\frac{1}{3}$ and λ gradually decreases towards lower temperatures.

Temperature dependent analysis of the μSR signal in PCN is obtained by a global fit to the Eq. 5.1 to extract the parameters λ and β. The relaxation rate λ, shown in Fig. 5.9a displays a typical critical behavior at lower temperature indicating that the dynamics of the spins are gradually slowing down. Also, the power exponent (β) shows a clear temperature dependence as it steadily decreases from $\beta \approx 1$ below $T = 100$ K. The non-exponential nature of the spectra above this temperature results in unphysical $\beta > 1$. In the vicinity of $T = 1.6$ K, the power *almost* seems to approach $\beta = 1/3$, corresponding to a near spin-glass state [96]. However, the low temperature data (from LTF) show that it clearly is not the case. Finally, it is worth noticing that in all our recorded data, the PCN compound never displays a Kubo-Toyabe behavior (arising due to the field distribution from static nuclear moments). This indicates the persistence of dynamic spin correlations even at temperature as high as $T = 200$ K.

If the system has static or dynamic fluctuations in the local fields, it is possible that the oscillatory part is killed despite the presence of magnetic ordering. It is possible to detect nature of these fluctuations by applying an external field in the direction of initial muon polarization. In the case of static local field fluctuations, application of an external magnetic field in the direction of muon spin gradually reduces the depolarization rate of the μ^+SR signal as the magnitude of the field is increased. It is possible to completely decouple the muon spin from the sample's magnetic environment when the external magnetic field is higher than the static internal field. In this case, the μ^+SR signal completely looses depolarization. However, if the system has dynamics due to fast fluctuating local fields the muon depolarization does not depend on applied field.

Fig. 5.10 represents the spectra measured in PCN in the presence of a longitudinal magnetic field at T = 20 mK, 1.6 K. At both the temperatures the relaxation rate of the signal shows very weak field dependence upto $\sim$5 kG which is an order higher than the decoupling field observed in typical spin glass systems [97, 98]. At very high magnetic fields (20 kOe) the relaxation becomes much slower although, it never completely looses the depolarization as is the case for system with static moments. This behavior is very similar to the dependence of longitudinal field μSR signal in Ag-Mn spin glass above T$_{SG}$ where dynamic fluctuations become very slow [98].Therefore, we can conclude that the spin correlations in PCN are dynamic in nature and they become very slow at low temperatures meaning that the magnetic correlations enhance.

5.8 Summary

The magnetic properties of PCN are remarkably different from the 'Fe' containing systems of this study i.e, the bulk magnetization and μ^+SR data clearly conclude that a static long-range magnetic order is absent in this system down to 20 mK. Further, μ^+SR data also indicates that there is no short-range ordering (like in spin glass) down to 20 mK. Therefore, although the absence of magnetic order in $PbCo_{1/3}Nb_{2/3}O_3$ remains ambiguous (despite the magnetic concentration being higher than the percolation threshold of 31% for a site disordered cubic system), we can conclude that the magnetic ground state of this system is neither AFSG nor SG. However, the slow relaxation of

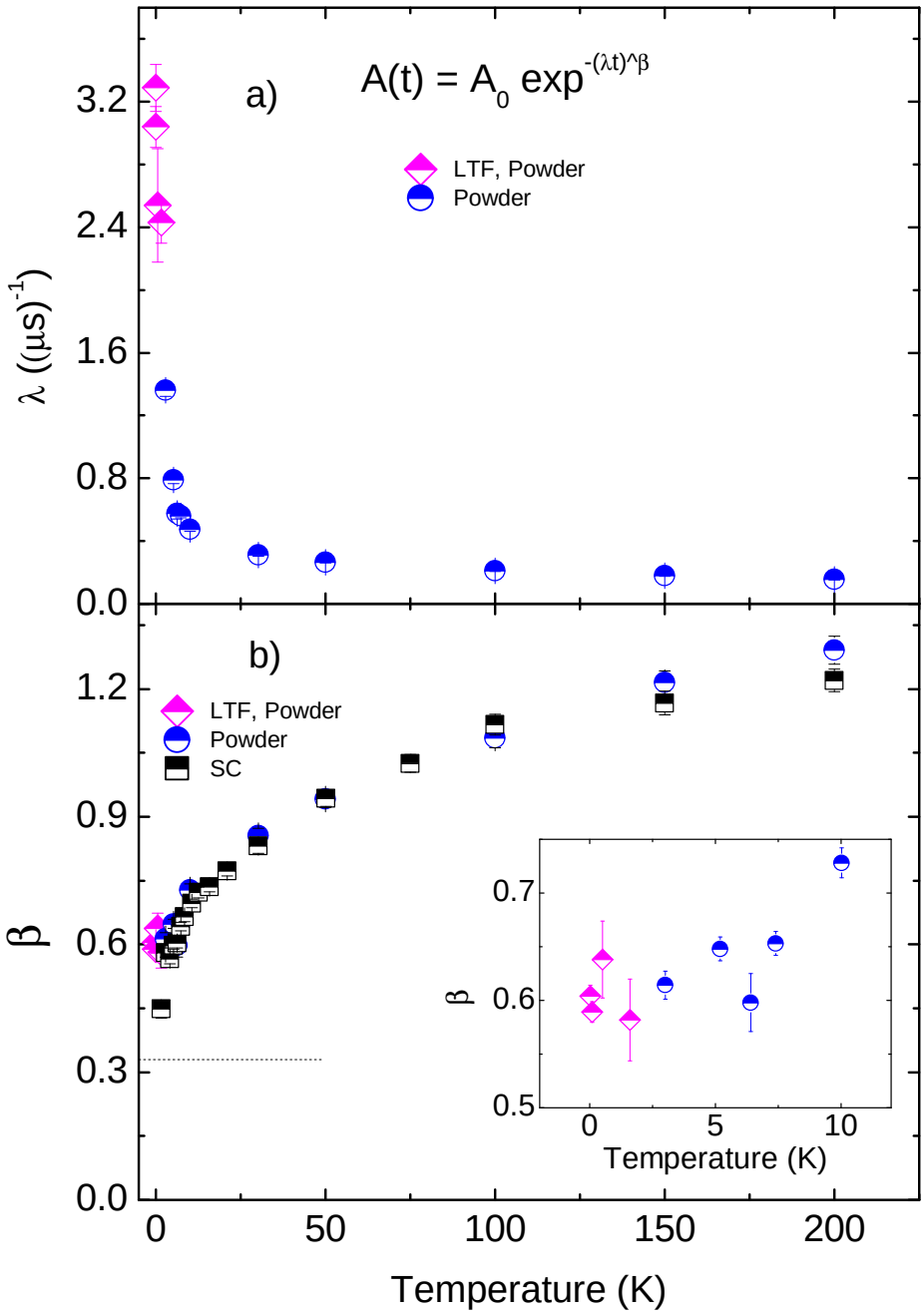

Figure 5.9: Temperature dependence of a) the relaxation rate (λ) and b) power exponent (β) for both single crystal (SC) and powder samples. (Here LTF refers to low temperature facility at SMuS PSI. Rest of the data are obtained at GPS.)

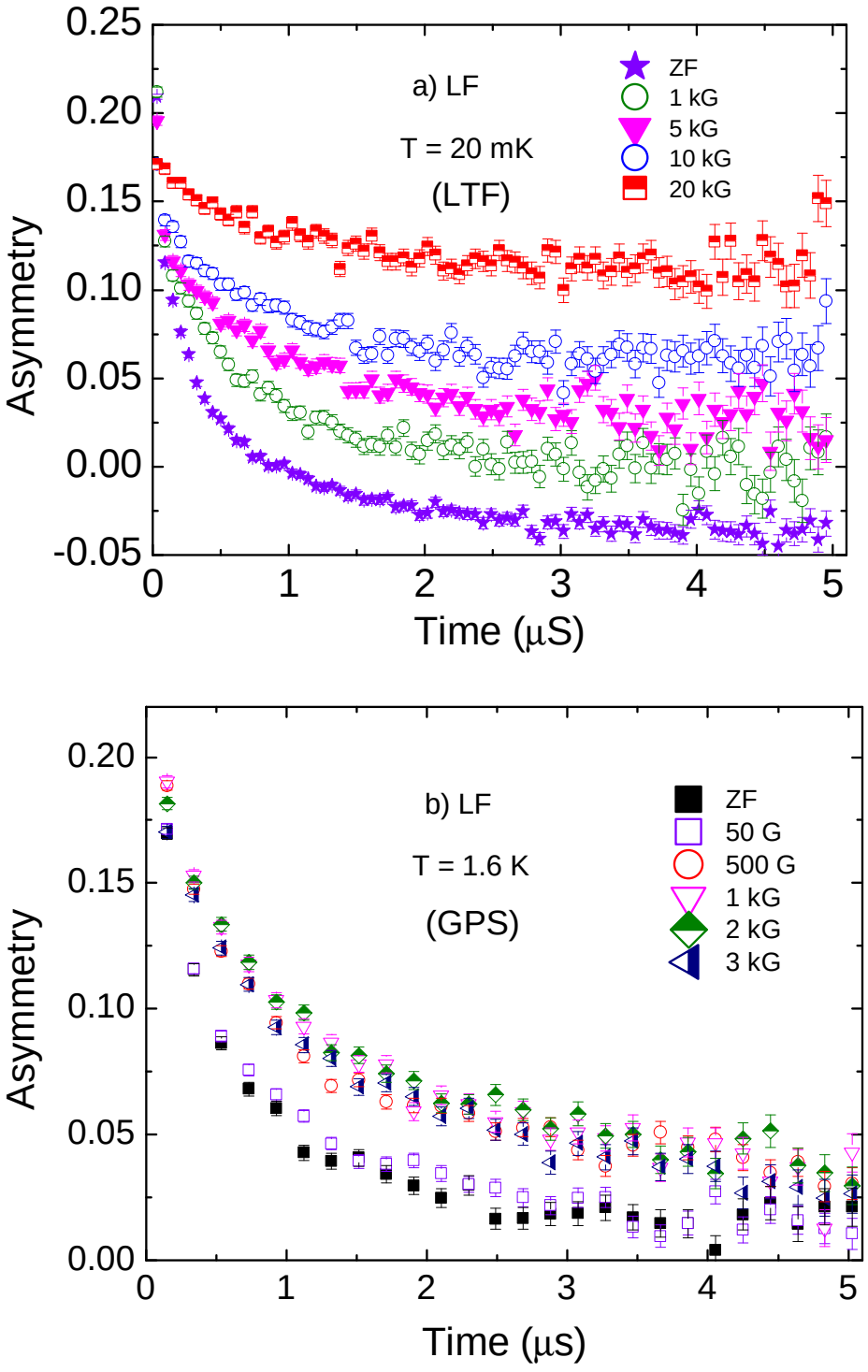

Figure 5.10: Muon depolarization spectra of PCN in the presence of an external magnetic field applied in the direction of initial muon polarization at a) 20 mK, b) 1.6 K respectively.

the zero-field spectra together with longitudinal field dependence strongly hint towards increasing magnetic correlations at low temperatures.

Chapter 6

Conclusion and Outlook

Infinite-range mean field theory for disordered spin systems predicts either a spin glass ground state or one involving a coexistence of long-range magnetic order with spin glass depending on the degree of frustration. More realistic models based on short-range interactions also reproduce these ground states through numerical simulations. On the experimental side, the presence of a spin glass state has been unambiguously confirmed in both Ising, Heisenberg systems and is observed in a variety of compounds such as metallic alloys, insulators and amorphous materials. The situation is less clear for the ground state of coexisting long-range magnetic order and spin glass. A major reason for this is the occurrence of phase separation, often observed in disordered systems with non-stoichiometric dilution. All the systems in which LRO-SG is reported so far, for example amorphous ferromagnets Au-Fe, Ni-Mn, Zr-Fe alloys, crystalline antiferromagnets such as $Fe_{0.6}Mn_{0.4}TiO_3$, $Co_2(OH)PO_4$, $Fe_{0.55}Mg_{0.45}Cl_2$ suffer uncertainties in chemical homogeneity. Therefore, a comprehensive understanding of this ground state i.e, the necessary magnetic interactions and the critical phenomena associated with the transition, is lacking. In this context, the present work is aimed to realize an unambiguous experimental proof of a coexisting LRO-SG system. For this purpose, Pb-based perovskites were considered for this study having stoichiometric dilutions of chemical disorder at the magnetic site preventing metallurgy related problems.

$PbFe_{1/2}Nb_{1/2}O_3$ belongs to the family of disordered perovskites with chemical disorder at Fe^{3+}/Nb^{5+} ions. The system undergoes an antiferromagnetic transition at T_N=143 K and a spin glass transition at T_{SG}=12 K. Therefore, $PbFe_{1/2}Nb_{1/2}O_3$ is a potential candidate to look for AFSG state. Present work probes the magnetic ground state of this material using a combination of bulk and local techniques, viz., magnetometry, neutron scattering and Mössbauer spectroscopy. While bulk magnetization reproduces the Néel transition and spin glass transition in the crystalline sample, neutron scattering confirms that the Bragg peak corresponding to long-range AF order persists into the SG state. Further, a reduction is observed in the intensity of this Bragg peak below $\sim$ 50 K indicating that the spins of ordered collinear AF structure undergo canting. Previous neutron scattering experiments observe a contribution from magnetic diffuse scattering under the AF Bragg peak indicating the presence of magnetic short-range correlations in the system [61]. These short-range correlations are enhanced below $\sim$ 50 K. On the local scale, this is reflected in the slowing down of dynamic fluctuations in the hyperfine field at ^{57}Fe nuclei resulting in its rapid growth.

Below T_{SG} the fluctuations freeze and the hyperfine field ultimately reaches a saturation moment at the base temperature. Therefore, these results conclude that the crystalline Heisenberg system $PbFe_{1/2}Nb_{1/2}O_3$ realizes a unique coexistence of long-range AF and short-range SG in the ground state [72]. This coexistence can be described by a speromagnet-like spin-arrangement considering randomly tilted frozen transverse components giving rise to SG and a mean AF on longitudinal components. Further, the transition temperature T_{SG} into AFSG state is studied by application of external magnetic field and hydrostatic pressure. The H-T phase diagram confirms that MFT is not a suitable model to describe the AFSG state in PFN .

In order to understand the conditions for the appearance of this exotic AFSG state, the magnetic properties of a series of compounds belonging to the $PbFe_{1/2}Nb_{1/2}O_3$ family are studied. First is $PbFe_{1/2}Ta_{1/2}O_3$, a system with fully substituted non-magnetic ion in PFN . The bulk magnetization reveals that magnetic properties of PFT are identical to those of PFN [99] i.e, PFT undergoes two magnetic phase transitions: AF at T_N ∼153 K and SG at T_{SG} ∼10 K. Neutron scattering clearly proves the presence of long-range AF order below T_{SG}. Further, these experiments reveal magnetic short-range correlations in PFT which rapidly strengthen below ∼ 50 K as T_{SG} is approached. The characteristic length of the correlations is found to be 10 ±2 $\AA$ and corresponds to nearly two lattice constants. This suggest that the magnetic interactions beyond first nearest-neighbor are important for magnetism of PFT . A similar analysis of the diffuse scattering observed in PFN [61] also leads to ∼10 $\AA$ correlation length, twice the size of its lattice parameter.

Similarly the Mössbauer spectra and its temperature evolution of PFT and PFN are identical. The spectra indicate dynamic fluctuations in magnetic hyperfine field which slow down as T_{SG} is approached. The fluctuations nearly vanish at the base temperature and hyperfine field reaches its saturation value indicating the magnetic ground state. Therefore a uniform coexistence of AF and SG is concluded at the ground state of PFT which can be described by the same speromagnet-like spin arrangement as in Fig. 3.10.

Much of the earlier research to probe the coexistence phase revealed that the simultaneous presence of long-range order and spin glass are restricted to a specific magnetic ion concentration range. For example, the Ising $FeCl_2$ shows AFSG state only for the dilution of Fe site with nearly 50% of Mg. However, in Au-Fe the FMSG state appears over a range of Fe concentrations.The present work shows that the AFSG state of PFN is retained if the ratio of magnetic to non-magnetic ion is kept constant i.e, in PFT . To find the effect of magnetic ion concentration on AFSG, magnetic properties of PFW and PCN are studied. The two materials have 0.67:0.33, 0.33:0.67 ratio of magnetic to non-magnetic ions respectively compared to 50:50 in PFN and PFT .

Bulk magnetization of PFW reveals three anomalies in ZFC susceptibility: T_N= 350 K, T_{an}= 7 K and T_m= 170 K. The position of T_{an} in *ac* susceptibility does not exhibit frequency dependence and hence the transition into spin glass is ruled out. Although neutron diffraction confirms that the antiferromagnetic Bragg peak at propagation vector $\boldsymbol{Q} = (\frac{1}{2}, \frac{1}{2}, \frac{1}{2})$ survives dow to 1.5 K. However, the history dependence of magnetization in the entire temperature, the anomaly at T_m= 170 K and the presence of a nearly constant hysteresis loops in M-H loops indicate the presence of a ferromagnetic contribution to the sample. The absence of a corresponding magnetic

Bragg peaks or the sextet due to ferromagnetic order in Mössbauer spectra indicate that the contribution is due to a ferromagnetic impurity in the sample. In this situation, we can conclude that the ground state of $PbFe_{2/3}W_{1/3}O_3$ is not an AFSG. Although, the magnetic properties of PFW are not entirely reliable due to the ferromagnetic contamination of the sample.

The results of PCN are surprisingly different from the above three compounds. Bulk magnetization of the compound shows paramagnetic behavior all the way down to 2 K without any significant anomalies corresponding to magnetic transitions. Although μ^+SR spectroscopy reveals enhancing magnetic correlations at low temperatures, the absence of any long-range or short-range magnetic order is confirmed down to 20 mK. Therefore, we can conclude that the magnetic ground state of PCN is not an AFSG.

In summary, by comparing the magnetic properties of the four compounds we can establish that the nature of the magnetic phases and specifically the microscopic coexistence of long range AF and orientational SG order are a common feature of stoichiometric disordered $PbFe_{1/2}B_{1/2}O_3$ (B = Fe, Ta) perovskites. We find that as long as the dilution is isovalent, the non-magnetic ions do not produce a strong effect on the magnetic phase transitions in this family. However, significant deviations are observed in the magnetic properties when the concentration and/or type of magnetic ion differs from that of 50% Fe^{3+}.

Overall, the work succeeded in identifying a disordered system whose magnetic ground state is a coexistence of spin glass and magnetic long order. The combination of bulk magnetization, neutron scattering, and Mössbauer spectroscopy unambiguously prove that the ground state of PFN and PFT is a homogeneous coexistence of antiferromagnet and spin glass. By comparing temperature evolutions of magnetic short range correlations, hyperfine fields and AF Bragg peak intensity, a microscopic model is proposed for the AFSG state. Both the systems contain Fe^{3+} as magnetic ions which are spin-only ions. Therefore, spin orbit coupling that can lead to magnetic anisotropy is non-significant for this magnetic ion. Secondly, the magnetic diffuse scattering is symmetrically distributed under the AF Bragg peak indicating that the system is Heisenberg-like. However, the vector or Ising nature of spins forming AFSG is best probed by directly measuring the magnetic exchange constants in the system. As mentioned in the Appendix. A.1, A.2 the spin wave dispersion, through which the magnetic interactions are extracted, could not be directly obtained in PFN and PFT . The corresponding inelastic scans do not reveal any feature referring to excitation peaks in the system. Similar spectra are also reported for PFN in Ref. [100]. It is known that disorder in magnetic systems tends to over damp magnetic excitations and hence may not be very well defined in the inelastic scans, for example as in disordered $Mn_{0.3}Zn_{0.7}F_2$ [101]. In this case, analysis of the spectrum was carried out with reference to the parent compound MnF_2 and calculating the excitation frequencies using coherent potential approximation (CPA). Similar approach was also successful in regenerating the excitation spectra of disordered $RbMn_{0.54}Mg_{0.46}F_4$ antiferromagnet [102]. Therefore, as a next step, the excitation spectra of PFN may be calculated by considering one of the several computational techniques.

Although, the magnetic exchange interactions in PFN , PFT are not completely identified, neutron scattering results confirm that the range of interactions extend at least up to next nearest neighbor. If these interactions are frustrated, as in many spin

glass systems, application of hydrostatic pressure will strongly effect the magnetic state of the system. For example, in pyrochlore $(Tb_{1-x}La_x)_2Mo_2O_7$ long-range ferromagnetic order is destroyed by the application of pressure and a ground state, spin glass is achieved [103]. In PFN , AF ordering temperature is reported to increase by 10 K for an applied pressure of 6.5 GPa [104]. In the current study, we observe that the glass transition temperature T_{SG} (into AFSG) in Sec. 3.5.2 increases by 20% upon applying a pressure of 0.23 GPa without any drastic change in the spectra. However, by applying sufficiently high magnitude of pressure one may be able to access new magnetic ground state in these disordered materials.

Appendices

Appendix A

Inelastic neutron scattering

A.1 $PbFe_{1/2}Nb_{1/2}O_3$

Inelastic scattering in PFN is measured at the PUMA triple axis spectrometer (FRM II, Germany). A high quality single crystal of 4x4x4 mm^3 dimensions was aligned in $< hh0 > / < 00l >$ scattering plane in cubic notation. This allowed us to reach three magnetic Bragg peaks, $\mathbf{Q}_{AF} = (\frac{1}{2}, \frac{1}{2}, \frac{1}{2})$, $(\frac{1}{2}, \frac{1}{2}, \frac{3}{2})$, $(\frac{3}{2}, \frac{3}{2}, \frac{1}{2})$. Inelastic scans are measured in these three Brillouin zones as functions of momentum and energy transfer at constant energy and momentum transfer respectively. All the neutron data were collected with $k_f = 2.662$ $\mathring{A}^{-1}$ and a collimation of *open-60′-sample-60′-open′*.

The representative inelastic spectra measured as a function of energy at $\boldsymbol{Q}$=(0.5, 0.5, 1.45), (0.55, 0.55, 1.55) and (0.55, 0.55, 1.5) at 20 K, shown in Fig. A.1, do not directly reveal the presence of any sharp excitation in the system. We observe that the magnetic dynamic scattering is over-damped in the measured three symmetric directions at all temperatures similar to the observations reported by Stock *et.al.* [100].

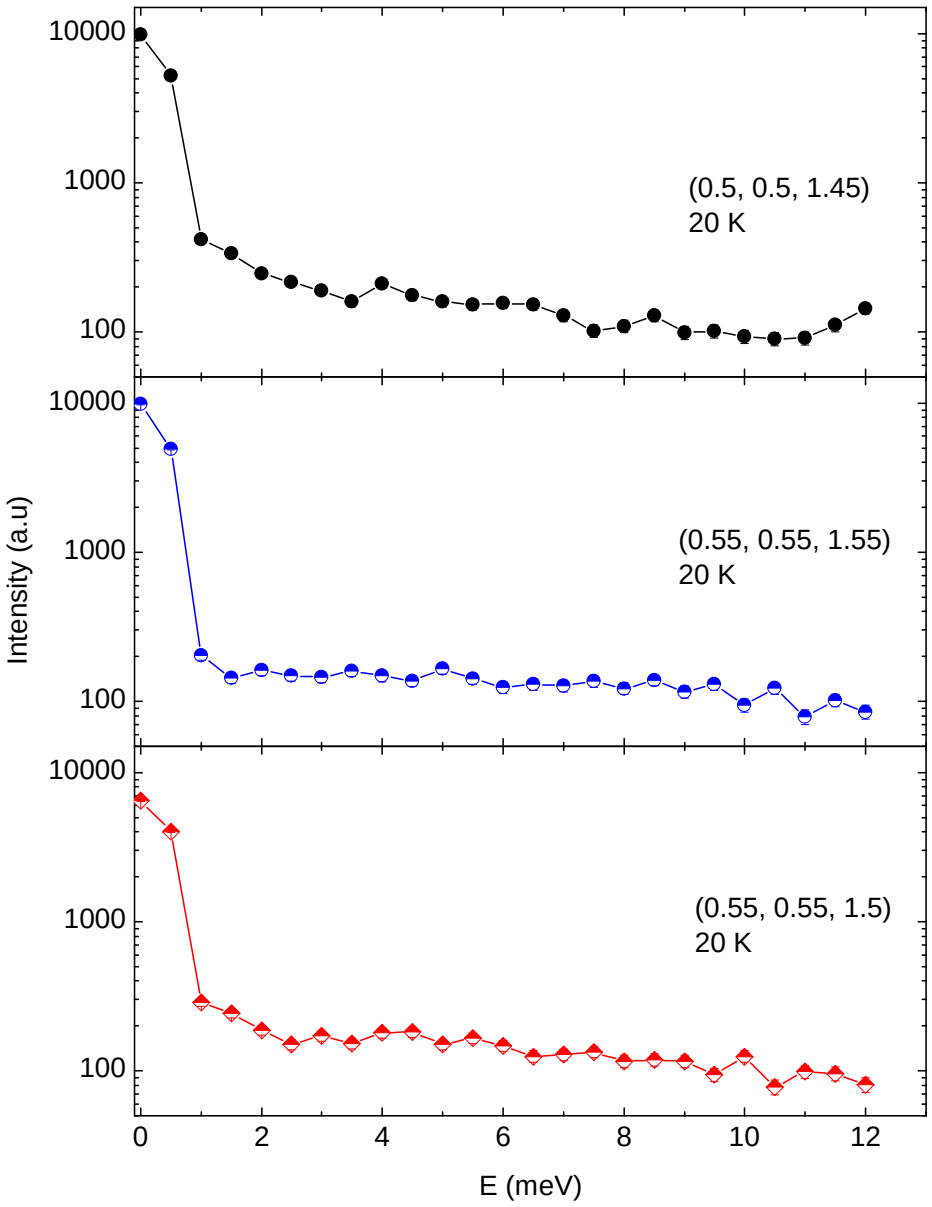

Figure A.1: The constant-$\boldsymbol{k}$ scans measured at $\mathbf{Q}_{AF} = (\frac{1}{2}, \frac{1}{2}, \frac{3}{2})$ with offsets along $< 001 >$, $< 111 >$ and $< 110 >$ directions at 20 K in $PbFe_{1/2}Nb_{1/2}O_3$.

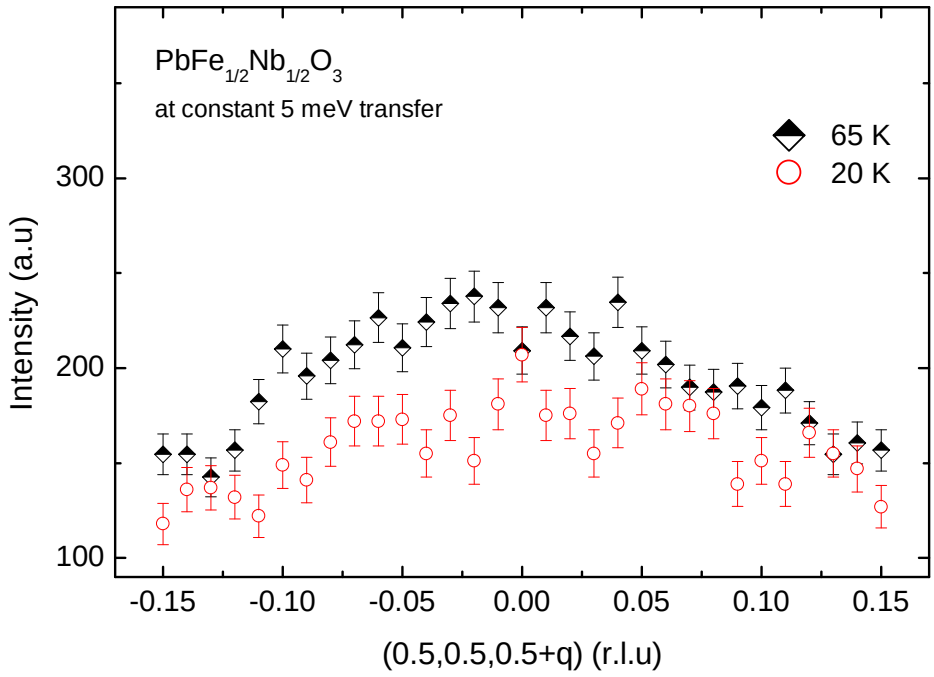

Figure A.2: Inelastic scans measured along $< 001 >$ direction from $\boldsymbol{Q}_{AF} = (0.5, 0.5, 0.5)$ for constant energy transfer of 5 meV at several temperatures.

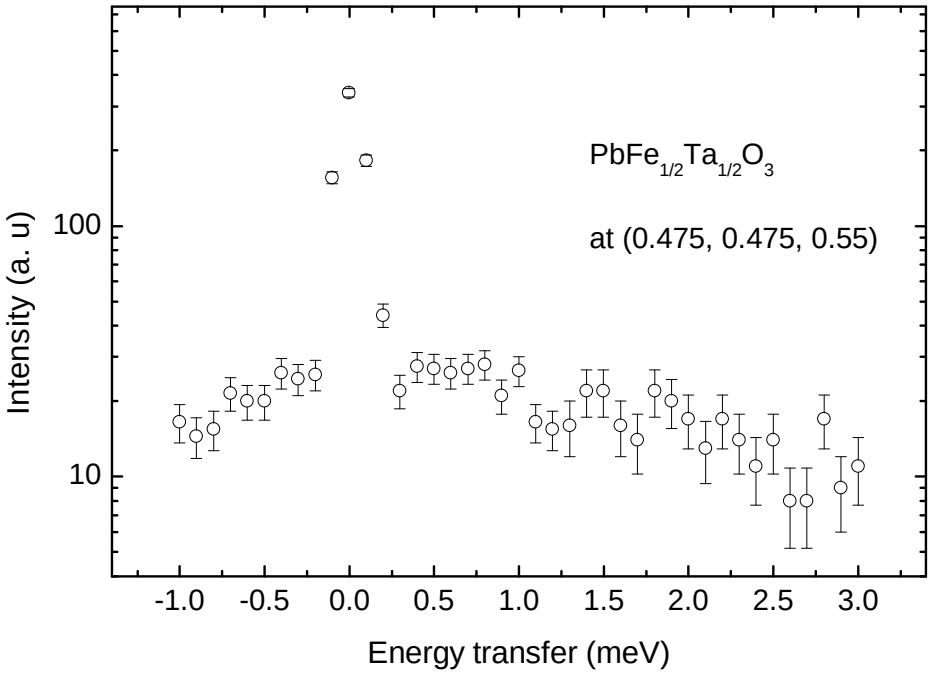

Figure A.3: Inelastic scans measured at constant $\boldsymbol{Q}$=(0.475, 0.475, 0.55) in PFT as a function of energy transfer at 70 K.

A.2 $PbFe_{1/2}Ta_{1/2}O_3$

Inelastic scattering in PFT at the magnetic Bragg peak is measured using the triple axis spectrometer TASP in the same configuration as in Sec. 4 for unpolarized neutron scattering. The neutron data were collected using $k_f = 1.55$ $\AA^{-1}$ and a collimation of *open-80′-sample-80′-80′*. A liquid nitrogen cooled Be-filter was used to suppress higher order contaminations.

Fig. A.3, A.4 show the inelastic scans as a function of momentum and energy transfer respectively revealing the similarity with spectra of PFN . The magnetic dynamic response in PFT also is over damped and hence no direct spin wave dispersion could be observed.

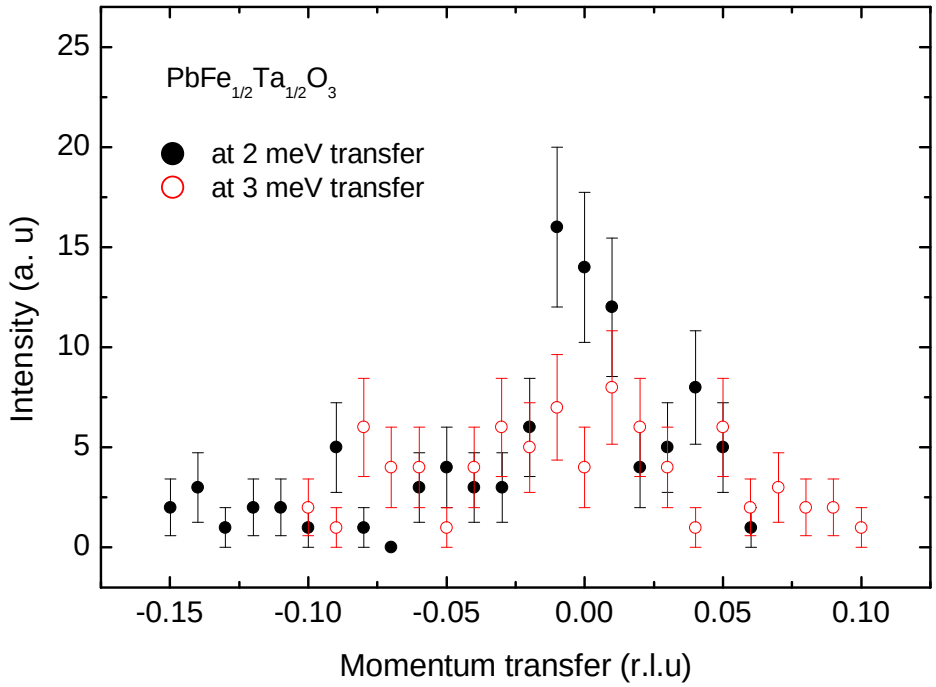

Figure A.4: Inelastic scans measured transverse to $\boldsymbol{Q}_{AF} = (0.5, 0.5, 0.5)$ in PFT for constant energy transfer at 70 K as a function of momentum transfer.

Appendix B

Resolution calculation for a triple-axis spectrometer

In a triple axis experiment, scattering is measured at a specific momentum transfer $\mathbf{k}$ in the Brillouin zone and energy transfer ω. However,due to the finite mosaicities of the single crystals used for monochromator, analyzer and the sample itself, the scattering does not occur at one point but in a volume centered at ($\mathbf{k}$, ω). Therefore, the scattered neutron is detected at ($\mathbf{k}$+$\Delta\mathbf{k}$, ω+$\Delta\omega$) with a probability given by function R($\Delta\mathbf{k}$, $\Delta\omega$), known as the resolution of the spectrometer. Hence, the measured scattered intensity is a convolution of sample's scattering function $S(\mathbf{k},\omega)$ and resolution function of the spectrometer so that the differential scattering cross section is written as:

$$\frac{d^2\sigma}{d\Omega dE_f} = \int R(\Delta\mathbf{k},\Delta\omega)S(\mathbf{k},\omega)d\omega d\mathbf{k}.$$

One can properly analyze a scattering data by calculating the resolution function for a given spectrometer configuration. As the integration is over four dimensions, the resolution function can be written in terms of a 4-vector ϱ and a 4×4 matrix $\mathbf{M}$ as following:

$$R(\Delta\mathbf{k},\Delta\omega) = R_0 e^{-\frac{1}{2}\Delta\varrho\mathbf{M}\Delta\varrho}.$$

where,

$$\varrho = (\varrho_0,\varrho_1,\varrho_2,\varrho_3) = \left(\frac{m\omega}{\hbar\mathbf{k}},\mathbf{k}_{||},\mathbf{k}_{\perp},\mathbf{k}_z\right).$$

$\mathbf{k}_{||}$, $\mathbf{k}_{\perp}$ are the parallel, perpendicular components of the scattering vector $\mathbf{k}$ and $\mathbf{k}_z$ is known as the vertical component and it points out of the scattering plane. This formulation reduces the calculation of resolution function to determining the resolution matrix $\mathbf{M}$. Two approximations are available for the calculation of $\mathbf{M}$: 1) Cooper-Nathan method [105] and, 2) Popovici method [106].

In Cooper-Nathan approximation, the inverse of the resolution matrix is given by:

$$\mathbf{M}^{-1} = BA(G + C^T F C)^{-1} A^T B^T.$$

Here, the matrix G relates to the beam divergences and collimators in the spectrometer, F to the mosaicities of monochromator and analyzer, A, B and C to the scattering angles of monochromator, analyzer and sample.

In the Popovici approximation, the effects of shapes and sizes of the source, monochromator, sample, analyzer and detectors are also considered in addition to the collimators and mosiaicities of the monochromator and analyzer crystals. This information is contained in the matrix S and the inverse of the reslution matrix $\mathbf{M}$ is represented by:

$$\mathbf{M}^{-1} = BA[\{D(S + T^T FT)^{-1} D^T\}^{-1} + G]^{-1} A^T B^T.$$

The matrices D and T include the terms containing distances involved in the spectrometer configuration, i.e, between monochromator and sample, sample and analyzer etc.

In the analysis of $PbFe_{1/2}Ta_{1/2}O_3$ data in Sec. 4.3.2, the Popovici approximation is used to calculate the resolution function of the spectrometer configuration using the MATLAB library *ResLib* [79].

Appendix C

Neutron powder diffraction from $PbFe_{2/3}W_{1/3}O_3$

The diffractions patterns (in Fig: 5.4) are consistently refined at all temperatures by considering: 1) cubic symmetry for the crystal structure, 2) Isotropic thermal factors for Pb^{2+}, Fe^{3+}/W^{6+} and anisotropic thermal factors for O^{2-} ions, 3) displacive disorder of Pb^{2+} ions around their actual (0, 0, 0) positions, 4) G-type magnetic structure for antiferromagnetic ordering below 350 K.

C.1 Reitveld refinement

The refinement approach for analyzing a diffraction pattern is based on the calculation of positions and intensities of Bragg peaks from all (hkl) planes from a starting model for the crystal structure. The intensities are appropriately adjusted for the experimental conditions. For example, the instrumental resolution, sample thickness, absorption coefficient, sample environment and so on. In particular, the observed shapes of Bragg peaks are generally Gaussian or Lorentzian or a combination of both and are defined by instrument resolution. The 2θ dependence of the FWHM of Gausian Bragg peak is given as follows based on instrument specific parameters U, V and W:

$$FWHM(2\theta) = \sqrt{Utan^2\theta + Vtan\theta + W}$$

A further broadening of the peaks is observed due to finite size and strain in the sample which is generally of Lorentzian form. In this case, the total peak shape is a convolution of Gaussian and Lorentzian functions. In some cases, the peaks are much broader than the FWHM defined by instrumental resolution which indicates a possible short-range order in the sample.

The calculated pattern at an angle 2θ can be written as follows:

$$I_{i,c} = I_{i,b} + \sum_{p,k} S_p I_{p,k} \Omega^p_{i,k}$$

Here, $I_{i,b}$ is the background, S_p is the scale factor for phase p, $\Omega^p_{i,k}$ is the profile function completely based on instrument parameters and

$$I_{p,k} = (L_k A_k P_k C_k |F_k|^2)_p$$

is the intensity of Bragg peak of phase p for k^{th} reflection where L_k, A_k, P_k and C_k are Lorenzian, absorption, preferred orientation and extinction correction respectively. F_k is the structure factor which defines the intensity and position of Bragg reflections as given in Sec. 2.1. The structure factor also takes thermally induced atomic vibrations into account which modifies the Bragg intensity with a factor $e^{-2(\boldsymbol{k}.\boldsymbol{u})^2}$ known as thermal factor where,

$$(\boldsymbol{k}.\boldsymbol{u})^2 = \sum_{m,n} \boldsymbol{k_m u_m k_n^T u_n^T} = \sum_{m,n} \boldsymbol{k_m u_m u_n^T k_n^T} = \sum_{m,n} \boldsymbol{k_m} \beta_{mn} \boldsymbol{k_n^T}.$$

Since the displacement $\boldsymbol{u}$, scattering vector $\boldsymbol{k}$ are vectors, the thermal factor results in a directional dependent tensorial quantity. For practical purposes, this is defined as

$$\beta = \begin{vmatrix} \beta_{11} & \beta_{12} & \beta_{13} \\ \beta_{21} & \beta_{22} & \beta_{23} \\ \beta_{31} & \beta_{32} & \beta_{33} \end{vmatrix}$$

in the refinement such that $\beta_{mn} = 2\pi^2 a *_m a *_n U_{mn}$ and U_{mn} is the mean square displacement of the the atom from its equillibrium position.

In the case of isotropic thermal motion this parameter $(\boldsymbol{k}.\boldsymbol{u})^2 = 8\pi^2 U_{iso} \frac{sin^2\theta}{\lambda^2}$ when $|\boldsymbol{k}| = 4\pi \frac{sin\theta}{\lambda}$.

Thus calculated pattern is then refined until a best fit is obatined between calculated and observed diffracted intensitiess. Reliability of the fit is described by the so called R-factors profile factor R_p, weighted profile factor R_{wp}, Bragg factor R_B and experimental factor R_{exp}. The most relevant factor that decides goodness of fit is the wighted profile factor given as below:

$$R_{wp} = 100 \left[\frac{\sum_i w_i (I_{obs,i} - I_{calc,i})^2}{w_i \sum_i I_{obs,i}^2} \right]^{1/2} = 100 \left[\frac{\chi^2}{w_i \sum_i I_{obs,i}^2} \right]^{1/2} \quad \text{(C.1)}$$

C.2 Structural analysis

A schematic of the refined cubic structure for PFW is shown in Fig. C.1. At room temperature, lattice parameter is found to be $a = 3.9986$ $\mathring{A}$ which is close to the value obtained from XRD ($a = 3.9805$ $\mathring{A}$). The lattice continuously shrinks while retaining the cubic structure as temperature is lowered (as shown in Fig. C.2) without any significant anomalies at either of the temperatures of interest. Therefore, we can conclude that within the measurement precision no structural phase transition is observed in PFW down to 1.5 K.

Best χ^2 is obtained by considering that the Pb ions are displaced from their original wyckoff-(0,0,0) positions. In the refinement model these displacements are considered along $< 110 >$ direction.Temperature dependence shows that amplitude of this displacement increases gradually below ~350 K (in Fig. C.3a). The observation is consistent with other Pb-based relaxor ferroelectrics like $PbMg_{1/3}Ta_{2/3}O_3$ [107], in contrast to the temperature independent displacements reported by [83]. In addition, Pb and

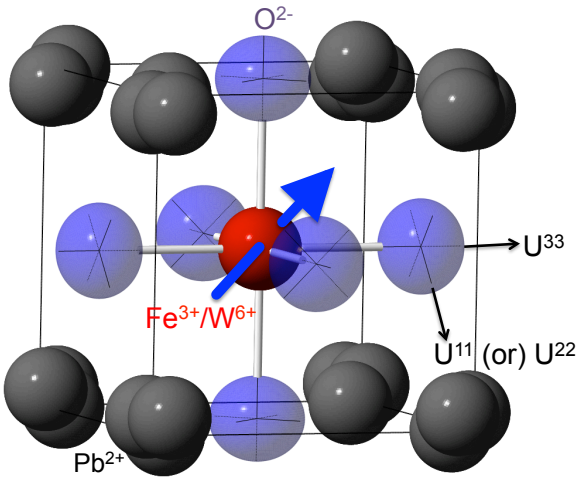

Figure C.1: Cubic structure of $PbFe_{2/3}W_{1/3}O_3$ showing the octahedral arrangement of Oxygen ions (blue ellipsoides) around Fe^{3+}/W^{6+} ions where U^{11}, U^{22} and U^{33} indicate the directions of anisotropic oxygen thermal parameters. Also, the displacement of Pb^{2+} in $< 110 >$ direction can be seen.

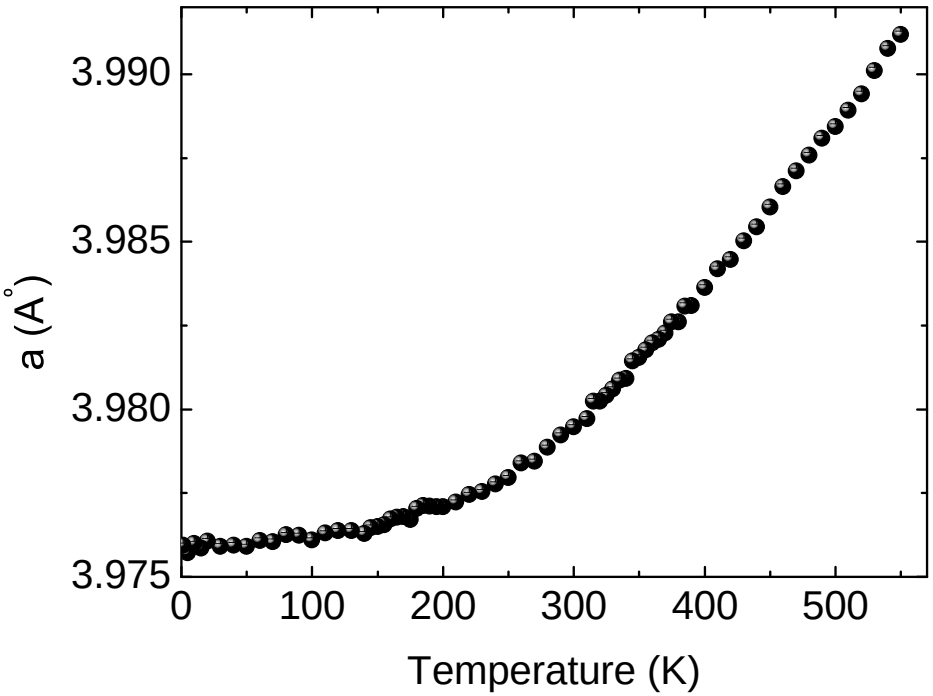

Figure C.2: Thermal expansion of the cubic lattice of PFW as observed through neutron powder diffraction.

Fe/W ions have an isotropic thermal factor defined as $B_{iso} = 8\pi^2 < u^2 >$ such that

$$U_{rms}^{iso} = \sqrt{< u^2 >} = \sqrt{\frac{B_{iso}}{8\pi^2}} \tag{C.2}$$

defines an equivalent displacement of the atom from its position. Fig. C.3b shows that U_{rms}^{iso} continuously decreases with decreasing temperature. However, the refinement results in Oxygen ion having anisotropic thermal factors with two components β_{11} and β_{33} of the tensor. While β_{11} (and β_{22}) are components in the face of the cube, β_{33} corresponds to component perpendicular to the face connecting to Fe/W ions as depicted in Fig. C.1. We observe that β_{11} decreases monotonically with temperature. However, an anomalous feature is observed in β_{33} ~200 K which is just above the transition into ferroelectric phase.

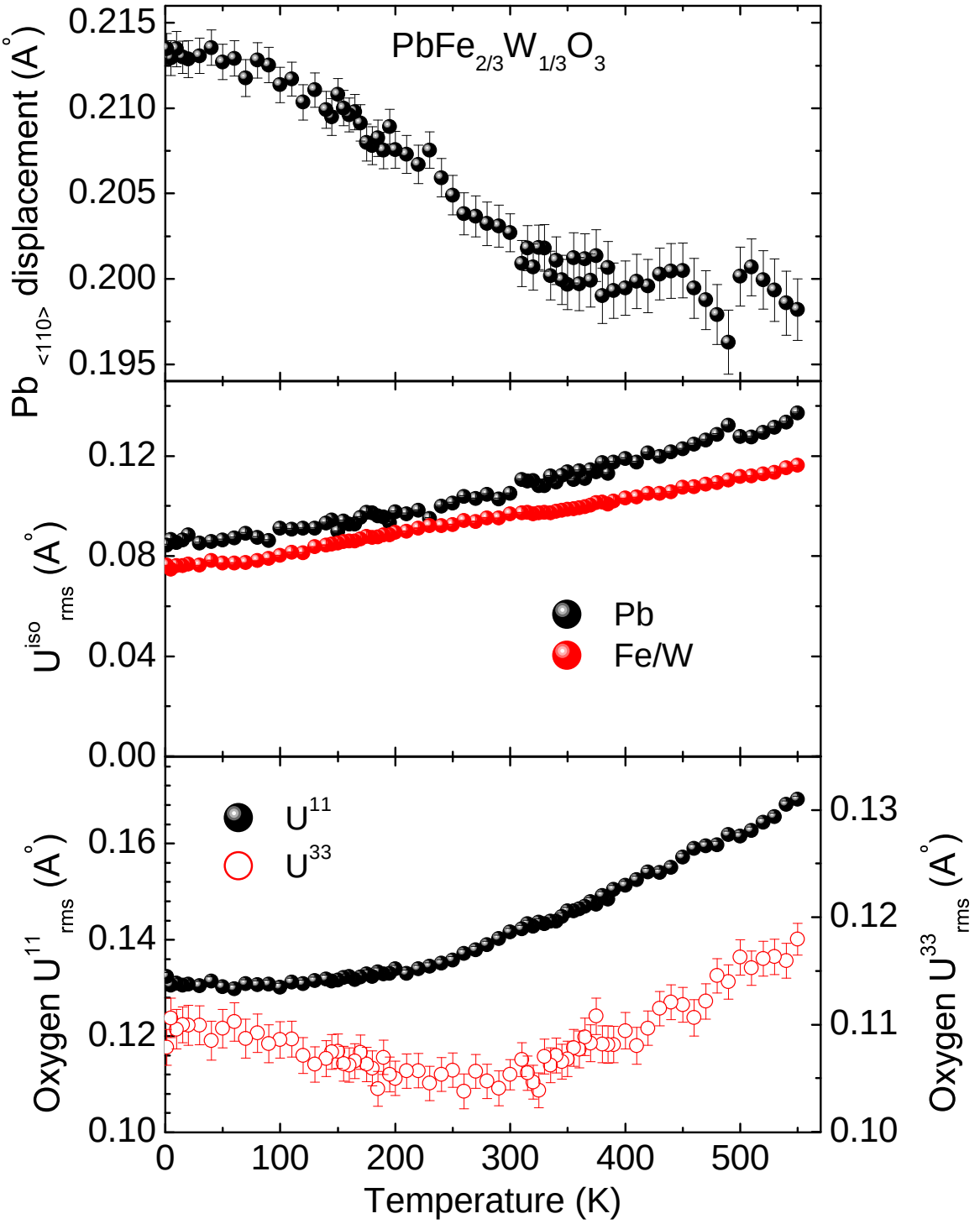

Figure C.3: Displacement of Pb^{2+} ions in cubic PFW lattice along $< 110 >$ direction, b) Isotropic thermal factor of Pb and Fe/W ions, c) U_{11} and U_{33} components of the anisotropic thermal factor tensor of Oxygen as a function of temperature.

List of Figures

Bibliography

[1] E. Dagotto, T. Hotta, and A. Moreo. Colossal magnetoresistant materials: the key role of phase separation. *Physics Reports*, 344:1 – 153, 2001.

[2] H. Maletta and W. Felsch. The non-metallic spin glass system (EuSr) S. *J. Phys. Colloques*, 39(C6):931–933, 1978.

[3] C. A. M. Mulder, A. J. van Duyneveldt, and J. A. Mydosh. Susceptibility of the CuMn spin-glass: Frequency and field dependences. *Phys. Rev. B*, 23:1384–1396, 1981.

[4] S. Nagata, P. H. Keesom, and H. R. Harrison. Low-dc-field susceptibility of CuMn spin glass. *Phys. Rev. B*, 19:1633–1638, 1979.

[5] R. Mathieu, M. Hudl, and P. Nordblad. Memory and rejuvenation in a spin glass. *EPL (Europhysics Letters)*, 90(6):67003, 2010.

[6] K. Binder and W. Kob. *Glassy Materials and Disordered Solids*. World Scientific, Singapore, 2011.

[7] David Sherrington and Scott Kirkpatrick. Solvable model of a spin-glass. *Phys. Rev. Lett.*, 35:1792–1796, 1975.

[8] G. Parisi. Infinite number of order parameters for spin-glasses. *Phys. Rev. Lett.*, 43:1754–1756, 1979.

[9] Marc Gabay and Gérard Toulouse. Coexistence of spin-glass and ferromagnetic orderings. *Phys. Rev. Lett.*, 47:201–204, 1981.

[10] I. Ya. Korenblit and E. F. Shender. Spin glass in an lsing two-sublattice magnet. *Sov. Phys. JETP*, 62:1030, 1985.

[11] I. Ya. Korenblit, Yu. A. Fedorov, and E. F. Shender. Antiferromagnetic spin glass in the lsing model. *Sov. Phys. JETP*, 65:400, 1987.

[12] I. Ya. Korenblit and E. F. Shender. Magnetic properties of frustrated antiferromagnets. phase transition into spin glass. *Sov. Phys. JETP*, 66:597, 1987.

[13] K. Binder and K. Schröder. Phase transitions of a nearest-neighbor ising-model spin glass. *Phys. Rev. B*, 14:2142–2152, 1976.

[14] W. Kinzel. Remanent magnetization in spin-glasses. *Phys. Rev. B*, 19:4595–4607, 1979.

[15] N. Kawashima and A. P. Young. Phase transition in the three-dimensional $\pm j$ ising spin glass. *Phys. Rev. B*, 53:R484–R487, 1996.

[16] M. Palassini and S. Caracciolo. Universal finite-size scaling functions in the 3d ising spin glass. *Phys. Rev. Lett.*, 82:5128–5131, 1999.

[17] H. G. Ballesteros, A. Cruz, L. A. Fernández, V. Martín-Mayor, J. Pech, J. J. Ruiz-Lorenzo, A. Tarancón, P. Téllez, C. L. Ullod, and C. Ungil. Critical behavior of the three-dimensional ising spin glass. *Phys. Rev. B*, 62:14237–14245, 2000.

[18] I. A. Campbell, K. Hukushima, and H. Takayama. Extended scaling scheme for critically divergent quantities in ferromagnets and spin glasses. *Phys. Rev. Lett.*, 97:117202, 2006.

[19] M. Hasenbusch, A. Pelissetto, and E. Vicari. Critical behavior of three-dimensional ising spin glass models. *Phys. Rev. B*, 78:214205, 2008.

[20] K. Gunnarsson, P. Svedlindh, P. Nordblad, L. Lundgren, H. Aruga, and A. Ito. Static scaling in a short-range ising spin glass. *Phys. Rev. B*, 43:8199–8203, 1991.

[21] J. A. Olive, A. P. Young, and D. Sherrington. Computer simulation of the three-dimensional short-range Heisenberg spin glass. *Phys. Rev. B*, 34:6341–6346, 1986.

[22] W. L. McMillan. Domain-wall renormalization-group study of the random Heisenberg model. *Phys. Rev. B*, 31:342–343, 1985.

[23] B. W. Morris, S. G. Colborne, M. A. Moore, A. J. Bray, and J. Canisius. Zero-temperature critical behaviour of vector spin glasses. *Journal of Physics C: Solid State Physics*, 19(8):1157, 1986.

[24] H. Kawamura. Chiral ordering in Heisenberg spin glasses in two and three dimensions. *Phys. Rev. Lett.*, 68:3785–3788, 1992.

[25] F. Matsubara, T. Shirakura, and S. Endoh. Spin and chirality autocorrelation functions of a Heisenberg spin-glass model. *Phys. Rev. B*, 64:092412, 2001.

[26] T. Nakamura and S-I. Endoh. A spin-glass and chiral-glass transition in a ±j Heisenberg spin-glass model in three dimensions. *Journal of the Physical Society of Japan*, 71:2113–2116, 2002.

[27] L. W. Lee and A. P. Young. Single spin and chiral glass transition in vector spin glasses in three dimensions. *Phys. Rev. Lett.*, 90:227203, 2003.

[28] D. X. Viet and H. Kawamura. Numerical evidence of spin-chirality decoupling in the three-dimensional Heisenberg spin glass model. *Phys. Rev. Lett.*, 102:027202, 2009.

[29] L. A. Fernandez, V. Martin-Mayor, S. Perez-Gaviro, A. Tarancon, and A. P. Young. Phase transition in the three dimensional Heisenberg spin glass: Finite-size scaling analysis. *Phys. Rev. B*, 80:024422, 2009.

[30] D. X. Viet and H. Kawamura. Spin-chirality decoupling in the one-dimensional Heisenberg spin glass with long-range power-law interactions. *Phys. Rev. Lett.*, 105:097206, 2010.

[31] L. P. Lévy and Andrew T. Ogielski. Nonlinear dynamic susceptibilities at the spin-glass transition of ag:mn. *Phys. Rev. Lett.*, 57:3288–3291, 1986.

[32] H. Bouchiat. Determination of the critical exponents in the AgMn spin glass. *J. Phys. France*, 47(1):71–88, 1986.

[33] E. Vincent and J. Hammann. Critical behaviour of the $CdCr_{2\times0.85}In_{2\times0.15}S_4$ insulating spin glass. *Journal of Physics C: Solid State Physics*, 20(18):2659, 1987.

[34] J. R. Thomson, H. Guo, D. H. Ryan, M. J. Zuckermann, and M. Grant. Magnetic ordering in the three-dimensional frustrated Heisenberg model. *Phys. Rev. B*, 45:3129–3132, 1992.

[35] Morten Nielsen, D. H. Ryan, Hong Guo, and Martin Zuckermann. Magnetic ordering in the three-dimensional site-disordered Heisenberg model. *Phys. Rev. B*, 53:343–349, 1996.

[36] J. Lauer and W. Keune. Magnetic double transition in Au-Fe near the percolation threshold. *Phys. Rev. Lett.*, 48:1850–1853, 1982.

[37] I. A. Campbell, D. Arvanitis, and A. Fert. Critical line for strong irreversibility in spin-glass and ferro-spin-glass alloys. *Phys. Rev. Lett.*, 51:57–60, 1983.

[38] D. H. Ryan, J. M. D. Coey, E. Batalla, Z. Altounian, and J. O. Ström-Olsen. Magnetic properties of iron-rich Fe-Zr glasses. *Phys. Rev. B*, 35:8630–8638, 1987.

[39] H. Yoshizawa, S. Mitsuda, H. Aruga, and A. Ito. Mixed phase of spin-glass ordering and antiferromagnetism in an ising system, $Fe_xMn_{1-x}TiO_3$. *Phys. Rev. Lett.*, 59:2364–2367, 1987.

[40] A. Ito, S. Morimoto, and H. Aruga Katori. Mössbauer studies of the ising spin-glass system $Fe_{0.5}Mn_{0.5}TiO_3$ in connection with the de almeida-thouless line. *Journal of the Physical Society of Japan*, 65(10):3331–3335, 1996.

[41] P.-Z. Wong, S. von Molnar, T. T. M. Palstra, J. A. Mydosh, H. Yoshizawa, S. M. Shapiro, and A. Ito. Coexistence of spin-glass and antiferromagnetic orders in the ising system $Fe_{0.55}Mg_{0.45}Cl_2$. *Phys. Rev. Lett.*, 55:2043–2046, 1985.

[42] R. J. Borg and C. E. Violet. Metallurgical explanation of "double magnetic transitions" and allied phenomena in AuFe alloys. *Journal of Applied Physics*, 55:1700–1702, 1984.

[43] Paul A. Beck. Spin clusters and random local anisotropy in mictomagnetic Au-Fe alloys. *Phys. Rev. B*, 32:7255–7262, 1985.

[44] E. Dartyge, H. Bouchiat, and P. Monod. X-ray determination of atomic short-range order in the spin-glass system AuFe. *Phys. Rev. B*, 25:6995–7002, 1982.

[45] J. W. Cable, G. Parette, and Y. Tsunoda. Spin correlations in $Au_{0.85}Fe_{0.15}$. *Phys. Rev. B*, 36:8467–8470, 1987.

[46] S. N. Kaul, V. Siruguri, and G. Chandra. Magnetization and Mössbauer study of the reentrant amorphous $Fe_{90}Zr_{10}$ alloy. *Phys. Rev. B*, 45:12343–12356, 1992.

[47] F. Bensamka, D. Bertrand, A.R. Fert, G. Jehanno, and J.A. Nasser. Mössbauer spectroscopy of the spin glass compounds $Fe_xMg_{1-x}Cl_2$. *J. Phys. France*, 48(6):1041–1050, 1987.

[48] A. M. Alakrmi, R. E. Vandenberghe, and E. De Grave. Mössbauer study of the re-entrant spin-glass behaviour in the mixed spinel ferrites $Mg_{(0.9+x)}Fe_{2(1-x)}Ni_{0.1}Ti_xO_4$ (x=0.5 and 0.6). *Journal of Magnetism and Magnetic Materials*, 322(5):510 – 516, 2010.

[49] G. A. Smolenskii and I. E. Chupis. Ferroelectromagnets. *Sov. Phys. Usp.*, 25(7):475–493, 1982.

[50] G. A. Smolenskii. *Ferroelectrics and Related Materials*. Gordon and Breach, New York, 1984.

[51] V. A. Isupov. Ferroelectric and antiferroelectric perovskites $Pb(B'_xB''_{1-x})O_3$. *Ferroelectrics*, 289(1):131–195, 2003.

[52] HRPT. http://sinq.web.psi.ch/sinq/instr/hrpt/index.html.

[53] G. Shirane, S.M. Shapiro, and J.M. Tranquada. *Neutron Scattering with a Triple-Axis Spectrometer: Basic techniques*. Cambridge University press, 2002.

[54] TASP. http://www.psi.ch/sinq/tasp/.

[55] S. J. Blundell. Spin-polarized muons in condensed matter physics. *Contemporary Physics*, 40(3):175–192, 1999.

[56] Kubo-Tayabe functions. http://www.fis.unipr.it/~derenzi/dispense/pmwiki.php?n=MuSR.KuboFunctions.

[57] V. Bonny, M. Bonin, P. Sciau, K. J. Schenk, and G. Chapuis. Phase transitions in disordered lead iron niobate: X-ray and synchrotron radiation diffraction experiments. *Solid State Communications*, 102(5):347 – 352, 1997.

[58] N. Lampis, P. Sciau, and A. G. Lehmann. Rietveld refinements of the paraelectric and ferroelectric structures of Pb $(Fe_{0.5}Nb_{0.5})O_3$. *J. Phys.: Condens. Matter*, 11:3489–3500, 1999.

[59] S. A. Ivanov, R. Tellgren, and N.W. Thomas. Investigation of the structure of the relaxor ferroelectric $Pb(Fe_{1/2}Nb_{1/2})O_3$ by neutron powder diffraction. *J. Phys. : Condens. Matter*, 49:1283–1286, 2007.

[60] A. Falqui, N. Lampis, Geddo-Lehmann A., and Gabriella P. Low-temperature magnetic behavior of perovskite compounds $PbFe_{1/2}Ta_{1/2}O_3$ and $PbFe_{1/2}Nb_{1/2}O_3$. *J. Phys. Chem. B*, 109:22967–22970, 2005.

[61] G. M. Rotaru, B. Roessli, A. Amato, S. N. Gvasaliya, C. Mudry, S. G. Lushnikov, and T. A. Shaplygina. Spin-glass state and long-range magnetic order in $Pb(Fe_{1/2}Nb_{1/2})O_3$ seen via neutron scattering and muon spin rotation. *Phys. Rev. B*, 79:184430, 2009.

[62] W. Kleemann, V. V. Shvartsman, P. Borisov, and A. Kania. Coexistence of antiferromagnetic and spin cluster glass order in the magnetoelectric relaxor multiferroic $PbFe_{0.5}Nb_{0.5}O_3$. *Phys. Rev. Lett.*, 105:257202, 2010.

[63] Ashok Kumar, R. S. Katiyar, Carlos Rinaldi, Sergey G. Lushnikov, and Tatjana A. Shaplygina. Glasslike state in $Pb(Fe_{1/2}Nb_{1/2})O_3$single crystal. *Appl. Phys. Lett.*, 93(23):232902, 2008.

[64] I. Mirebeau, C. Bellouard, M. Hennion, G. Jehanno, V. Caignaert, A. J. Dianoux, T. E. Phillips, and K. Moorjani. Coexistence of antiferromagnetic order and spin glass freezing in$YBa_2(Cu_{0.88}Fe_{0.12})_3O_{6.5}$. *Physica C Superconductivity*, 184:299–310, 1991.

[65] I. P. Raevski, S. P. Kubrin, S. I. Raevskaya, D. A. Sarychev, S. A. Prosandeev, and M. A. Malitskaya. Magnetic properties of $Pb(Fe_{1/2}Nb_{1/2})O_3$: Mössbauer spectroscopy and first-principles calculations. *Phys. Rev. B*, 85:224412, 2012.

[66] G. Shirane, D.E. Cox, and S. L. Ruby. Mössbauer study of isomer shift, quadrupole interaction, and hyperfine field in several oxides containing Fe^{57}. *Phys. Rev.*, 125(4):1158, 1962.

[67] R. A. Brand, J. Lauer, and W. Keune. Magnetic double transition in Au-Fe: Observation of spin canting in zero magnetic field. *Phys. Rev. B*, 31:1630–1632, 1985.

[68] R. A. Brand, H. Georges-Gibert, J. Hubsch, and J. A. Heller. Ferrimagnetic to spin glass transition in the mixed spinel $Mg_{1+t}Fe_{2-2t}Ti_tO_4$: a mossbauer and dc susceptibility study. *Journal of Physics F: Metal Physics*, 15(9):1987, 1985.

[69] L. J. P. Ketelsen and M. B. Salamon. Transverse freezing in the amorphous spin-glass $Fe_{10}Ni_{70}P_{20}$. *Phys. Rev. B*, 30:2718–2723, 1984.

[70] D. H. Ryan, J. M. Cadogan, and J. van Lierop. Muon spin resonance study of transverse spin freezing in a-Fe_xZr_{100-x}. *Phys. Rev. B*, 61:6816–6820, 2000.

[71] N. Lampis, P. Sciau, and A.G. Lehmann. Rietveld refinements of the paraelectric and ferroelectric structures of $PbFe_{0.5}Ta_{0.5}O_3$. *Powder Diffraction*, 12:2367–2378, 2000.

[72] S. Chillal, M. Thede, F. J. Litterst, S. N. Gvasaliya, T. A. Shaplygina, S. G. Lushnikov, and A. Zheludev. Microscopic coexistence of antiferromagnetic and spin-glass states. *Phys. Rev. B*, 87:220403, 2013.

[73] L. I. Shvorneva and Yu. N. Venevtsev. Perovskites with ferroelectric-magnetic properties. *Soviet Phys. JETP*, 22(4):722–724, 1966.

[74] S. Nomura, H. Takabayashi, and T. Nakagawa. Dielectric and magnetic properties of $PbFe_{1/2}Ta_{1/2}O_3$. *Jpn. J. Appl. Phys.*, 7:600–604, 1968.

[75] R. Martinez, R. Palai, H. Huhtinen, J. Liu, J. Scott, and R. Katiyar. Nanoscale ordering and multiferroic behavior in $PbFe_{1/2}Ta_{1/2}O_3$. *Phys. Rev. B*, 82:1–10, 2010.

[76] S. A. Ivanov, S Eriksson, N. W. Thomas, R. Tellgren, and H. Rundölf. A neutron powder diffraction study of the ferroelectric relaxor $Pb(Fe_{1/2}Ta_{1/2})O_3$. *J. Phys.: Condens. Matter*, 13:25–33, 2001.

[77] N. Lampis, C. Franchini, G. Satta, A. Geddo-Lehmann, and S. Massidda. Electronic structure of $PbFe_{1/2}Ta_{1/2}O_3$: Crystallographic ordering and magnetic properties. *Phys. Rev. B*, 69:1–12, 2004.

[78] M. Janoschek, S. Klimko, R. Gähler, B. Roessli, and P. Böni. Spherical neutron polarimetry with MuPAD. *Physica B: Condensed Matter*, 397:125–130, 2007.

[79] A Zheludev. Reslib 4.2, 2007. http://www.neutron.ethz.ch/research/resources/reslib.

[80] D. H. Ryan, A. D. Beath, E. McCalla, J. van Lierop, and J. M. Cadogan. Transverse spin freezing in a-$(Fe_{1-x}Mn_x)_{78}Si_8B_{14}$: A site-frustrated metallic glass. *Phys. Rev. B*, 67:104404, 2003.

[81] H. Ren and D. H. Ryan. Exchange frustration and transverse spin freezing in iron-rich metallic glasses. *Phys. Rev. B*, 51:15885–15897, 1995.

[82] I. A. Campbell and S. Senoussi. Re-entrant systems: A compromise between spin glass and ferromagnetic order. *Philosophical Magazine B*, 65(6):1267–1274, 1992.

[83] S. A. Ivanov, S.-G. Eriksson, R. Tellgren, and H. Rundlöf. Neutron powder diffraction study of the magnetoelectric relaxor $Pb(Fe_{2/3}W_{1/3})O_3$. *Materials Research Bulletin*, 39:2317–2328, 2004.

[84] L. Feng, H. Guo, and Z-G. Ye. Magnetic ordering in relaxor ferroelectric (1-x)$Pb(Fe_{2/3}W_{1/3})O_3$-(x)$PbTiO_3$ single crystals. *Journal of Materials Research*, 22:2116–2124, 2007.

[85] Z-G. Ye, K. Toda, M. Sato, E. Kita, and H. Schmid. Synthesis, structure and properties of the magnetic relaxor ferroelectric Pb $(Fe_{2/3}W_{1/3})O_3$ [PFW]. *Journal of the Korean Physical Society*, 32:S1028–S1031, 1998.

[86] L. Mitoseriu, D. Marré, A. S. Siri, and P. Nanni. Magnetic properties of $Pb(Fe_{2/3}W_{1/3})O_3$-$PbTiO_3$ solid solutions. *Applied Physics Letters*, 83:5509–5511, 2003.

[87] A.S. Kamzin and V.A. Bokov. Mössbauer studies of $PbFe_{2/3}W_{1/3}O_3$ multiferroics. *Physics of the Solid State*, 55(6):1191–1197, 2013.

[88] A. Prasatkhetragarn, P. Ketsuwan, S. Ananta, R. Yimnirun, and D. P. Cann. Phase formation, microstructure, and dielectric properties of (1-x)PZT - (x)PCN ceramics. *Materials Letters*, 63:1281–1284, 2009.

[89] E.A. Popova, V.G. Zalessky, T.A. Shaplygina, S.N. Gvasaliya, S.G. Lushnikov, and S.V. Krivovichev. X-ray and dielectric investigations of $PbCo_{1/3}Nb_{2/3}O_3$ single crystals. *Ferroelectrics*, 412:15–22, 2011.

[90] Y.N. Venevtsev, G.S. Zhdanov, and V.V. Ivanova. New lead-containing perovskite compounds of complex composition. *Doklady Akademii Nauk SSSR*, 158:86, 1964.

[91] D. Stauffer. Scaling theory of percolation clusters. *Physics Reports*, 54(1):1 – 74, 1979.

[92] A. B. Denison, H. Graf, W. Kündig, and P. F. Meier. Positive muons as probes in ferromagnetic metals. *Helvetica Phys. Acta*, 52:460, 1980.

[93] S. F. J. Cox. Implanted muon studies in condensed matter science. *J. Phys. C: Solid State Phys.*, 20:3187, 1987.

[94] A. Yaouanc and P. Dalmas de Reotier. *Muon Spin Rotation, Relaxation, and Resonance: Applications to Condensed Matter*. Oxford University Press, USA, 2011.

[95] Y. J. Uemura, T. Yamazaki, R. S. Hayano, R. Nakai, and C. Y. Huang. Zero-field spin relaxation of μ^+ as a probe of the spin dynamics of AuFe and CuMn spin-glasses. *Phys. Rev. Lett.*, 45:583–587, 1980.

[96] I. A. Campbell, A. Amato, F. N. Gygax, D. Herlach, A. Schenck, R. Cywinski, and S. H. Kilcoyne. Dynamics in canonical spin glasses observed by muon spin depolarization. *Phys. Rev. Lett.*, 72:1291–1294, 1994.

[97] Y.J. Uemura, K. Nishiyama, T. Yamazaki, and R. Nakai. Muon spin relaxation in a spin glass CuMn observed in finite longitudinal magnetic fields. *Solid State Communications*, 39(3):461 – 465, 1981.

[98] A. Keren, P. Mendels, I. A. Campbell, and J. Lord. Probing the spin-spin dynamical autocorrelation function in a spin glass above T_g via muon spin relaxation. *Phys. Rev. Lett.*, 77:1386–1389, 1996.

[99] S. Chillal, S. N. Gvasaliya, A. Zheludev, D. Schroeter, M. Kraken, F. J. Litterst, T. A. Shaplygina, and S. G. Lushnikov. Magnetic short- and long-range order in $PbFe_{0.5}Ta_{0.5}O_3$. *Phys. Rev. B*, 89:174418, 2014.

[100] C. Stock, S. R. Dunsiger, R. A. Mole, X. Li, and H. Luo. Coupled short-range ferroelectric and magnetic order in $PbFe_{1/2}Nb_{1/2}O_3$. *Physical Review B*, 88:094105, 2013.

[101] G. J. Coombs, R. A. Cowley, W. J. L. Buyers, E. C. Svensson, T. M. Holden, and D. A. Jones. Magnetic excitations in antiferromagnetic $Mn_{1-c}Zn_cF_2$ at large Zn concentrations. *Journal of Physics C: Solid State Physics*, 9(11):2167, 1976.

[102] R. A. Cowley, G. Shirane, R. J. Birgeneau, and H. J. Guggenheim. Spin fluctuations in random magnetic-nonmagnetic two-dimensional antiferromagnets. i. dynamics. *Phys. Rev. B*, 15:4292–4302, 1977.

[103] A. Apetrei, I. Mirebeau, I. Goncharenko, D. Andreica, and P. Bonville. Microscopic study of a pressure-induced ferromagnetic spin-glass transition in the geometrically frustrated pyrochlore $(Tb_{1-x}La_x)_2Mo_2O_7$. *Phys. Rev. Lett.*, 97:206401, 2006.

[104] D. P. Kozlenko, S. E. Kichanov, E. V. Lukin, N. T. Dang, L. S. Dubrovinsky, H.-P. Liermann, W. Morgenroth, A. A. Kamynin, S. A. Gridnev, and B. N. Savenko. Pressure-induced polar phases in relaxor multiferroic $PbFe_{0.5}Nb_{0.5}O_3$. *Phys. Rev. B*, 89:174107, 2014.

[105] M. J. Cooper and R. Nathans. The resolution function in neutron diffractometry. I. The resolution function of a neutron diffractometer and its application to phonon measurements. *Acta Crystallographica*, 23:357–367, 1967.

[106] M. Popovici. On the resolution of slow-neutron spectrometers. IV. The triple-axis spectrometer resolution function, spatial effects included. *Acta Crystallographica Section A*, 31(4):507–513, 1975.

[107] S. N. Gvasaliya, B. Roessli, D. Sheptyakov, S. G. Lushnikov, and T. A. Shaplygina. Neutron scattering study of $PbMg_{1/3}Ta_{2/3}O_3$ and $BaMg_{1/3}Ta_{2/3}O_3$ complex perovskites. *The European Physical Journal B - Condensed Matter and Complex Systems*, 40(3):235–241, 2004.

Acknowledgements

First and foremost I am grateful to Prof. Dr. Andrey Zheludev for giving me the opportunity to work towards my PhD in the group of Neutron Scattering and Magnetism at the Laboratory for Solid State Physics, ETH Zurich. His constant encouragement and constructive criticism throughout my work duration has greatly helped me in shaping my scientific thoughts. My PhD work would not have been as smooth and educational without the mentorship of Dr. Severian Gvasaliya. I am extremely thankful to him for visioning this project and providing a friendly, learning and exciting environment to carry out my thesis work. I am also thankful to Dr. Peter Gehring from NIST for agreeing to be my co-examiner and coming all the way from USA to participate in the exam. I greatly appreciate his support in evaluating this thesis.

The thesis work would not have been possible without the constant efforts of Prof. Dr. Sergey Lushnikov, Ioffe State University, Russia in providing me the excellent samples. I am extremely thankful to him and his team for their support. The help of Prof. Dr. Jochen Fred Litterst, Technische Universität Braunschweig, Germany was instrumental in obtaining important results through Mössbauer spectroscopy. I am very thankful to him and his team for the fruitful collaboration.

I would like to thank Dr. Denis Cheptiakov at LNS and Dr. Rustem Khasanov, Dr. Alex Amato and Dr. Chris Bains at LMU in PSI for useful discussion and support during and after the measurements at the SINQ and SMuS facilities. I would also like to thank Dr. Oleg Sobolev from FRM II, Munich for his support during measurements at PUMA.

It gives me a great pleasure to thank Ms. Brigitte Abt for her help in all the aspects of administrative work and her support throughout my PhD duration. I would like to thank the current and former group members of NSM, Dan, Sebastian, Wolfram, Erik, Matthias, Dave, Manuel, Gediminas, Nicole, Johannes, Kiril, Gerard, Alex for all the scientific and funny discussions at the memorable bistro coffee sessions. Special thanks to Mathias for proof reading some of the thesis chapters and helping with the German translation of the abstract. Thanks to Gwen and Shuang for the enjoyable time on and off the work at PSI.

I would like to thank my parents Renuka and Vittal Rao Chillal for their constant support and encouragement throughout my life despite the many hard times. I would like to extend the gratitude to my in-laws for continuing the support that my parents have bestowed upon me. Finally, I would like to thank Veeresh Deshpande (who happens to be my spouse) for his immense support throughout my PhD. I am also very thankful to him for proof reading this thesis.

Curriculum Vitæ

Personal Details

Name:	Shravani CHILLAL
DOB:	27-08-1986
Birth Place:	Narayanpet, India

Education

1991–2001	Secondary School Dayanand Vidya Mandir High School, Narayanpet, India
2001–2003	Intermediate Education Sri Sai Co-operative Junior College, Narayanpet, India
2003–2007	B.Sc. in Mathematics, Physics, Electronics & Computer Sciences Osmania University College for Women, Hyderabad, India
2007–2009	M.Sc. in Physics Indian Institute of Technology Madras, India
2009–2010	Masters in Material Science exploring European Large scale Facilities (Erasmus Mundus) M.Sc. in Engineering Physics Technische Universität München, Germany M.Sc. in Materials and Business Université Rennes 1, France
2011–2015	Ph.D. thesis *Microscopically Coexisting Antiferromagnetic and Spin glass States in Disordered Perovskites* Eidgenössische Technische Hochschule Zürich, Switzerland Advisor: Prof. Dr. Andrey Zheludev

Scholarships

2009–2010	Erasmus Mundus scholarship for Masters in Material Science exploring European Large scale Facilities
2007–2009	Institute Merit scholarship for M.Sc in Indian Institute of Technology Madras
2008	Young Scientist Research scholarship for summer internship in Raja Ramanna Centre for Advanced Technology

Publications

- S. Chillal, M. Thede, F. J. Litterst, S. N. Gvasaliya,T. A. Shaplygina, S. G. Lushnikov, A. Zheludev, *Microscopic Coexistence of Antiferromagnetic and spin glass states*, Phys. Rev. B **87**, 220403(R), 2013.
- S. Chillal, S. N. Gvasaliya, A. Zheludev, M. Kraken, D. Schoeter, F. J. Litterst, T. A. Shaplygina, S. G. Lushnikov, *Magnetic short- and long-range order in* $PbFe_{0.5}Ta_{0.5}O_3$, Phys. Rev. B **89**, 174418, 2014.
- S. Chillal, D. Koulialias, S. N. Gvasaliya, R. A. Cowley, L. I. Ivleva, S. G. Lushnikov, A. Zheludev, , *Phase transition of chemically doped uniaxial relaxor ferroelectric*, arXiv:1505.03499, Phys. Rev. B (submitted), 2015.